NOTE TO USERS

This reproduction is the best copy available.

UMI®

HIGH-SPEED DIGITAL MODE CONTROL FEEDBACK ON MAGNETO-HYDRODYNAMIC INSTABILITIES IN THE HBT-EP TOKAMAK

by

Alexander Jörgen Klein

Professor Thomas Sunn Pedersen

Submitted in partial fulfillment of the requirements for the degree

of Doctor of Philosophy

IN THE GRADUATE SCHOOL OF ARTS AND SCIENCES

COLUMBIA UNIVERSITY

2005

UMI Number: 3209347

INFORMATION TO USERS

The quality of this reproduction is dependent upon the quality of the copy submitted. Broken or indistinct print, colored or poor quality illustrations and photographs, print bleed-through, substandard margins, and improper alignment can adversely affect reproduction.

In the unlikely event that the author did not send a complete manuscript and there are missing pages, these will be noted. Also, if unauthorized copyright material had to be removed, a note will indicate the deletion.

UMI®

UMI Microform 3209347

Copyright 2006 by ProQuest Information and Learning Company.

All rights reserved. This microform edition is protected against unauthorized copying under Title 17, United States Code.

ProQuest Information and Learning Company
300 North Zeeb Road
P.O. Box 1346
Ann Arbor, MI 48106-1346

ABSTRACT

High-speed Digital Mode Control Feedback on Magneto-hydrodynamic Instabilities in the HBT-EP Tokamak

Alexander Jörgen Klein

Ideal magneto-hydromagnetic (MHD) instabilities set the limit on sustainable pressures in advanced tokamak devices, which are the leading candidates for viable fusion reactor concepts. Active feedback control of these instabilities may present a route to high-pressure operation with burning plasmas and is therefore of intense interest. The feedback system on the HBT-EP tokamak uses magnetic pick up and control coils which are arranged in what is called a "mode control" configuration and are coupled via a set of high-speed digital processors. Experiments are presented which show that this system is capable of suppressing these instabilities even when they are near the ideal limit. The effects of transfer function phase shifts, loop latency, and control coil coverage of the feedback system are characterized and shown to be critically important.

TABLE OF CONTENTS

TABLE OF CONTENTS .... **I**

LIST OF FIGURES .... **III**

ACKNOWLEDGMENTS .... **VIII**

CHAPTER 1) INTRODUCTION **1**

1.0 BACKGROUND 1
1.1 TOKAMAKS 4
1.2 BETA AND BETA LIMITS IN TOKAMAKS 7
1.3 HBT-EP 10

CHAPTER 2) EXTERNAL KINK MODE PHYSICS **14**

2.0 MHD AND FLUID EQUATIONS, STABILITY 14
2.1 KINK MODE IN THE LARGE ASPECT RATIO TOKAMAK 23
2.2 RESISTIVE WALL MODE 25

CHAPTER 3) FEEDBACK CONTROL OF EXTERNAL KINKS **28**

3.0 FEEDBACK CONTROL OF RESISTIVE WALL MODES 28
3.1 OPTIMIZED MODE CONTROL 29
3.2 MODELING OF PLASMA RESPONSE TO FEEDBACK 32
3.3 OPTIMIZED FEEDBACK HARDWARE ON HBT-EP 39

CHAPTER 4) SYSTEM CHARACTERISTICS **42**

4.0 MODE CONTROL SIGNAL PROCESSING 42
4.1 HARDWARE SPECIFIC TRANSFER FUNCTIONS 44
4.2 PHASE LEAD/LAG COMPENSATION 49
4.3 GAIN 54
4.4 LATENCY 64

CHAPTER 5) EQUILIBRIUM AND KINK OBSERVATION **66**

5.0 BASIC EQUILIBRIUM AND FEEDBACK EFFECTS 66
5.1 STABILITY OF EQUILIBRIUM 69
5.2 KINK MODE IDENTIFICATION 75
5.3 POLOIDAL SENSOR ARRAY PHASE ANALYSIS 76

CHAPTER 6) OPEN LOOP EXPERIMENTS **84**

6.0 MODE DIRECTION 84

6.1 MODE LOCKING 86

6.2 RESONANT ERROR FIELD AMPLIFICATION 89

CHAPTER 7) LATENCY EXPERIMENTS 91

7.0 THEORETICAL CONSIDERATIONS 91

7.1 EXPERIMENTAL RESULTS 93

CHAPTER 8) TOROIDAL PHASE ANGLE SCANS 96

8.0 TRANSFER FUNCTION VARIATION 96

8.1 PHASE STABILITY AND TRACKING 100

8.2 ROGOWSKI COIL ANALYSIS 103

8.3 POLOIDAL SENSOR ANALYSIS 112

8.4 SHELL MOUNTED PROBE (SMP) ANALYSIS 114

CHAPTER 9) GAIN SCANS AND GENERAL GAIN LIMITATIONS 122

CHAPTER 10) PARTIAL COVERAGE SCANS 125

10.0 MODE RIGIDITY 125

10.1 PARTIAL COVERAGE PHASE ANGLE SCAN RESULTS 127

10.2 SIDE BAND EXCITATION 133

CHAPTER 11) FUTURE WORK AND CONCLUSION 144

11.0 FUTURE CONTROL COIL MODIFICATIONS 144

11.1 ADVANCED ALGORITHMS AND NOISE REDUCTION 150

11.2 CONCLUSION 152

BIBLIOGRAPHY 154

LIST OF FIGURES

Figure 1.1-1: Tokamak magnetic field line topology 5
Figure 1.1-2: Major coil systems in a typical tokamak configuration 6
Figure 1.3-1: Experimental cell of HBT-EP 12
Figure 1.3-2: HBT-EP cross-section showing moveable shells, plasma and chamber walls ... 13
Figure 2.0-1: Cut through plasma torus revealing nested magnetic surfaces 17
Figure 2.0-2: Exaggerated distortion of a toroidal m/n = 3/1 external kink mode 22
Figure 2.1-1:Kink mode growth vs. edge q in large aspect ratio, low ß approximation 25
Figure 3.1-1: Schematic representation of smart shell vs. mode control configuration 32
Figure 3.3-1: Mode control feedback system as implemented on HBT-EP 40
Figure 4.1-1: Simplified schematic of input stage circuitry before digitization 46
Figure 4.1-2: combined RC filter network on analog board: amplitude transfer function 47
Figure 4.1-3: combined RC filter network on analog board: phase transfer function 47
Figure 4.1-4: Amplitude transfer (flux-flux) for feedback system without digital filtering 48
Figure 4.1-5: Transfer function phase shift for feedback system without digital filtering 48
Figure 4.2-1: Cost functions used to optimize digital phase lag/lead compensation filter 52
Figure 4.2-2: Amplitude transfer function for phase lag/lead compensators designed with cost functions 53
Figure 4.2-3: phase transfer function for phase lag/lead compensators designed with cost functions 53
Figure 4.3-1: Magneto-static analysis of single coil pair showing field strength (contours of 2, 4, 6, 8, 10 Gauss shown) and magnetic field lines for 10 A of current in the coils 55
Figure 4.3-2: Contour plot of *m/n* = 3/1 mode flux produced by perturbed plasma currents59
Figure 4.3-3: 3D depiction of model for control coil flux produced on plasma surface 60
Figure 4.3-4: Contour plot of flux produced by control coils vs. poloidal and toroidal angles60
Figure 4.3-5: Control coil currents for vacuum shot with normalized gain G = 1 (as used in subsequent experiments) 63
Figure 4.3-6: Control coil currents for vacuum shot with normalized gain G = 10 63
Figure 4.3-7: Control coil currents for vacuum shot with normalized gain G = 40 64
Figure 4.4-1: oscilloscope traces of input and output for NI 7831R FPGA modules 65

Figure 5.0-1: Basic plasma parameters: shot #43481 (black, no feedback), #43482 (red, positive feedback), #43494 (blue, negative feedback) 68

Figure 5.0-2: TokaMac output for shot #43268 (pressure profile and flux surfaces) 69

Figure 5.1-1: Radial magnetic field of *m*/*n* = 3/1 unstable mode in shot #43268 as computed by DCON 71

Figure 5.1-2: Cosine-like and Sine-like mode structure for 3-1 mode in shot#43268 as computed by DCON 73

Figure 5.1-3 *m*/*n* = 3/1 mode amplitude vs. poloidal angle for shot #43268 as computed by DCON 73

Figure 5.1-4: VALEN predictions for growth rates of external 3/1 kink modes for several s parameters as function of mode rotation 74

Figure 5.2-1: m = 3, m= 2 fluctuations in Rogowski coils and from modal decomposition in the SMPs 76

Figure 5.3-1: Integrated signals from top poloidal sensor group, shot #43075 77

Figure 5.3-2: Exaggerated lobe structures with modified poloidal anlges for several λ values78

Figure 5.3-3: Phase differences between n = 1 phases in the four poloidal groups for shot #43482 81

Figure 5.3-4: Expected n = 1 phase differences between the four poloidal groups based on known plasma and sensor positions 82

Figure 5.3-5: Expected phase difference spectrum for shot #43482, with λ =0.15 83

Figure 6.0-1: Four possible helical rotation directions in tokamaks. Mode rotation is in direction (A) 84

Figure 6.0-2: Open loop mode components (n = 0, 1, 2 = red, green, blue) in control coils and sensor coils (top poloidal array) 85

Figure 6.1-1: Phase locking between n = 1 components of control coil currents (5 kHz) and sensor coil voltages for shot #43075, waveform anti-parallel to magnetic field direction ("A" in Figure 6.0-1) 87

Figure 6.1-2: Phase relationship between n = 1 components in control coil currents (5 kHz) and sensor coil voltages for shot #43080, waveform parallel to magnetic field direction ("D" in Figure 6.0-1) 87

Figure 6.1-3: Phase relationship between n = 1 components in control coil currents (4 kHz) and sensor coil voltages for shot #43091, waveform in direction "B" in Figure 6.0-1 88

Figure 6.1-4: Phase relationship between n = 1 components in control coil currents (5 kHz) and sensor coil voltages for shot #43037, waveform in direction "C" in Figure 6.0-1 88

Figure 6.2-1: m = 3 Rogowski coil signals in vacuum (black), with plasma (red, shot #43075)89

Figure 7.0-1: Calculated phase response of feedback with latency of 10, 60, 110, 160, and 200 μsec 92

Figure 7.1-1: a) m = 3 Rogowski signal from shot #43312 (no feedback) and b) m=3 from shot #43305, negative feedback, but with 60 _sec latency 94

Figure 7.1-2: Smoothed histograms of m = 3 Rogowski signal amplitudes for various latency settings 95

Figure 8.0-1: Total system transfer functions for the toroidal phase angle scan experiments 98

Figure 8.0-2: Target phase angles for feedback experiments using digital filters [A] and [B]..99

Figure 8.0-3: Transfer function toroidal phase mapping for system with filter [A] and [B]. 100

Figure 8.1-1: Spatial phase relationship between n = 1 components for the 4 control/sensor groups 101

Figure 8.1-2: measured phase between n = 1 modes in control and sensor coil arrays (averaged over the four poloidal groups), for 2 < t < 3 msec vs. target phase set by rotation operator 102

Figure 8.1-3: Measured (average) phases between n = 1 components of control and sensor signals, color coded to indicate target phase 103

Figure 8.2-1: Raw m = 3 Rogowski coil signal amplitudes in interval 2 < t < 3 msec. A) with filter [A], B) with filter [B] 105

Figure 8.2-2: Integrated m = 3 Rog. coil signal amplitudes in interval 2 < t < 3 msec. A) with filter [A], B) with filter [B] 105

Figure 8.2-3: Natural (no feedback) mode, all angles (phase not defined without feedback) 107

Figure 8.2-4: Amplitude of m = 3 Rog. signals (raw) for data obtained with digital filter [A] and [B] 108

Figure 8.2-5: Amplitude of m = 3 Rogowski data with inverse toroidal phase mapping applied to compensate for transfer function phase shifts 109

Figure 8.2-6: Amplitude contour spectrum plots of magnetic m = 3 fluctuations detected by Rogowski coils (integrated signals for data set obtained with digital filter [A] and [B] 109

Figure 8.2-7: Control coil currents in coils at toroidal position T3 (near Rogowski coil) with and without plasma 110

Figure 8.2-8: m = 3 Rog. coil signals for plasma (positive feedback) and vacuum shot with similar control coil currents 111

Figure 8.2-9: : m = 3 Rog. coil signals for plasma (negative feedback) and vacuum shot with similar control coil currents 111

Figure 8.3-1: Geometry of poloidal groups and average n = 1 fluctuation signal levels (71 shots) in each group 113

Figure 8.3-2: n = 1 component of magnetic fluctuations recorded by poloidal sensor arrays vs. target control field phase shift, data from poloidal groups separated by color 113

Figure 8.4-1: Schematic of poloidal shell mounted Mirnov array (SMP) 115

Figure 8.4-2: Contour plot of magnetic fluctuations in SMP for shot # 47169 116

Figure 8.4-3: Spatial mode structure from SVD analysis in shot #44257 (each SMP signal normalized) 117

Figure 8.4-4: Unstable mode structure for m/n = 3/1 mode for shot #44257 as predicted by DCON 118

Figure 8.4-5: Time evolution of paired most dominant SVD modes (shot# 44257) 118

Figure 8.4-6: RMS of four most dominant mode pairs as identified by the SVD analysis from SMP signals during 2.4 < t < 2.7 msec (diamonds: m = 3 amplitude) 119

Figure 8.4-7: m = 3 and m = 2 mode evolution from SMP decomposition for three shots with and without feedback 120

Figure 8.4-8: Several shots with control phase adjusted for maximum excitation (red) and supression (blue) 120

Figure 10.1-1: Experimental arrangement for partial coverage phase angle scans: two Rogowski coils are at positions T1 and T3 near the control coils 129

Figure 10.1-2: Amplitude of Rogowski coil signals vs. Feedback phase angle setting for each of the two Rogowski coils for 36 different shots, full coverage 130

Figure 10.1-3: Amplitude of signals vs. feedback phase angle with coils near T1 muted 130

Figure 10.1-4: Amplitude of signals vs. feedback phase angle with coils near T3 muted 131

Figure 10.1-5: Amplitude of Rog. signals for maximum negative (blue) and positive (red) feedback applied with a) all coils active, b) c-coils near T3 muted, c) c-coils near T1 muted132

Figure 10.2-1: Smart shell control coil model showing location of control coils and plasma surface 136

Figure 10.2-2: Flux contour plot of radial field on plasma surface produced by smart shell control coils 136

Figure 10.2-3: Mode spectrum from Fourier analysis for smart shell flux. 3/1 mode amplitude squared is 13.44% of the sum of all the modes squared 137

Figure 10.2-4: Mode control coil model showing control coils and plasma surface 138

Figure 10.2-5: Flux contour plot of radial field on plasma surface produced by mode control coils 138

Figure 10.2-6: Mode spectrum from Fourier analysis mode control shells (paired). 3/1 mode amplitude squared is 3.4% of the sum of all the modes squared 139

Figure 10.2-7: Mode control model with one toroidal coverage gap showing location of control coils and plasma surface 140

Figure 10.2-8: Flux contour plot of radial field on plasma surface produced by mode control coils with one toroidal position deactivated 140

Figure 10.2-9: Mode spectrum from Fourier analysis mode control shells with toroidal coverage gap 141

Figure 11.0-1: Proposed feedback system to be installed on HBT-EP 145

Figure 11.0-2: Model of future control coils (5° coverage) and plasma surface 145

Figure 11.0-3: Flux contour plot of control field on plasma surface (5° coverage) 146

Figure 11.0-4: Mode spectrum from Fourier analysis when future mode control coils (5° coverage) are energized to produce m/n = 3/1 mode. The 3/1 mode amplitude squared is 2.6% of the sum of all the modes squared 147

Figure 11.0-5: Model of control coils (10° coverage) and plasma surface 147

Figure 11.0-6: Flux contour plot of radial field on plasma surface produced by future mode control coils (10° coverage) 148

Figure 11.0-7: Mode spectrum from Fourier analysis when future mode control coils (10° coverage) are energized to produce m/n = 3/1 mode. The 3/1 mode amplitude squared is 5.92% of the sum of all the modes squared 148

Figure 11.0-8: Model of proposed control coils (15° coverage)and plasma surface 149

Figure 11.0-9: Flux contour plot of radial field on plasma surface produced by future mode control coils (15° coverage) 149

Figure 11.0-10 Mode spectrum from Fourier analysis when future mode control coils (15° coverage) are energized to produce m/n = 3/1 mode. The 3/1 mode amplitude squared is 9.4% of the sum of all the modes squared 150

Figure 11.1-1: National Instruments 7831R module, LabVIEW programming illustration. 152

ACKNOWLEDGMENTS

I wish to express sincere appreciation to Professor Thomas Sunn Pedersen for his tireless and diligent efforts to support his own as well as other students at Columbia University. Clearly, his priorities lie in his role as educator and mentor. Professor Pedersen is always willing to talk to and make time for a student, always willing to consider a problem fully, never flippantly dismissing another's point of view, all the while working relentlessly on his own work and taking care of a family. Such dedication and productivity is awe-inspiring, and I can only hope to conduct my future affairs in a manner that remotely approximates this man's style. I am especially grateful for his willingness on several occasions to stand up intellectually on my behalf when I was surrounded by intimidating senior scientists. I could not have been more fortunate to have been able to enlist Professor Pedersen to act as my advisor.

Thanks also to David Maurer who can keep his head up and his gaze focused in a set of circumstances that is often bleak; his positive outlook was inspiring on several occasions. Additional thanks are in order to Dmitry Maslovsky for tolerating annoying questions and nagging requests about the DCON, VALEN, and TokaMac computer codes. Thanks to Nickolas Rivera, Jim Andrello, and John Moran for their technical support and ability to make things work.

Finally: thank you Anna, for supporting my life as a student and boy for the past three years, when I should have been a professional man by now. Thanks for dealing with being poor,

with fraternities and their urinations, and with the neglect that I often showed as a result of my studies. I owe you.

CHAPTER 1) INTRODUCTION

1.0 Background

The present level of population on earth, as well as the relative prosperity of a fraction of this population, is made possible only by energy intensive industrial and agricultural production and transportation. The energy requirements for our civilization have been increasing steadily over the past century. Today as in the past, these requirements are largely being met by the power produced in the burning of oil, natural gas, and coal, collectively known as the fossil fuels. These fuels constitute a finite resource; the rate of discovery of oil deposits for example peaked forty years ago, and at the time of this writing, crude oil is reaching its peak of production[1]. It is anticipated that in a few decades the cost of recovering crude oil will be prohibitively high. However, the true cost of the fossil fueled economy must not only be measured in simple monetary terms, but must also be understood in terms of indirect costs that are incurred. These include the geo-political ramifications: Energy consumption in the industrialized countries has long ago exceeded internal production capacity, and fuel imports constitute ever growing percentages of the trade balance. Most of the remaining large stores of oil are located in the Middle East, where political tension and instability are often a result of our foreign policies, which serve only to secure the flow of oil. At present, the toll of our military presence in oil rich regions consumes billions of dollars per day, not to mention thousands of human lives, which are the inevitable casualties in conflicts. As each industrialized nation scrambles to secure the remaining stores of fossils for themselves, the competition will undoubtedly lead to more conflict and war. In addition, fossil fuels come with environmental costs, which are also difficult to measure purely in terms of dollars. Just to mention the direct environmental effects on humans: Carcinogens, mercury, sulfur dioxide, and many other harmful compounds are released into the air in amounts that have very serious effects on disease and death rates. These claim millions of lives. As a small but striking example, a recent report by the Clean Air Task Force[2] estimates that the number of deaths caused by chronic exposure to diesel soot and fumes in New York City alone is on the order of 2,729 annually, accompanied by 4,342 heart attacks and many more asthma attacks requiring emergency room visits. Last but not least there is the prospect of fossil fuel induced climate change: global carbon dioxide emissions from fossil emissions into the atmosphere amount to 25 billion metric tons annually[3] which is having a disastrous effect on the planets climate equilibrium. It is beyond the scope of this dissertation to discuss global warming effects at any length, but the net result will be a likely decrease in the population carrying capacity of the planet.

Clearly, the need for non-carbon based energy sources is very great. It is this author's opinion that the only viable long term solution that will enable the continuation of an energy intensive industrialized society is the harnessing of the power produced in controlled nuclear fusion. The energy produced in fusion reactions is by far the greatest amount per atom when compared to fission or ordinary chemical (combustion) reactions. It is so enormous that the fusion of one ounce of deuterium (a common hydrogen isotope) is equivalent to burning

75,000 gallons of gasoline in terms of energy produced. Furthermore, since the fuels for fusion are the lightest elements in the periodic table, they are abundantly found throughout our world. Once we discover the method by which the fusion process can be initiated, sustained, and controlled in the laboratory (in an efficient and economically acceptable way), the fuels for this awesome energy source are virtually inexhaustible; deuterium for example is found in seawater in copious amounts. Fusion also produces no direct pollution or greenhouse gas emissions. Even for the reactions involving tritium, radiation levels are modest, and any radioactive waste produced has a very short half-life. For the so called "advanced fuels", all the fusion byproducts are charged particles whose kinetic energy can be directly converted into electricity, so that the reaction is accompanied by a complete absence of hazardous radiation and could be exploited with ~90% efficiency[4].

Fusion is not the stuff of science fiction: the sun and all the stars are examples of well designed fusion reactors. The military complex has had a fusion weapon for fifty years already. Among the science community there is broad consensus that it is a matter of when, not if, mankind will make fusion viable to produce net useable energy. It appears to be merely a matter of will and devoting the resources to the research. Historically, fusion has been the holy grail of plasma physics for over 50 years, but initial excitement in the field soon faded after it was determined that the task of developing this energy source would be more difficult than originally thought. Over the past 25 years, the U.S. national fusion sciences budget has been decreasing steadily[5] and now stands at a mere $270 Million per year. Although there has been great progress in plasma physics, it is generally believed that at the current rate the complete development of a useful fusion power source remains 40 years in the future. Whether or not the transition to fusion power can be accomplished in time to mitigate all of the effects of fossil depletion to a level that will allow modern civilization to carry on is doubtful, but certainly we must try.

1.1 Tokamaks

For fusion to yield useful energy, matter must be contained in the form of a plasma at about 100 million degrees centigrade, at pressures and for times long enough so that a substantial fraction of particles collide and undergo the fusion process. There are many schemes for creating the conditions for fusion in laboratory experiments. About forty years ago, the tokamak emerged as the leading candidate that might lead to commercial reactors, because at the time it demonstrated higher plasma temperatures than all the other known confinement schemes[6]. Since then, the emphasis in the fusion program has remained with the tokamak, and as a consequence it is the most developed device in the field. Many large and small tokamak experiments have been built and operated around the world. The newest and largest of these is the planned international thermonuclear experimental reactor (ITER), which, it is hoped, will contain a burning plasma producing net fusion power about 25 years from now. ITER is expected to cost $12 billion, the net energy gain is unlikely to be enough for a power plant, but it will demonstrate feasibility.

The tokamak is a Soviet invention (*TOroidalnya KAmera ee MAgnetnaya Katushka* – "torus-shaped magnetic chamber") by physicists Andrei Sakharov and Igor Tamm. It is a toroidal magnetic confinement device wherein a strong axial magnetic field is created using external electromagnets that are arranged around a donut-shaped vacuum chamber. This field is augmented by a poloidal field that arises from a large toroidal plasma current, which is usually induced by a large transformer using the plasma itself as the secondary winding. The resultant helical field lines form magnetic flux surfaces which hold the plasma, since plasma is comprised of charged particles which are constrained to follow the magnetic field lines around the torus. In this way the plasma is contained without contacting a material wall, which is a prerequisite for fusion: The temperature of solid material cannot exceed a few thousand degrees, but the fusion plasma must be at a temperature well over an order of magnitude hotter than the sun.

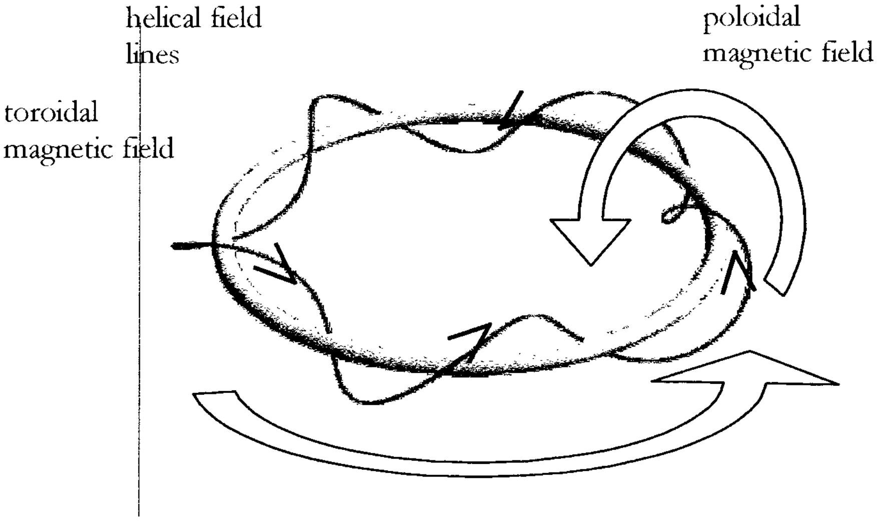

Figure 1.1-1: Tokamak magnetic field line topology

In addition to the main toroidal field coils, there are additional electromagnets which shape and stabilize the plasma position (vertical field coils), and large transformer coils which induce the plasma current. A typical tokamak configuration is shown in

Figure 1.1-2.

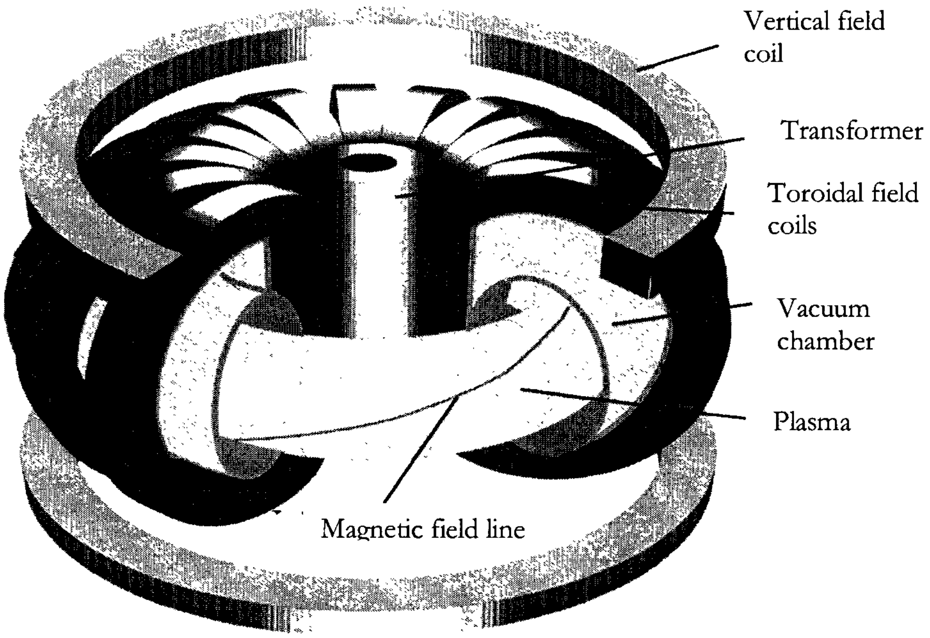
Vertical field coil
Transformer
Toroidal field coils
Vacuum chamber
Plasma
Magnetic field line

Figure 1.1-2: Major coil systems in a typical tokamak configuration

1.2 Beta and Beta Limits in Tokamaks

Although the tokamak has excellent confinement properties for low density plasmas, it has the disadvantage that the current in the plasma tends to make it unstable. Therefore tokamaks can operate only within limited parameters outside of which a sudden loss of confinement ("disruption") causes the plasma to lose its energy, or worse yet, crash against the inside of the vacuum vessel which results in a total loss of plasma and violent stresses on the physical structures of the containment vessel. This is not a problem from a physics standpoint, since disruptions can be avoided if the device is run conservatively, with low density and modest plasma current. In such a discharge, the so-called safety factor, q, is relatively high. However, for net fusion power, the product of density, temperature, and confinement time must reach a minimum value, known as the Lawson criterion. The scaling is such that the plasma confinement time increases with magnetic field and increases with device radius, so that in theory the tokamak could simply be designed to use very high magnetic fields in a very large containment vessel filled with a very modest plasma density to produce an excess of energy from fusion.

For reactor purposes, however, other considerations come into play. One important consideration involves economics: because the achievable toroidal field strength is limited by engineering constraints, the size of the containment vessel necessarily is on the order of meters to keep the particle confinement times reasonably high. Since the reactor is therefore relatively large, and because the magnetic field energy density is relatively high over a large volume, the cost associated with such a construction is such as to make energy production completely uneconomical unless the fusion rates are high enough to yield on the order of 500 Mega-Watts. It will now briefly be shown that for fusion to fulfill its promise of providing cheap and abundant energy, the plasma pressure must be able to grow to a sizeable fraction of the vacuum magnetic field pressure.

The ratio of plasma pressure to (vacuum) magnetic field pressure is defined as ß. For a thermal plasma with an isotropic Maxwellian velocity distribution, the pressure is simply the scalar product of density and temperature, *knT*, (k is the Boltzman constant and will be incorporated into units temperature for the remainder of this thesis) while the magnetic pressure is derived by evaluating the magnetic vacuum energy.

$$\beta \equiv nT \Big/ \frac{B^2}{2\beta_0} \qquad (1.2\text{-}1)$$

This quantity is limited by theoretical stability considerations, as well as empirical observations. It has been found that the maximum ß in tokamaks cannot much exceed the Troyon [7] limit which is defined in terms of a normalized ß involving the plasma current, I_p, and the plasma minor radius, a:

$$\beta_n \equiv \beta \Big/ \frac{I_p}{aB} \leq 3 \qquad (1.2\text{-}2)$$

The total fusion power output of a reactor may be expressed as a function of ß; because fusion is a process involving collisions between two particles, the fusion rate increases in proportion to the square of the density, and (at optimum temperature) as the square of the pressure:

$$\text{Fusion power} \propto \text{Volume} \cdot (nT)^2 \propto R^3\beta^2B^4 \tag{1.2-3}$$

Because the volume and the magnetic field of the reactor both cost money, and since in a "burning" plasma the input energy comes largely from the fusion burn, it is clearly imperative to maximize ß to achieve maximum reactor efficiency and economic feasibility. The ß limit can be improved somewhat by shaping the plasma cross-section, but in general tokamaks cannot run at ß's higher than about 5%.

Most scientists believe that a fusion reactor must operate in steady state, one of the reasons being that the stress on heat absorbing materials is too high for the thermal cycling from a pulsed machine. With purely inductive current drive and heating, tokamaks necessarily function in a pulsed mode. But they are capable of reaching steady state conditions by using additional current drive methods. Once the fusion burn is initiated, external heating can be reduced as the desired operating value for power amplification Q (≡ fusion power out / heating power to the plasma) is reached.≡ The additional heating systems can then be used to drive currents in the toroidal direction, either directly or indirectly (via a pressure gradient driven "bootstrap current"), sustaining the tokamak configuration. This kind of operation requires precise control over plasma temperature, current, and pressure profiles, and also calls for a host of other sophisticated means for interacting with the plasma. This is referred to as the "advanced tokamak" regime[8,9,10] Unfortunately, the current profiles required for advanced tokamak operation are such as to provide free energy to macro-instabilities that set the ceiling on the achievable β_n to unacceptably low values.

The upper limits to the realizable pressures in an advanced tokamak are set by magneto-hydrodynamic stability limits, notably the ideal external kink instability[11] which will be described in detail in chapter 2. This instability can be slowed by surrounding the plasma with conducting walls, so that the growth rate of the external kink is reduced to the rate at which a magnetic field will penetrate the conducting wall, in which case the ideal external kink is called the resistive wall mode (RWM). Without some means to eliminate this instability, economic operation on an advanced steady state power producing tokamak may not be possible.

1.3 HBT-EP

HBT-EP stands for High Beta Tokamak – Extended Pulse. It is a small tokamak designed specifically to study the ideal and resistive MHD beta limits in a tokamak, and to serve as a test bed to investigate means for the control of long wavelength MHD instabilities in order to extend these limits. The main parameters of the machine are listed in table 1.3.1. The experiment is much smaller than some of the major tokamaks such as D-III-D[12] or JET[13], but is able to achieve plasma states of relevance to these and even reactor-scale machines using only ohmic heating by incorporating several innovative features[14]. These include segmentation of the vacuum vessel into five sections, separated by quartz breaks. This allows magnetic flux to penetrate the chamber very rapidly. Additionally, the ohmic heating capacitor bank and air-core ohmic heating coil allow discharge programming to include a rapid and sustained current ramp with a rise time faster than the plasma magnetic diffusion rate. This in turn enables broad current profiles and prevents the high temperature core from sapping the ability of the ohmic heating system. The details of these features are found in [14]. The base vacuum pressure is as low as 3.5 x 10^{-9} Torr, a result of meticulous vacuum practices and baking procedures for the vessel. Consequently, impurity levels are kept as low as on the major machines, and the discharges can access the Troyon beta limits even though the typical temperature and magnetic field strength on HBT-EP are quite low by fusion standards.

parameter	**HBT-EP**	**DIII-D**
Major radius	R = 0.92 m	R = 1.67
Minor radius	a = 0.13 – 0.2 m	a = 0.62 m
Toroidal magnetic field	$B_T \leq 0.35$ Tesla	$B_T \leq 2.6$ Tesla
Plasma current	$I_p \leq 20$ kAmperes	$I_p \leq 3000$ kAmperes
Pulse length	$\tau_p \leq 10$ msec	$\tau_p \leq 10{,}000$ msec
Temperature	$<T_e> = 50 - 100$ eV	$<T_e> = 2000$ eV
Density	$<n_e> \sim 10^{19}\ \mathrm{m}^{-3}$	$<n_e> \sim 10^{19}\ \mathrm{m}^{-3}$

Table 1: Nominal parameters of the HBT-EP tokamak compared with those in a large Tokamak (DIII-D)

A unique feature of the HBT is the incorporation of moveable shells inside the vacuum vessel. There are ten toroidal positions where top and bottom shells on the outboard side are mounted on radially adjustable posts, for a total of twenty independently moveable shells that can be moved from radii b/a = 1.57 towards the plasma up to b/a = 1.07 (b ≡ shell radius, a ≡ plasma radius). Half of the shells are made of thick (1.4 cm) aluminum, so that these behave like perfectly conducting plates for time scales on the order of the discharge. The other half of the shells are made of thin stainless steel, upon which are mounted numerous sensor and control coils for active feedback experimentation. The proximity of conducting walls to the plasma has been shown to convert the fast growing ideal external kink mode to the slowly growing RWM, and in the presence of significant plasma rotation this can result even in complete stabilization of the mode.

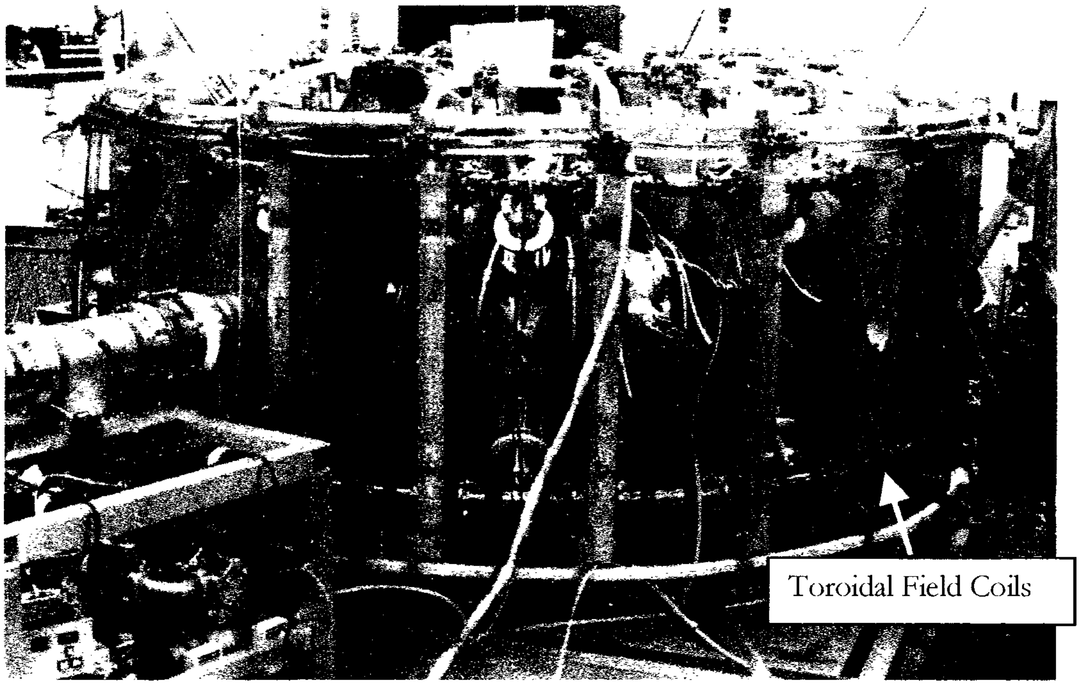

Figure 1.3-1: Experimental cell of HBT-EP

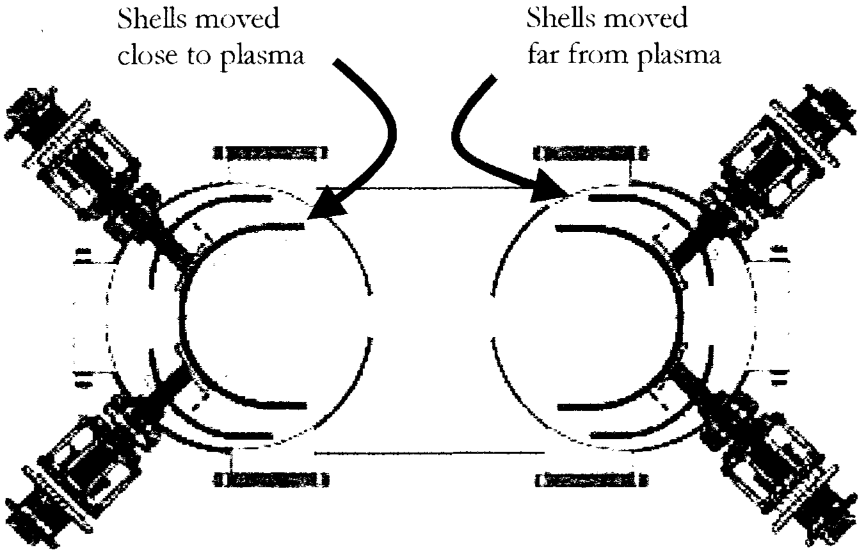
Shells moved
close to plasma
Shells moved
far from plasma

Figure 1.3-2: HBT-EP cross-section showing moveable shells, plasma and chamber walls

CHAPTER 2) EXTERNAL KINK MODE PHYSICS

2.0 MHD and Fluid Equations, Stability

Plasmas are ensembles of charged particles that interact with each other via long range Coulomb forces, and their behavior is generally extremely complicated and difficult to track analytically. However, when the particles are in thermal equilibrium, and have collision mean free paths much shorter than any length scales of interest (such as the macroscopic size of the plasma itself), they can be treated as an ideally conducting fluid. Tokamak plasmas are somewhat peculiar, as they typically operate at densities such that the mean free path for collisions along magnetic field lines between particles is very long (often thousands of meters), but because of the magnetic confinement the mean free path in the radial, cross-field direction is very small. Because particles travel in closed orbits, even the long mean free path in the parallel dimension does not thwart a general equilibrium from being quickly established. Therefore, the fluid description of plasmas works very well to describe the gross, first order behavior of plasmas in Tokamaks. In the absence of viscosity, the combined fluid equations for electrons and ions are listed here:

$$\frac{\partial \rho}{\partial t} = -\nabla \bullet (\rho\, \mathbf{u}) \quad \text{(mass conservation)} \tag{2.0-1}$$

$$\rho \frac{d\mathbf{u}}{dt} = \mathbf{j} \times \mathbf{B} - \nabla p \quad \text{(momentum conservation)} \tag{2.0-2}$$

$$\mathbf{E} + \mathbf{u} \times \mathbf{B} = 0 \quad \text{(simplified ideal Ohms Law)} \tag{2.0-3}$$

$$\frac{d}{dt}\left(\frac{p}{\rho^{5/3}}\right) = 0 \quad \text{(adiabatic energy conservation)} \tag{2.0-4}$$

The symbols in these expressions are defined as follows (bold indicates vector quantities):

ρ	Plasma density
$\mathbf{j}$	Current density
$\mathbf{B}$	Magnetic field
p	pressure
$\mathbf{u}$	Plasma velocity
μ_0	Permeability of free space

These relations, along with Maxwell's equations (in the low frequency limit) form the theory of ideal magneto-hydrodynamics (MHD). They imply that all particles are in isotropic thermodynamic equilibrium, that the plasma is quasi neutral, and that magnetic fields are "frozen" into the plasma, i.e. particles cannot move across magnetic field lines, nor are magnetic fields able to diffuse into the plasma*. The theory describes macroscopic plasma behavior fairly well for time scales longer than particle gyration about field lines and over distances much longer than the ion gyro radius for many types of plasmas. For detailed derivations of MHD theory, one can consult the textbooks listed in the references[15,16,17].

---

* The simplified static equilibrium ohm's law neglects what is known as the Hall term, which describes the physics of a two fluid (electrons and ions) model more adequately. One consequence of this is that magnetic fields are frozen into the electron fluid, not necessarily the plasma mass. This is why the kink modes in the experiments on HBT are seen to rotate with the electron bulk. For simplicity, this treatment is not followed in this chapter.

In (stationary) equilibrium, there is only one relevant fluid equation:

$$\mathbf{j} \times \mathbf{B} - \nabla p = 0 \tag{2.0-5}$$

along with the Maxwell's equations: $\nabla \times \mathbf{B} = \mu_0 \mathbf{j}$ and $\nabla \bullet \mathbf{B} = 0$. The equilibrium equation implies that plasmas are confined by magnetic fields such that the magnetic field lies along constant pressure surfaces. In a torus the magnetic field forms closed surfaces, and these can be of two general types: if one magnetic field line will come arbitrarily close to any point on its surface without ever closing in on itself, such a surface is called irrational. If, on the other hand, the magnetic field lines on a surface close in on themselves after some finite number of toroidal circuits, such a surface is termed rational. The distinction is important when considering stability of a particular state in the tokamak, as rational surfaces are prone to be susceptible to perturbations in magnetic topology.

The quantity known as the safety factor, q, describes properties of the magnetic surfaces and reveals whether or not a particular surface is rational. The safety factor is defined as the number of times a magnetic field line winds toroidally divided by the number of times it winds poloidally in the limit of following the field line infinitely far. One can interpret q as the average helical pitch of the magnetic field on a particular surface. If q is a rational number, then the surface is a rational surface. There are infinitely many nested surfaces in tokamaks, and most of these are of the irrational type, just as there are many more irrational numbers than rational ones on the number line.

Stability problems arise when q is a low order rational number. One intuitive way to see the reason for this is to understand that rational surfaces are not true surfaces at all: neighboring field lines are disconnected and independent of each other. Small perturbations can therefore easily tear the plasma apart.

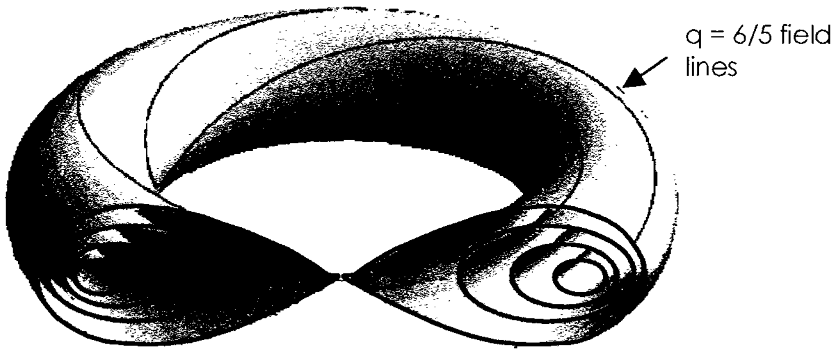

Figure 2.0-1: Cut through plasma torus revealing nested magnetic surfaces

Although a plasma may be in equilibrium, it is not at all ensured that such an equilibrium is stable, just as a pencil balanced on its point constitutes an unstable equilibrium. In general, current carrying plasmas in magnetic fields always have thermodynamic free energy which can drive instability, and the stability of a particular arrangement depends on the constraints on the motion of the plasma, which may or may not access the available free energy[18]. Tokamak plasmas in particular are subject to a great number of possible instabilities, which fall into two general categories: micro- and macro-instabilities. The former result when small scale phenomena cause turbulence and subsequent rapid diffusion of particles and energy. The more catastrophic, faster growing, and global type are the macro-instabilities. These can be understood by ideal or resistive MHD analysis, which has proven to be a very good indicator of how a particular plasma confinement scheme will behave in the laboratory. If MHD predicts instability, the confinement will almost certainly exhibit rapid and violent oscillations or even complete disruptions. Often, the unstable equilibrium is never observed in the first place.

The MHD stability of any particular equilibrium can be determined as follows: The equilibrium is allowed a small displacement, ζ, and the fluid momentum equation is linearized about small perturbations in all equilibrium quantities. The first order quantities are then balanced in an equation of motion. Using subscripts 0 and 1 to refer to equilibrium and perturbed quantities, the result is:

$$\rho\frac{\partial \mathbf{u}}{\partial t} = \mathbf{j}_1 \times \mathbf{B}_0 + \mathbf{j}_0 \times \mathbf{B}_1 - \nabla p_1 \tag{2.0-6}$$

The right hand side of equation 2.0-6 represents a force. The perturbed currents, magnetic field, as well as the pressure gradient can be re-expressed in terms of the plasma displacement and the equilibrium quantities by using the remaining (linearized) MHD and Maxwell equations. One then finds for the force:

$$\begin{aligned}\mathbf{F} = \nabla\left(\gamma p_0 \nabla \bullet \xi + \xi \bullet \nabla p_0\right) + \frac{1}{\mu_0}\left(\nabla \times \nabla \times \left(\xi \times \mathbf{B}_0\right)\right) \times \mathbf{B}_0 \\ + \frac{1}{\mu_0}\left(\nabla \times \mathbf{B}_0\right) \times \nabla \times \left(\xi \times \mathbf{B}_0\right)\end{aligned} \tag{2.0-7}$$

If this force is in the same direction as the displacement in some region, that region contributes to instability of the whole arrangement. The force field can be viewed as the gradient of a potential energy. Integrating the force along the infinitesimal displacements then is an evaluation of the potential energy of the system as it moves away from equilibrium. If the change in potential is negative, the equilibrium is unstable to the chosen perturbation. Mathematically, the condition for stability is expressed as what is known as the energy principle[19]:

$$\delta W = -\frac{1}{2} \int_{all\ space} \xi \bullet \mathbf{F}\, d^3x \geq 0 \tag{2.0-8}$$

This integral is evaluated over all space, and needs to be evaluated repeatedly for different displacement fields ξ, to look at all possible displacements. If a physically realizable displacement is found for which the energy change is negative, the equilibrium is proved to be unstable. The difficulty often lies in proving that a given equilibrium is a stable one.

The equation for δW is frequently manipulated into what is called its intuitive form, using much algebra, some vector identities, and the divergence theorem. In this form the energy integral is broken into separate components in separate regions (plasma and vacuum), each of which contributes terms which result from particular aspects of the physical perturbation. For example, there is energy associated with field line bending, as well as with field line compression or stretching. There is of course energy associated with compressing the plasma against it's own kinetic pressure.

The algebra required to write the energy equation in its extended, intuitive form is quite involved[20,21], so the results will simply be written below. The perturbed energy is written in terms of separate contributions from the plasma, the plasma surface (which vanishes unless there are surface currents), and the vacuum region(s), spelled out in equations 2.0-9,10, and 11.

$$\delta W = \frac{1}{2}\int_{plasma} \left(\begin{array}{l} +\dfrac{\left|\left(\nabla\times\left(\xi\times\mathbf{B_0}\right)\right)_\perp\right|^2}{\mu_0} \\ +\dfrac{\mathbf{B_0}^2}{\mu_0}\left|\nabla\bullet\xi_\perp+2\xi_\perp\bullet\dfrac{\mathbf{R_c}}{\mathbf{R_c}^2}\right|^2 \\ +\dfrac{5}{3}p\left|\nabla\bullet\xi\right|^2 \\ -2\left(\xi_\perp\bullet\nabla p\right)\left(\dfrac{\mathbf{R_c}}{\mathbf{R_c}^2}\bullet\xi^*_\perp\right) \\ -\mathbf{j_0}\left(\xi^*_\perp\times\mathbf{b}\right)\bullet\left(\nabla\times\left(\xi\times\mathbf{B_0}\right)\right)_\perp \\ \end{array} \right) d^3x \tag{2.0-9}$$

$$\delta \mathrm{W_s} = \frac{1}{2}\int_{\mathrm{surface}} \left|\mathrm{n}\bullet\xi_\perp\right|^2 \mathrm{n}\bullet\left[\!\left[\nabla\left(\mathrm{p}+\frac{\mathrm{B}^2}{2\mu_0}\right)\right]\!\right]_{\mathrm{jump}} \mathrm{d}^2\mathrm{x} \tag{2.0-10}$$

$$\delta \mathrm{W_v} = \frac{1}{2}\int_{\mathrm{vacuum}} \frac{\mathrm{B}^2}{2\mu_0}\ \mathrm{d}^3\mathrm{x} \tag{2.0-11}$$

In the preceding equations, the subscript indicating perpendicular and parallel components are with respect to the equilibrium magnetic field direction. R_c is the radius of curvature of the local magnetic field, b is the unit vector along the magnetic field, and n is the unit vector normal to the plasma surface.

Within the plasma, the plasma energy is separated into five terms. The first three terms represent magnetic field line bending, magnetic field compressions, and plasma compression, which always require energy, and therefore these terms are positive definite, always contributing to stability. The fourth term can be negative if the density gradient points in the same direction as the magnetic field curvature. This term causes ballooning instabilities when the pressure becomes high enough to overwhelm the stabilizing terms in toroidal geometry (toroidal geometries always have regions of bad field line curvature). The final term is proportional to the equilibrium current density and is always destabilizing. This is what is meant by the statement that there is always free energy available for instabilities when there are plasma currents. The currents give rise to the kink instability, consequently the term is often called the "kink term" in the energy equation. Finally, the surface term can be neglected in the absence of surface currents, while the vacuum contribution to the perturbed energy is always stabilizing.

The external kink instability is a special case of the general kink instability. In general, when a magnetic surface is of a rational type, it is susceptible to the smallest of perturbations which can destroy the surface and cause the formation of islands in the layers of the nested magnetic surfaces. If the rational surface is in the interior of the plasma, these islands can only form if the constraints of ideal MHD are relaxed to allow for magnetic flux diffusion in the plasma (by considering plasma resistivity). When current gradients drive an instability of this type, it is called a tearing mode, which evolves relatively slowly on the time scale of resistive diffusion. In the advanced tokamak configuration, these can be prevented or controlled by manipulating the plasma current profile or by injecting RF energy into regions where magnetic islands begin to form, among other methods.

More troublesome is when the rational surface lies near but outside of the edge of the plasma, because islands can form in the vacuum region very easily. One then labels the phenomenon the external kink instability (known also for a long time as a Mirnov[22] oscillation), it can grow very rapidly (limited only by plasma inertia), and there is little that can be done to avoid it completely once the edge of the plasma forms a rational surface. As there are always small imperfections in the magnetic field coils that form the tokamak configuration, there are always error fields with resonant components which act as small seed perturbations to excite the external kink (and which actually are amplified as the kink begins to go unstable).

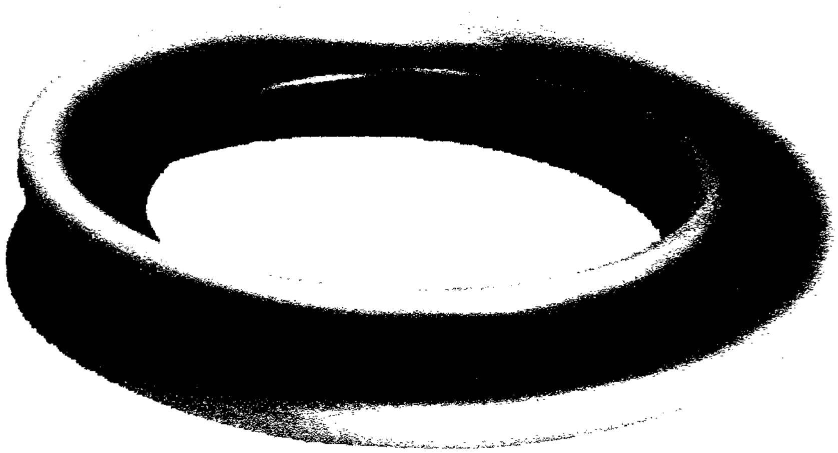

Figure 2.0-2: Exaggerated distortion of a toroidal m/n = 3/1 external kink mode

External kink modes can be somewhat stabilized by the presence of conducting walls, nevertheless they remain a ubiquitous problem for tokamaks. External kink modes have been predicted and observed in tokamaks for over forty years. It is somewhat interesting that these basic instabilities still represent most pressing obstacles to high ß operation and an active area of research.

2.1 Kink Mode in the Large Aspect Ratio Tokamak

Tokamak plasma stability can in truth only be evaluated numerically because of the complex plasma shapes that are usually involved, as well as pressure and current profiles that are in general not represented by simple analytic functions. Results of such analysis will be presented in section 5.1. However, it is useful (and adequate in some circumstances) to make approximations that allow for analytic treatment of the stability problem in order to understand the regimes in which tokamaks can operate, and to get reasonable estimates for the stability of a particular discharge. One common simplification of the problem is known as the large aspect ratio approximation, valid for near circular, long and skinny plasmas whose minor radius is much smaller than the major radius (the ratio of these is known as the inverse aspect ratio, ε, of a torus). Another (generally good) approximation is that of low ß. Since these parameters describe the HBT-EP, it is instructive to look at simple predictions and expand the δW equation in ε.

The large aspect ratio tokamak can be described using simple coordinates and estimates: Let the plasma cross-section be essentially round with circular magnetic surfaces, with plasma minor radius = a where a << R. Then the coordinates r (distance from major radius axis), θ (poloidal angle), and ϕ (toroidal angle) are well suited to describe the geometry. Because the plasma is assumed to be of very low ß, the plasma does not significantly distort the vacuum magnetic fields, the toroidal field is approximately constant in the plasma, and the r coordinate practically is a magnetic surface coordinate. The equilibrium equation can be written very simply, and the perturbed energy equation can be expanded in ε or even ε^2 . There have been many analytical treatments[23] of the large aspect ratio tokamak with different current profiles, good examples and derivations may be found in the texts by Freidberg and/or Wesson.[15,24] The plasma current profile provides the source of the kink energy, and the stability regimes that are discovered strongly depend on what current profiles are assumed. Perturbations are written in a Fourier expansions as

$$\xi_n(r,\theta,\phi) = e^{in\phi}\sum_m \xi_m(r)\, e^{im\theta} \qquad (2.1\text{-}1)$$

What is found is that the longest wavelength, lowest n and m numbered modes are the most unstable (because the stabilizing influence of field line bending is minimized). It can be shown that typically only the m = 3, 2, 1 with n =1 are unstable when the current profile is parabolic and a conducting wall is nearby (see Figure 2.1-1 reproduced from [24]).

In toroidal geometry, even at large aspect ratio, the m numbered modes are coupled because of the θ dependence of the field line curvature as well as the non-circularity of the magnetic surfaces[25]. These effects are increased with increasing pressure, when the plasma experiences a shift towards the outboard side of the tokamak. Hence high ß contributes to kink mode instability. Because the pressure gradient does not enter directly into kink mode stability analysis, the pressure driven and current driven kinks are equivalent in terms of the underlying mechanisms and method for stabilization.

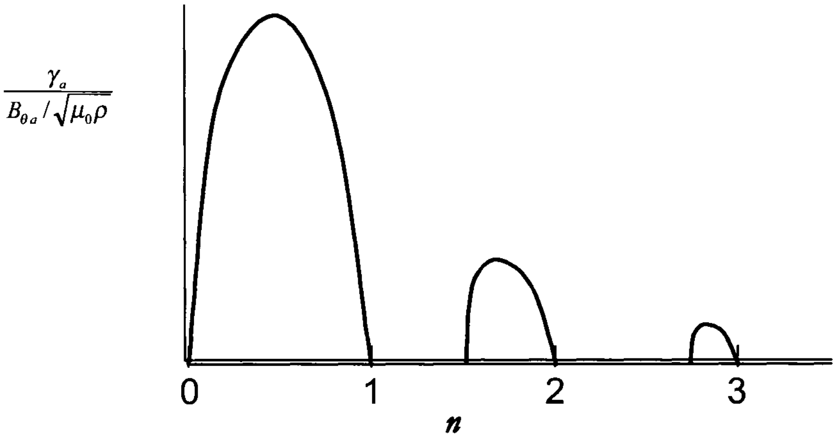

Figure 2.1-1:Kink mode growth vs. edge q in large aspect ratio, low ß approximation

2.2 Resistive Wall Mode

As has already been mentioned, the ideal external kink mode is stabilized by the presence of a nearby ideally conducting wall[26, 27]. If the wall is very close to the plasma surface (i.e. directly adjacent to it), the external kink mode is completely stabilized, even for arbitrary ß and plasma current. This is because the plasma is tied to magnetic field lines, and no magnetic field can penetrate an ideal conductor. In any real tokamak however, the plasma must not contact a wall of course, so a vacuum gap must exist which allows for instability when the energy involved in vacuum field compression in the gap is insufficient to prevent kinking of the plasma column. This is called the ideal wall limit[28]. As the kink develops, it still cannot penetrate the conducting wall, and so the mode saturates with some amplitude, which may be acceptable if it does not lead to disruption or excessive transport. Unfortunately, additional limitations arise because realistic walls are not ideal conductors, but rather metal structures which have a finite resistivity. As a consequence, magnetic fields do diffuse through the wall on a time scale of the inverse eddy current decay rate in the wall, which is usually much slower than the growth rate of an ideal kink in the absence of any wall (the "no-wall-limit"), but still is faster than the characteristic fusion time in a reactor and therefore presents an obstacle to steady state, high ß operation. An external kink mode which is slowed via a conducting wall is then referred to as the resistive wall mode (RWM).

Since the ideal external kink has growth times on the order of the Alfvenic transit time around the torus, but the RWM has growth times that are typically orders of magnitude slower, it is the RWM that is commonly the target of feedback schemes that aim to suppress these modes entirely and raise the beta limit in tokamaks up to the point where the ideal mode is destabilized.

Besides being stabilized by active feedback, the RWM can also be stabilized by plasma rotation[29, 30, 31, 32, 33, 34]. While rotation will certainly play a role in a reactor, it is unclear if a reactor scale plasma can be infused with enough rotational momentum to prevent RWM growth, and therefore feedback stabilization of these modes remains an active topic of research. The questions then arise: What are the requirements for a feedback system to be able to suppress RWM's up to (and perhaps beyond) the ideal wall limit? What geometry and hardware represent the optimum feedback configuration? It is these questions which the HBT-EP tokamak was designed to find answers to.

CHAPTER 3) FEEDBACK CONTROL OF EXTERNAL KINKS

3.0 Feedback Control of Resistive Wall Modes

Feedback and control systems have an extensive history in the field of plasma physics and fusion research[35]. A number of feedback schemes have been proposed and implemented to deal with external kink and RWM instabilities in toroidal plasmas over the past several decades. One of these is known as the intelligent or smart shell[36] concept, in which sensors are located behind a conducting shell facing the plasma. These sensors detect magnetic flux penetrating the shell when the RWM develops and then produce signals that drive control coils which establish magnetic fields that cancel the flux penetrating the walls. In smart shell feedback, each sensor-control coil pair operates independently. The conducting structures thus mimic the behavior of an ideally conducting wall, and the mode is stabilized. Another feedback concept is that of the fake rotating shell[37], wherein magnetic coils respond to the sensor signals with a toroidal phase shift applied which is supposed to give the effect of a rotating wall. There are even ideas by which two walls surround the plasma, one of these rotating rapidly, so that the plasma and the RWM always are stabilized by rotation in one frame or another[38]. This is currently being investigated on the Rotating Wall Machine[39] at Madison, Wisconsin.

In more recent feedback designs, the idea of "mode control" has emerged as a scenario wherein a multitude of sensors strategically placed around the plasma identify the global mode structure(s), so that a set of many modular control coils receives signals that take into account mode information not only locally, but from the entire plasma surface. The control field that is applied is then the result of potentially sophisticated algorithms. For example, the feedback can couple to multiple modes simultaneously[40] or incorporate modern discrimination techniques such as Kalman filtering[41].

The first successful attempt to control kink instabilities in tokamaks with active magnetic feedback occurred nearly thirty years ago on the TO-1 tokamak[42,43,44] using a helical coil covering a quarter toroidal section and a pair of poloidal field sensors, along with relatively simple analog signal processors and amplifiers.

3.1 Optimized Mode Control

Optimization issues in external kink feedback systems deal with questions such as: what are the best locations for sensors to detect the modes, and what type of sensors are optimal? For example, it has been conjectured[45,46] and also demonstrated[47] that magnetic pickup coils are most effective for feedback when these are located close to the plasma, not behind a conducting shell, and when they are oriented to detect the poloidal field component of magnetic perturbations rather than the radial one. This is so because a) the time required for a sensor to register any change in mode amplitude is very long if the perturbed magnetic fields must first soak through a conducting shell, and b) even if the sensor is located in front of such a shell, there can be no radial component to the perturbed field until the field has had time to soak through the shell, because an ideal conductor can experience no change to the normal magnetic field on its surface. Therefore, sensors that measure radial fluxes have a large latency associated with them, which means stabilization will fail when the modes have fast growth rates.

The applied control field issues involve similar considerations: Can a control coil be effective behind a conducting shell? Does the inductive coupling between control coils and passive conducting shells limit the effectiveness of feedback? Clearly, the maximum control power reaches the plasma in the shortest amount of time if the control coils are directly facing the plasma surface, preferably without any conducting structures nearby. For example, consider the case where a conducting shell lies between the control coil and the plasma. For short time scales, and for rapid growth rates of MHD modes, the coil should be configured to drive eddy currents in the shell, which oppose the flux due to the coils. But for slower time scales, the eddy currents decay in the shells and the control coil fields directly interact with the plasma surface. Therefore the sign of the gain of the feedback system is dependent on which frequency regime one is working with. The fact that the gain must change sign precludes such a system from performing what is known as robust feedback[48,49].

Generally, limitations to the feedback system arise from (1) the mutual inductive coupling between control and sensor coils (leading to self-oscillations and ceilings on attainable gain, as well as noise), (2) coupling between the control coils and the conducting shell (leading to finite response time of the system, as well as limiting the stability range over which fixed feedback coefficients are effective), (3) coupling between the sensor coils and conducting shells that slow the response time of the feedback control fields, and 4) other sources of latency in the system, such as the processing time required to send particular output signals to the control coils in response to given input signals. When these limitations are minimized, feedback is known as "optimized mode control." Numerical modeling has predicted external kinks can then be feedback controlled up to the ideal wall limit.[56]

The feedback geometry used for the experiments described in this dissertation represents a realization of optimized mode control and is very different from the smart shell approach that was previously the subject of study on HBT-EP[50].

Figure 3.1-1 schematically contrasts the smart shell and optimized mode-control feedback implementations. For the smart shell, the sensor is strongly coupled to the passive wall and control coil. The control coils are also highly coupled to the wall (and really only coupled to the plasma indirectly). For the mode control case, the poloidal sensors are uncoupled from the wall, and located far from the control coils. The control coils are also directly facing the plasma.

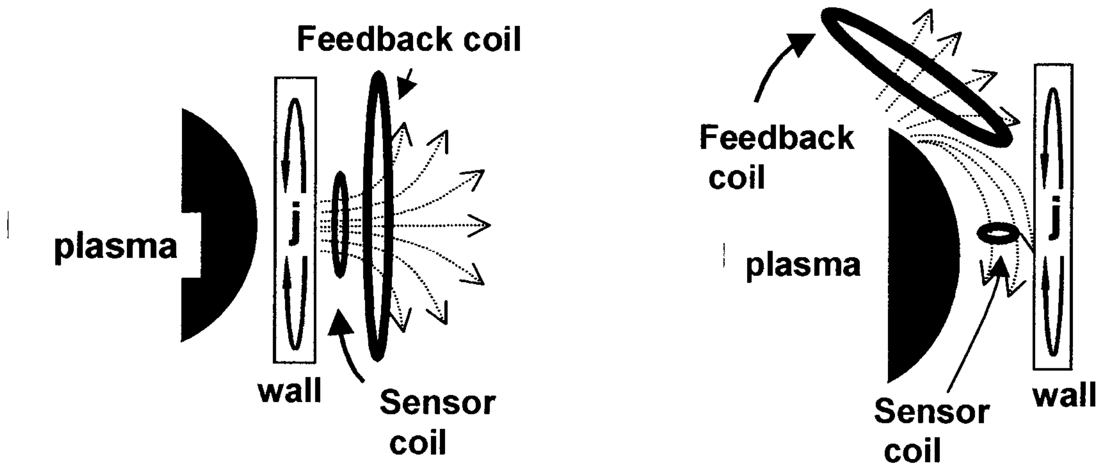

a) Smart Shell b) Optimized Mode Control

Figure 3.1-1: Schematic representation of smart shell vs. mode control configuration

3.2 Modeling of Plasma Response to Feedback

The design of feedback systems for external kink modes in tokamak plasmas calls for some method of predicting plasma stability and plasma response to external perturbations. A number of models have been developed in attempts to quantify the performance of passive and active kink mode control systems[51, 52, 53]. Such models might include the intrinsic plasma stability strength for individual modes, plasma inertia, plasma and kink mode rotation effects, internal plasma dissipation, the influence of external passive conducting structures and control coils, sensor coils, and perhaps even account for coupling between modes of differing poloidal mode numbers. Needless to say, such models can grow to be quite complicated, even when simplifying assumptions about plasma parameters and geometry are made.

Fitzpatrick and Aydemir [54] developed a set of dynamical equations for the current-driven external kink instability in a cylindrical tokamak that aimed to "establish the minimum set of requirements for the stabilization of the resistive wall mode in a rotating tokamak plasma." Their model equations describe a plasma discharge surrounded by a thin resistive shell and are based on the reduced MHD equations with anomalous perpendicular viscosity. In the presence of a single, small-amplitude kink mode, a very thin "skin current" and a thicker "inertial layer" form at the edge of the plasma. The layer geometry used to estimate the effects of viscous dissipation are formally valid only for small dissipation; however, both the resistive kink mode and the wall mode that results from strong viscous dissipation agree with the results of Ref. [55] that were derived with more appropriate assumptions. Fitzpatrick and Aydemir used this model to show that viscous dissipation within the inertial layer can lead to rotational stabilization of the resistive wall mode. A feature of the model is that in rotating tokamak discharges, two kink modes are present: the slowly growing and slowly rotating resistive wall mode and the more rapidly rotating kink-mode. Only one of these two modes can be unstable for a given discharge, and both may be stabilized below the ideal wall limit and for sufficiently fast plasma rotation.

Another method to calculate the interactions between the RWM and the currents in external structures and rotating plasmas has been put forth by Allen Boozer. In the Boozer formalism, the deformations of a plasma surface arising from helical kink modes give rise to magnetic fields outside of the plasma which are unique to the perturbation. The fields in turn can be determined by specifying their normal component at the plasma surface, which sets the boundary conditions for solving Laplace's equations in the vacuum region outside of the plasma. Boozer represents these field normal components at the plasma surface by specifying a set of surface currents on the unperturbed plasma surface, and therefore argues that the surface deformation arising from the kink mode is equivalent to the presence of such surface currents on the plasma surface as far as the external world is concerned. The plasma response can thus be represented as that of an electrical circuit which interacts with the outside world (comprised of other circuits) via induction equations. The effects of plasma dissipation can be incorporated into this model by allowing for a thin resistive shell (a "control surface") just exterior to the plasma, with the choice of resistivity that gives an L/R time comparable to the dissipative time scale in the plasma; the physical mechanism causing dissipation is left out of the model, it is merely a parameter in the equations. In this way, many of the complications of plasma dynamics can be reduced to the electrodynamics of electrical circuits. The unstable plasma is essentially represented by a circuit with negative self inductance.

Further simplifications in this picture are accomplished by assuming linearity in the so-called single mode approximation. This approximation postulates that (near marginal stability) only the least stable mode dominates the response of the plasma/wall/feedback system, and that because the plasma is near marginal stability it thus exhibits a linear response to external perturbations. The plasma response to magnetic flux produced by the external circuits can then be characterized using a relatively simple permeability function, and the explicit plasma mode currents eliminated from the set of equations that describe the system. This is the type of model that is used in the VALEN code[56], a finite element electromagnetic code which takes the output of plasma stability calculations from programs such as DCON[57] or MARS[58], determines the surface current distributions that give rise to the perturbed normal fields in these codes, and calculates growth rates for unstable modes in an environment of passive and active exterior circuit elements. The results from VALEN calculations applicable to the mode control experiments on HBT-EP will be presented in section 5.1.

A brief and simplified overview of the Boozer model follows. The flux in a single mode on the plasma surface is written in a flux evolution equation as:

$$\psi_a = L_a I_a + \psi_x \tag{3.2-1}$$

where L_i is the effective plasma inductance which includes stability information, I_i the perturbed plasma current on the surface, and ψ_x is the flux produced by the external circuits (comprised of both reactive conducting structures and active control coils) on the surface.

The externally produced flux is simply the result of external currents and coupling parameters (mutual inductances). Assuming the plasma can rapidly arrange itself with respect to more slowly varying currents in the external conductors, the perturbed plasma currents are eliminated explicitly from the flux evolution equation using the induction equations for the wall and the control circuits, and the plasma surface flux is reformulated in terms of a plasma permeability:

$$\psi_a = P_a \psi_x \tag{3.2-2)}$$

This permeability is generally a complicated function, even in the single-mode linear theory. Thes equations must be supplemented with the expressions for the magnetic flux at the wall, at the control coils, and at the (fictitious, used to account for damping in the plasma) dissipative shell immediately at the plasma surface,

$$\frac{d\psi_w}{dt} + R_w I_w = 0 \tag{3.2-3}$$

$$\frac{d\psi_c}{dt} + R_c I_c = V_c(t) \tag{3.2-4}$$

$$\frac{d\psi_a}{dx} + R_d I_d = 0 \tag{3.2-5}$$

Together with the knowledge of the coupling parameters between the various circuits (mutual inductances, coupling the circuit equations together since each circuit experiences a flux due to currents in the other circuits), the dispersion relation for external kink modes can be calculated and stability regimes mapped out. Depending on the plasma parameters, certain limits can be taken which often simplify the equations. For example, it is usually true that the wall flux diffusion time is very long compared to the time scale for plasma MHD evolution. This means the RWM branch of the dispersion relation can be treated as a slow evolution of the plasma equilibrium (albeit in three dimensions, suffering a loss of toroidal symmetry), while the ideal kink mode branch operates with the walls behaving like ideal conductors. Furthermore, some plasmas lie in a dissipation dominated regime (as is the case in HBT-EP, presumably the result of collisional damping and charge exchange between plasma and neutral atoms) where the damping rate sets the limit for the speed with which plasma perturbations can grow or respond to feedback, allowing for neglect of any inertial terms in the equations.

Near marginal stability for the RWM, the general forms of the Fitzpaatrick-Aydemir and Boozer equations are equivalent [59], and the model of Fitzpatrick-Aydemir can be reformulated in terms of Boozer's "single mode" model for the RWM near marginal stability. The (linear) Fitzpatrick-Aydemir equations for the perturbed magnetic flux the become[53]:

$$\frac{1}{\gamma_{MHD}^2}\frac{d^2\Psi_a}{dt^2}-\left(\bar{\alpha}+2i\frac{\Omega^2}{\gamma_{MHD}^2}\right)\frac{1}{\Omega}\frac{d\Psi_a}{dt}+\left[1-\bar{s}+i\bar{\alpha}-\frac{\Omega^2}{\gamma_{MHD}^2}\right]\Psi_a=\Psi_x=\frac{1}{\sqrt{c}}\left(\Psi_w+c_f\Psi_c\right) \tag{3.2-6}$$

$$\frac{d\Psi_w}{dt}+\frac{\gamma_w}{1-c}\left(\Psi_w-\sqrt{c}\Psi_a\right)=\gamma_w\Psi_c\left(1-\frac{cf}{1-c}\right) \tag{3.2-7}$$

where the terms involving γ_{MHD} are the so-called "inertial terms" that contain the Alfven wave dynamics of the ideal external kink. The first equation represents the dynamics of the total perturbed magnetic flux at the plasma surface, r = a. The second equation represents the evolution of the total perturbed magnetic flux at the wall.

The various frequencies in these equations are defined as follows: the rate of dissipation, ν_d, the natural mode rotation rate for the ideal kink mode is given by Ω , the ideal MHD kink mode growth rate is given by γ_{MHD}, and finally $\bar{s} \equiv s/s_{crit}$ is the stability parameter related to the strength of the plasma's ability to excite unstable kink modes. When $s < 0$, the kink mode is stable. When $0 < s < s_{crit}$, the RWM can be unstable, unless the plasma rotates faster than a critical rate, $\Omega > \Omega_{crit}$. When $s > s_{crit}$, the kink mode becomes unstable. In the presence of strong dissipation, as observed in HBT-EP, the wall-stabilized kink mode has a growth rate reduced by dissipation. The "non-ideal", or viscous, kink mode in a rotating plasma has a complex growth rate given by $\gamma = i\Omega + (\gamma_{MHD}^2 / \nu_d)(\bar{s} - 1)$. In the lab frame, the real frequency of the mode is Ω and the slow growth rate is $(\gamma_{MHD}^2 / \nu_d)(\bar{s} - 1)$. Shilov and co-workers [60] directly measured the characteristic frequency and damping rate of the kink modes in HBT-EP, and he was able to detect the plasma response associated with both branches that emerge from the roots of the dispersion relation through direct magnetic excitation.

The wall eddy-current decay rate, γ_w, and the plasma-wall coupling, c, are determined by VALEN. The factor cf represents the direct coupling of the control coils to the plasma. The torque parameter, $\bar{\alpha} = -\frac{\nu_d \Omega}{\gamma_{MHD}^2}$, is proportional to the product of the plasma rotation, as well as the anomalous rate of dissipation, ν_d. In the Fitzpatrick-Aydemir equations, dissipation is modeled by viscous dissipation. Chu [31] and Boozer [61, 62] have shown that more general forms of dissipation lead to a dispersion relation for the kink mode that has the identical form of the Fitzpatrick-Aydemir equations. The proper model for RWM-kink dissipation is not known; however, the recent measurements of Sabbagh [63] suggest a viscosity that scales with the edge safety factor, $\nu_d \propto 1/q_a^2$, as expected for neoclassical viscosity [64]. Shilov's experiments demonstrated a consistency between HBT-EP wall-stabilized kink modes and the viscous model of Fitzpatrick-Aydemir although he did not exclude other possible dissipation mechanisms. The unresolved questions regarding the origin of dissipation are not the subject of this thesis, however, and are left to be answered by others.

3.3 Optimized Feedback Hardware on HBT-EP

The HBT-EP mode control feedback system is depicted in

Figure 3.3-1. The machine has twenty sets of moveable shells at ten toroidal positions (one shell on the bottom, one on the top). At five of these positions, spaced 72° apart, the shells are made from 1.4 cm thick aluminum. These have been used in the past to passively stabilize external kink modes[65] by moving them close to the plasma surface, as they are such good conductors that their L/R time is 60 msec, many times longer than a typical tokamak pulse length (τ < 10 msec). Adjusting the positions of the wall segments allows adjustment of the plasma-wall coupling (and the ideal wall stability limit) and effective wall current decay rate, γ_w. When the Al segments are moved from the fully withdrawn to fully inserted position, the stability parameter value foe the ideal wall limit doubles, and γ_w decreases from 6.3 ms^{-1} to 2.3 ms^{-1} for $m/n = 3/1$ modes.

The ten remaining shells, interspersed between the thick aluminum shells, are made from stainless steel and are only 0.2 cm thick. Their eddy current decay time has been measured to be ~300 μsec, which enables RWM to fully develop during a discharge. Upon these are mounted various sensor and control coils. The experiments described in this dissertation were conducted using a subset of these coils, i.e. the mode control coils.

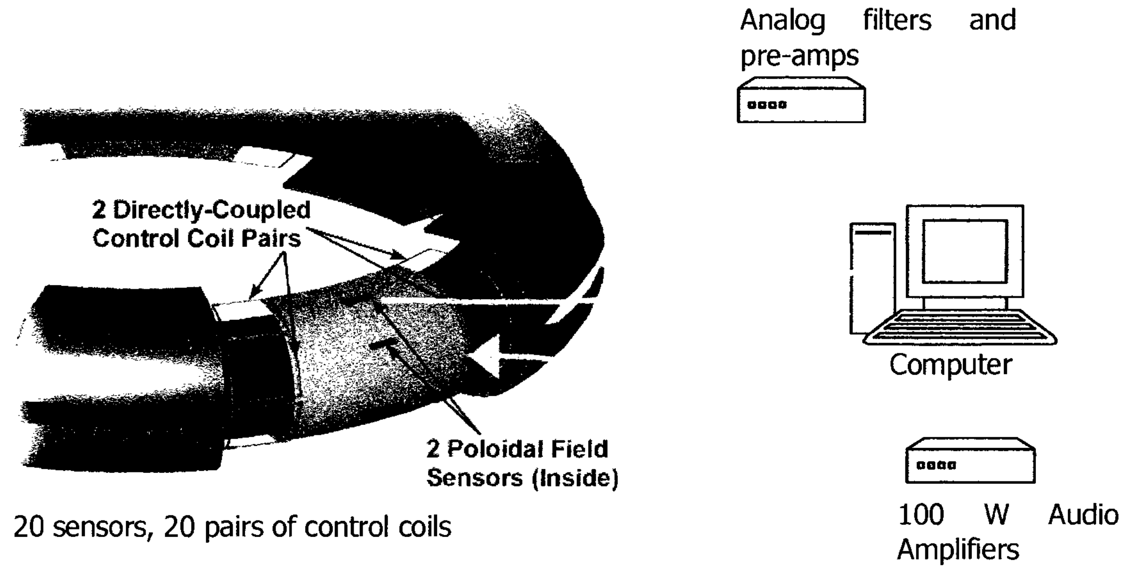
Analog filters and pre-amps
2 Directly-Coupled Control Coil Pairs
Computer
2 Poloidal Field Sensors (Inside)
20 sensors, 20 pairs of control coils
100 W Audio Amplifiers

Figure 3.3-1: Mode control feedback system as implemented on HBT-EP

The mode control coil set consists of the following: Twenty poloidal sensors are mounted at five toroidal locations and 4 poloidal angles on the inside (plasma facing side) of moveable stainless steel shells. Because they measure poloidal magnetic fluctuations, the sensors can measure kink perturbations even for time scales short compared with the SS wall's magnetic diffusion time. The sensors consist of 15 turn rectangular loops with an active area of 7 mm x 101 mm. When the plasma is centered at R = 92 cm, the sensors are located at poloidal angles ± 27° and 83° on the outboard side.

The feedback control coils are constructed from 16 turns of wire in a rectangular loop of 121 mm x 160 mm and are mounted in the gaps between the aluminum and steel shells (see Figure 3.3-1) , on wings of very thin stainless steel shim stock. For all practical purposes, the shim stock is transparent to fluctuating magnetic fields, so that the applied radial fields may couple directly to the plasma. A total of forty control coils are arranged at four poloidal locations and at ten, equally spaced, toroidal positions. Each pair of control coils mounted on the same segment and at the same poloidal position is connected in series. The mutual inductance between the poloidal sensors and the feedback coils has been measured to be negligible.

The arrangement of sensors, control coils, and passive shell segments as described above represents one of the most optimal ways to construct a feedback system, because the inductive coupling between sensors and control coils/shells as well as the coupling between control coils and shells is minimized, while the coupling between plasma and sensors as well as control coils is maximized.

CHAPTER 4) SYSTEM CHARACTERISTICS

4.0 Mode Control Signal Processing

The way in which signals from the poloidal sensor arrays are processed will now be described explicitly. Mode control feedback is achieved by detection of the $n = 1$ toroidal component of the perturbed poloidal field at each of the four poloidal angles and applying, in proportion, a toroidally-rotated $n = 1$ radial field using the control coils. First, the sensors signals are amplified and filtered using analog circuitry, and then digitized to 16-bits for input to multiple, high speed field programmable gate arrays (FPGA)[66]. Data is sampled with a sample interval, $\tau_s = 10\ \mu s$. After temporal filtering (described in the next section), the five sensor signals at each of four poloidal positions are grouped together and digitally processed to select the $n = 1$ component of the measured magnetic field perturbation. The $n = 1$ component is isolated using a discrete Fourier transform (DFT), while the $n = 0$ and $n = 2$ components are disregarded. Each poloidal group is processed independently from the others, and the toroidal phase at each poloidal angle is determined by the $n = 1$ mode at each poloidal location. Because the toroidal phase of each poloidal group is completely independent of the others, the system is sensitive not to one particular m numbered perturbation, but rather allows for the handling of multiple modes and complicated poloidal mode structure. The floating poloidal phases also automatically adjust to a change in poloidal mode structure caused by evolution of the plasma equilibrium. For example, if the plasma changes radial position, or if beta increases cause increased ballooning or other distortions of the mode structure (see section 5.0), the feedback system automatically adjusts to perform feedback optimally since toroidal symmetry is preserved in any of these scenarios.

In the software, a rotation operator is used to generate the appropriate toroidal phasing of the radial control fields, and finally an inverse DFT produces control signal outputs that are sent to 100 Watt audio amplifiers. Except for the temporal filter, the entire digital algorithm is implemented as a 5 by 5 matrix multiplication,

$$\overline{V_c} = G \times \left(\overline{\overline{T^T}} \times \overline{\overline{R}} \times \overline{\overline{N_1}} \times \overline{\overline{T}} \right) \bullet \overline{\delta\Phi_s} = \overline{\overline{\mathrm{A}}} \bullet \overline{\delta\Phi_{\mathrm{s}}} \qquad (4.0\text{-}1)$$

where V_c is the control coil voltage, $\delta\Phi_s$ is the poloidal field sensor flux, T is the discrete Fourier transform operator, N_1 represents n = 1 mode isolation, R accomplishes a toroidal rotation, and G is the effective overall system gain. Because the final algorithm is so simple, and because operations in the FPGAs are performed in parallel, the matrix processing in eqn. 4.0-1 can be accomplished in a few tens of nano-seconds. However, the system latency is limited by the Analog to Digital conversion times to be approximately 10 μs.

4.1 Hardware Specific Transfer Functions

Any feedback system that controls an unstable process with complex growth rates must be designed to possess an amplitude and frequency response that can cope with the band of frequencies and the range of real growth rates as they occur in the process in order to ensure stability. For example, if the process has a complex growth character that can be written as $e^{\gamma t} = e^{(i\omega+\delta)t}$, with ω being a (real) rotation frequency and δ a real growth rate, then the force applied to this process must be phased properly to oppose any perturbation (i.e. force must be in the proper direction) and have a magnitude strong enough (gain) and a latency period short enough to prevent the growth of the instability. This is the situation for external kink modes on HBT-EP which rotate toroidally as they grow in amplitude, and thus have complex growth rates.

Without consideration of the digital portion of the feedback loop, the mode control feedback system incorporates several stages of analog circuitry and reactive coils that cause the amplitude and frequency response of the open-loop system to be less than optimum. Optimum would mean that the gain and phase shift for the signals passing through the system are the same for all relevant frequencies. If that were the case, the rotation operator in the FPGA processor could simply be set to provide the proper phasing of the control coil currents with respect to the perturbed magnetic fluxes, and the system would perform negative feedback for all frequencies at fixed gain. Unfortunately, drastic variations in the system transfer function occur in the frequency range of interest. Therefore, a digital phase compensation scheme is implemented to improve the transfer function of the system for a relatively wide frequency band. This band includes all external kink mode rotation frequencies as they are observed on HBT-EP, nominally 1-10 kHz.

Analytic expressions for the amplitude and phase response of the open loop system were derived by estimating or measuring the reactive contribution of all electronic components that lie in the signal path. Any amplifiers were assumed to be ideal, i.e. they only effect a constant gain for all frequencies without distortion. The only digital aspect that was included in the calculations was the phase shift due to digitization latency, which is always present in the system regardless of what sort of algorithm is running in the FPGA. The theoretical transfer functions constructed from these calculations were then verified (measured) by sending pure sinusoidal signals as an input for a range of frequencies, component by component and also for the entire system. The components that introduce phase shift and frequency dependent amplitude variations of any significance are: A) the poloidal sensor coil, B) a DC blocking RC high pass filter, C) an RC low pass filter on the input stage of the analog boards, and D) the self inductance of the control coils. The analog filtering stages were retained merely because they could not easily be removed from the existing circuitry (circuitry which was previously used to implement smart shell feedback).

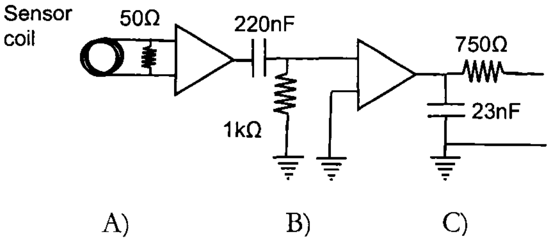

Figure 4.1-1: Simplified schematic of input stage circuitry before digitization

A poloidal sensor coil consists of a 12 turn copper coil with a measured self inductance of ~12.8 μH, and a resistance of 2.5 Ω, placed in series with 50 Ω input resistance on the analog board. Consequently, the coil behaves as an ideal B-dot probe for frequencies << 2 MHz. The values of the capacitors and resistors in the circuitry were measured directly for some of the channels. After the digital portion of the control loop, several amplifier stages do not add significant phase shift or frequency dependent gain for frequencies between 50 and 40,000 Hz. The main amplification occurs in high quality audio amplifiers that exhibit a very flat frequency response up to 40 kHz. The only reactive element is the control coil itself, which is a set of two coils connected in series. The self inductance of these was measured to be 255 μH, with a resistance of 4 Ω. A small resistance and inductance is also present in the wiring from the amplifiers to the coils within the vacuum chamber.

An example of the transfer measurements is shown in Bode plots in Figure 4.1-2 and Figure 4.1-3, for the circuitry up to the digitization stage. The plotted points represent measurements; the solid line is the analytic expectation. The analytic expressions for gain and phase were largely validated by the measurements and used subsequently to design digital filters. The total system transfer functions in the absence of digital processing are depicted in Figure 4.1-4 and Figure 4.1-5.

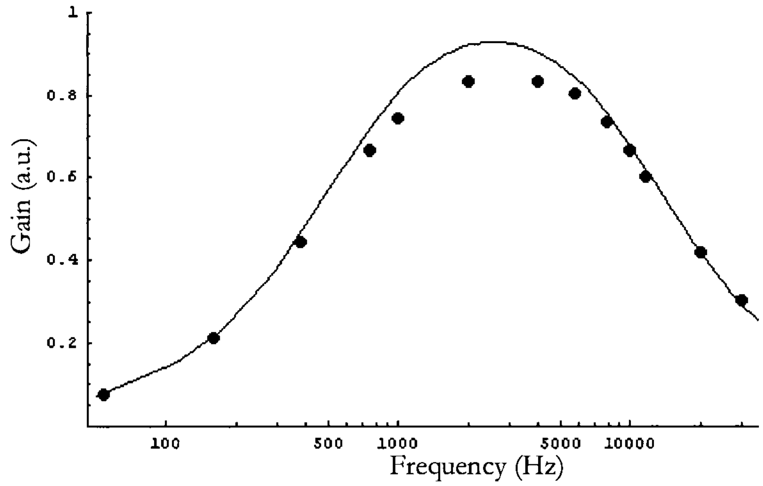

Figure 4.1-2: combined RC filter network on analog board: amplitude transfer function

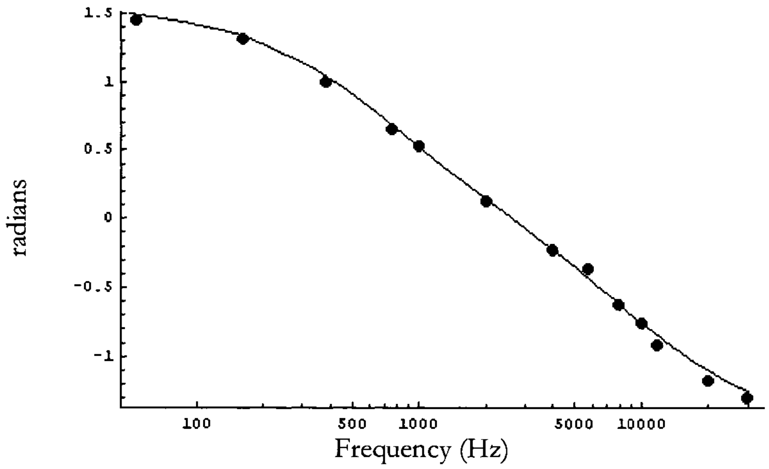

Figure 4.1-3: combined RC filter network on analog board: phase transfer function

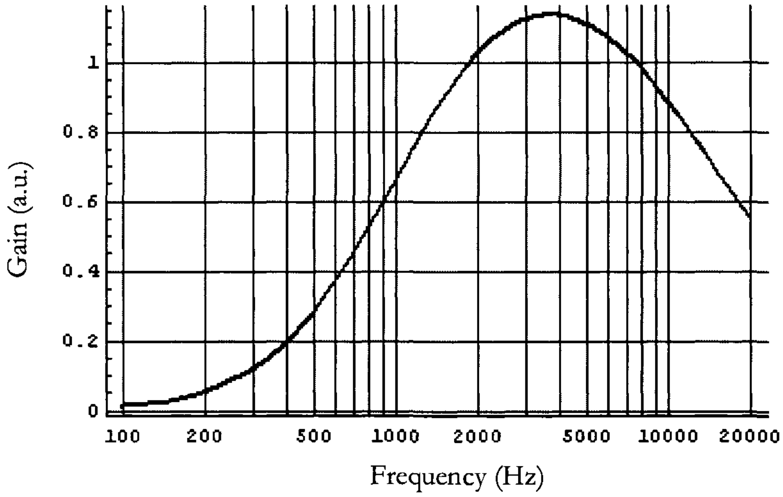

Figure 4.1-4: Amplitude transfer (flux-flux) for feedback system without digital filtering

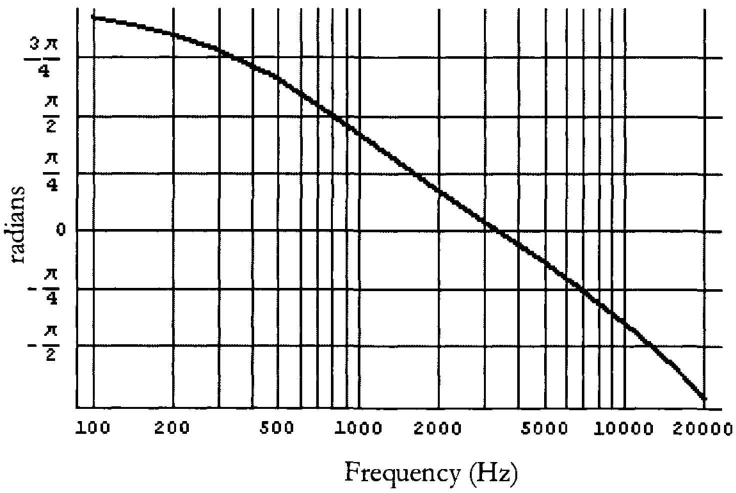

Figure 4.1-5: Transfer function phase shift for feedback system without digital filtering

Apparent in the bode plots for the base transfer functions (without digital filtering) is that a) the amplitude transfer is acceptable in the 1-10 kHz region, and does not vary more than a factor of two, but b) the phase shift is widely varying in the frequency band of interest, as it changes by more than 180° and consequently will make positive feedback on a consistent basis difficult if and when the plasma modes change their rotation frequency. This predicament calls for some kind of compensator.

4.2 Phase Lead/Lag Compensation

In control applications, compensators that shape the open loop transfer function of the system can be of various types, which include PD (proportional and derivative), PI (proportional/integral) and PID (a combination of the two) compensation. However, these can lead to a gain divergence at the high end of the frequency spectrum or radical phase changes at the low end. Another type of compensation is achieved with so-called phase lead and phase lag compensators. Their transfer function is represented in the Laplace s-domain by $G_c(s) = \alpha \frac{s+z}{s+p}$, where $|z| < |p|$ for phase lead, and $|z| > |p|$ for phase lag compensators.

A Mathematica code was written to determine the best lead/lag compensators to shape the mode control feedback transfer functions. The code finds the coefficients for two cascaded first order filters by calculating and minimizing the phase changes of the total resultant transfer function in the 1-10 kHz region. The results produced amplitude/gain effects however which were found to be unacceptable at high and low frequencies. A better method seems to be to design a phase lead and lag compensator in the s-domain by adjusting the zeroes and poles manually until the results look acceptable. I picked the following:

$$G_{lead}(s) = 5.7\,\frac{s+35000}{s+200000}$$

and

$$G_{lag}(s) = 0.93\,\frac{s+16200}{s+1500}$$

These functions compensate for the significant phase change in the 1-10kHz region due to the analog components. Using the bi-linear transform method†, the digital approximations to these functions were determined. Then small manual adjustments were made to the digital filter coefficients, until a reasonable outcome was achieved. In the digital domain, because the system is discrete, the transfer function of the system is described by the so-called z-transfer function. Explanations of digital signal processing terms and methods can be found in the in the two references on digital filters[67,68].

The final FPGA z-transfer function in these calculations for the compensator then is:

$$G(z) = K\,\frac{0.4 - 0.6208\,z^{-1} + 0.2387\,z^{-2}}{1 - 0.975\,z^{-1} - 0.00985\,z^{-2}} \qquad 4.2\text{-}1$$

This is a second order filter, easily implemented (K is simply a gain coefficient). It requires a loop algorithm where the previous two input samples and output samples are mixed together with the current sample to produce the new output. The coefficients are derived from the equation above. In some sense, the filter uses quite a bit of integral action, and moderate amounts of derivative action. Because the poles of the z-transfer function lie within the unit circle, the filter is stable.

---

† See a text such as A. Anoniou, Digital Filters: Analysis, Design, and Applications (1993)

With a good base digital filter to start from, an attempt was made to optimize the algorithm to yield the flattest possible phase shifts in the transfer functions from 1 to 10 kHz. The algorithm is implemented as a difference equation, expressed as

$y_n = a_0 x_n + a_1 x_{n-1} + a_2 x_{n-2} + b_1 y_{n-1} + b_2 y_{n-2}$, where y_n stands for the n-th sample output, x_n the n-th sample input, etc.

An IDL code was written which varied the coefficients of the terms within reasonable ranges (stability was a requirement) and then used cost functions which assigned penalties to regions where the phase shift of the resultant function deviated from the phase at 4 kHz in proportion to the deviation. The code then maximized the integral of the phase transfer in the 1-10 kHz band. Several cost functions were tried, among them:

$$C(\Delta\phi) = \frac{A}{A_{\max}} Cos(\Delta\phi),\quad \frac{A}{A_{\max}} Cos^3(\Delta\phi),\quad \frac{A}{A_{\max}} Cos^5(\Delta\phi),\quad \frac{A}{A_{\max}} Cos(\Delta\phi)\cdot e^{2\,Cos(\Delta\phi)},$$

$$\text{and}\quad \frac{A}{A_{\max}} Cos^3(\Delta\phi)\cdot e^{2\,Cos^3(\Delta\phi)}$$

The resultant transfer functions appeared to be very similar to those obtained with the original filter that had been designed by hand, regardless of which cost function was used. The various cost functions and some of the resultant total system transfer functions are graphically depicted in Figure 4.2-1, Figure 4.2-2, and Figure 4.2-3. The second order digital filter performing phase lag/lead compensation was found to be very effective in shaping the transfer function of the open loop system and was used for the subsequent feedback experiments.

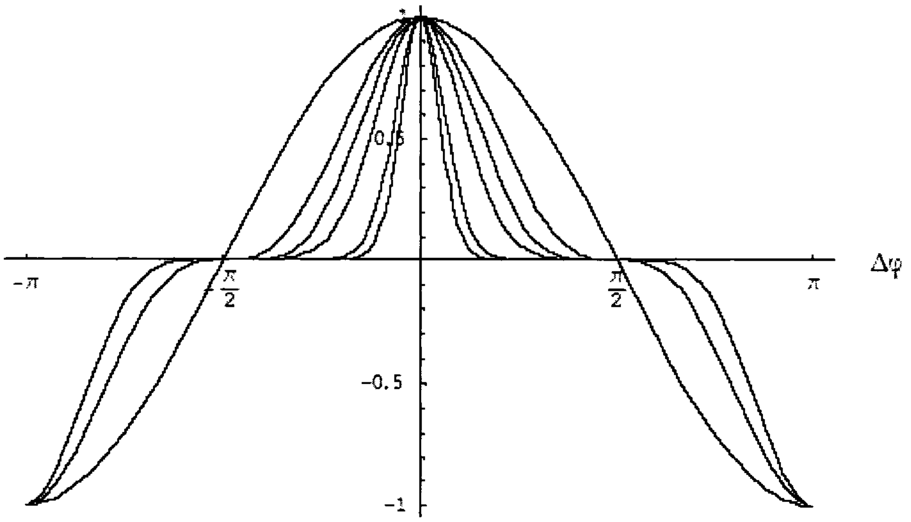

Figure 4.2-1: Cost functions used to optimize digital phase lag/lead compensation filter

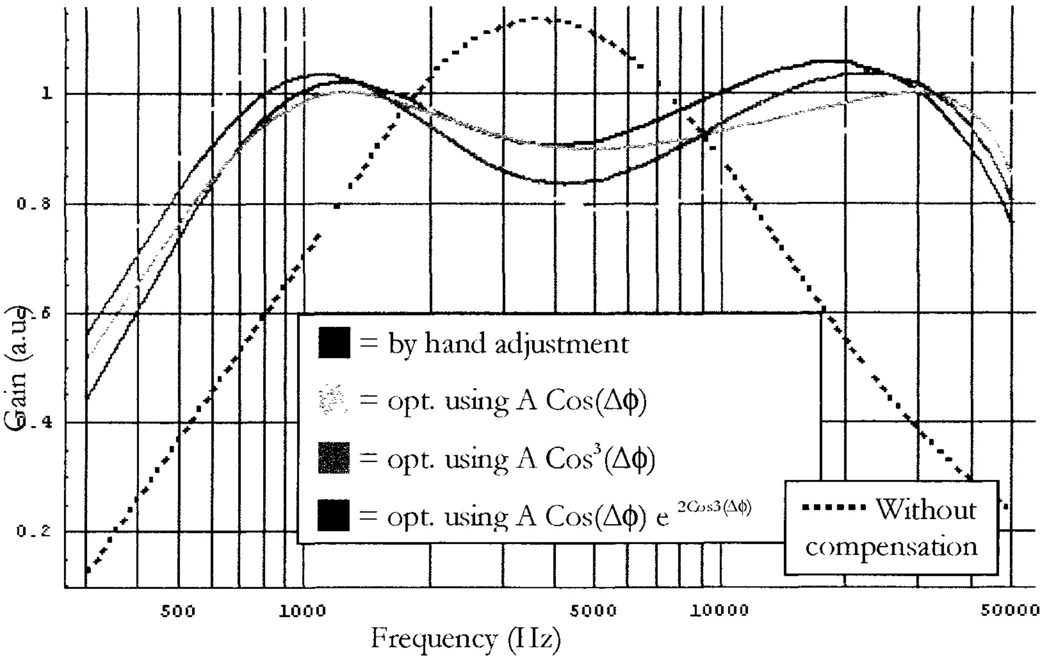

Figure 4.2-2: Amplitude transfer function for phase lag/lead compensators designed with cost functions

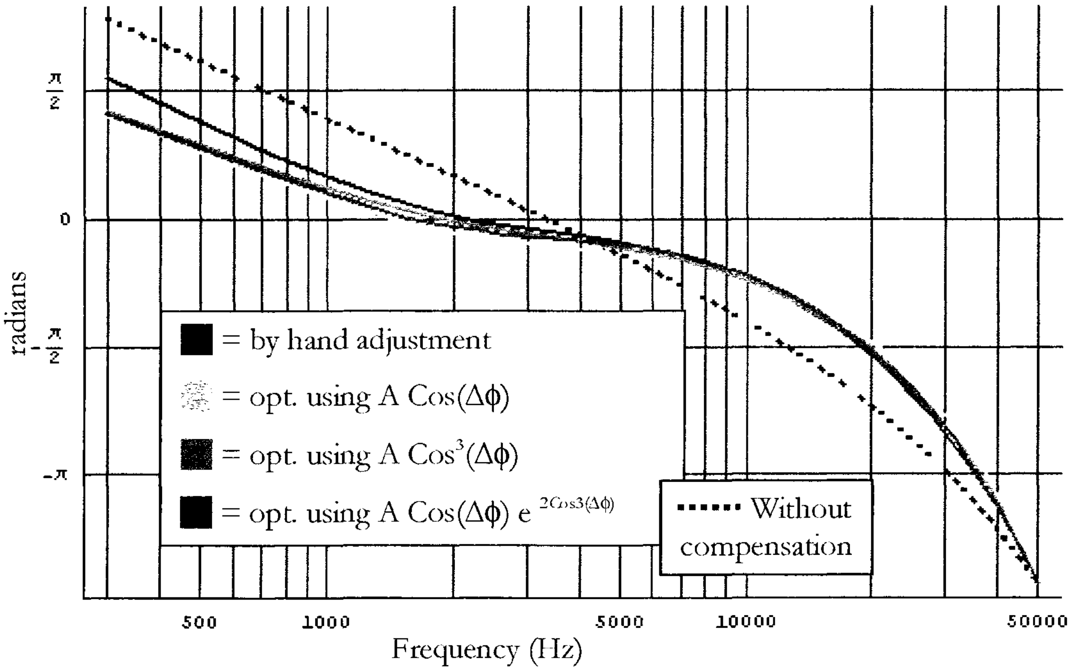

Figure 4.2-3: phase transfer function for phase lag/lead compensators designed with cost functions

4.3 Gain

In order to characterize the available gain in the feedback system, the term "gain" must first be properly defined. Preferably, this should be done in a way which can apply to feedback systems on other devices, to allow for meaningful comparisons and to give intuitive insight into the strength of the feedback.

Such a definition of gain is a dimensionless ratio of sensor flux to control flux. To calculate the flux-to-flux gain of the system, the fluxes must be defined over equal areas, otherwise the calculation is not directly comparable to other coil and plasma geometries. That is to say, if a small sensor experiencing small local magnetic flux causes a response on large control coils to produce a large magnetic flux (due to large coil size), it appears at first glance that the system has relatively high gain. This is misleading however, because the sensor only samples the flux produced by the external kink mode in a small portion of the total surface over which such flux is produced. Therefore, to properly characterize the system in terms of flux-to-flux gain, a surface that encloses the entire plasma must be used to calculate the flux resulting from mode growth. Similarly, the flux produced by the control coils must be evaluated over that same entire surface.

For the mode control system on HBT-EP, the poloidal sensor coils produce ~ 1 Volt of signal into 50 Ω when the local magnetic field strength is 3.7 Gauss, with the field fluctuating at a frequency of 5 kHz (the sensor measures changing flux). This signal level represents the maximum level of fluctuations in a typical discharge. The control coils are powered by audio amplifiers with limited power. The maximum voltage that these can deliver is 42 Volts, which at 5 kHz corresponds to a maximum current in the control coils of about 6 Amperes. This in turn produces an average of about 10 Gauss over the area of the control coils, which is of course much larger than the area involved with the sensor coils.

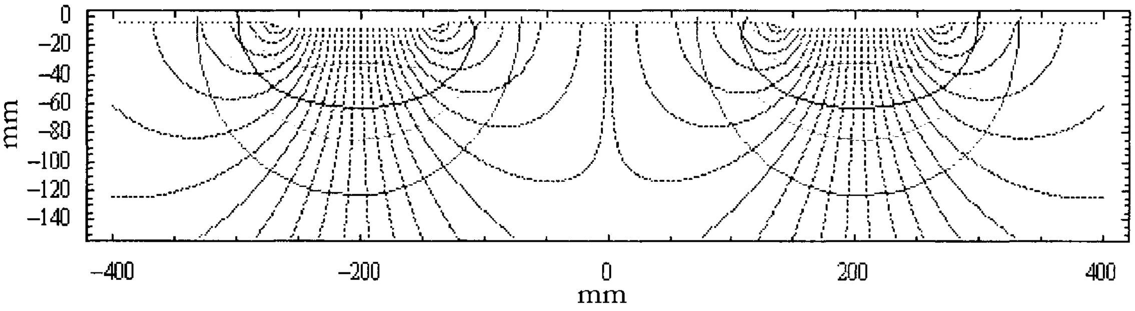

Figure 4.3-1: Magneto-static analysis of single coil pair showing field strength (contours of 2, 4, 6, 8, 10 Gauss shown) and magnetic field lines for 10 A of current in the coils

The flux produced by a particular m/n mode is unique to that mode, so that one can speak of an eigenmode which produces an "eigenflux". For example on a cylinder, any surface function can be expanded in a Fourier series of functions, and the perturbed flux on a surface can be mapped onto the eigenfunctions to resolve the m/n components of the current distributions on the cylinder. In a torus, the analysis is not so straight forward because of coupling between the poloidal harmonics. Nevertheless, one can assume that when one particular mode is unstable, it is the only mode that needs to be considered (especially in a large aspect ratio tokamak) and a Fourier-like set of functions adequately represents the set of eigenfunctions that make up the mode structures, each proportional to $e^{i(n\phi-m\theta)}$. As will be seen in the experimental sections, the particular kink mode observed in the discharges in the experiments is predominantly of wave number m/n =3/1. The system gain is estimated for the n = 1, m = 3 external kink mode by evaluating the mode fluxes (due to plasma perturbations as well as control coil currents) on a surface just outside of the plasma. This was done as follows:

Allen Boozer[69] has shown that the deformation associated with an external kink mode in a torus gives rise to a magnetic field which is indistinguishable from that produced by a current on the un-deformed plasma surface. The plasma column produces a mode flux in proportion to the strength of the kink perturbation. Since the sensors measure the magnetic field just 1 cm from the plasma, it is relatively easy to calculate what the total flux is on the surface just outside of the plasma. For a cylindrical column, any perturbed current distribution along the axial direction gives rise to a magnetic field outside of the cylinder which can be written as

$$\vec{B}(r) = \sum_m m \frac{\mu_0 I_m}{2r_a} \left(\frac{r_a}{r} \right)^{m+1} \left[\cos(m\theta)\hat{r} + \sin(m\theta)\hat{\theta} \right] \tag{4.3-1}$$

where m's refer to the poloidal mode numbers and I_m is the surface current amplitude in the mth mode. The important aspect of this expression for the magnetic field is that it falls off in the vacuum region as $r^{-(m+1)}$. Assuming that the cylindrical model is fairly accurate for the large aspect ratio tokamak near the plasma surface, and taking m = 3, a plasma major radius of 92 cm, minor radius of 15 cm, and knowing the sensor position is at r = 16 cm, one can deduce that the field has decayed to 77% from the value at the plasma surface to the location of the sensors. It remains merely to calculate the magnetic field everywhere on the surface based on a few sensor coil measurements, with some additional considerations:

The cylindrical expressions are modified for toroidal geometry. Fussman[70] has derived an analytic expression for the magnetic field of current perturbations in a large aspect ratio torus, which to first order is given by:

$$\overline{B_m}(r)=\frac{\mu_0 j_{mn} r_a}{2}\left(\frac{r_a}{r}\right)^{m+1}\left[\cos\left(m\theta^*-n\phi-\omega t\right)\hat{r}+\sin\left(m\theta^*-n\phi-\omega t\right)\hat{\theta}\right] \qquad (4.3\text{-}2)$$

where the poloidal angle is modified in the following way:

$$\theta^*=\theta-\lambda\sin\theta \qquad (4.3\text{-}3)$$

with $\lambda=\frac{r_a}{R}(1+\frac{l_i}{2}+\beta_\theta)$, where l_i is the normalized plasma inductance and β_θ the poloidal beta at the plasma surface. The normalized plasma inductance is a measure of the peakedness of the current profile, with $l_i = 1$ for a singular current on the magnetic axis, and $l_i = 0$ for a hollow current profile with all of the current concentrated near the plasma surface. The poloidal beta is simply the ratio of pressure to the poloidal magnetic field pressure. A reasonable estimate for the ballooning parameter _ in the discharges under consideration on HBT-EP is about 0.3, and will be discussed further in Chapter 7. The modified poloidal angle accounts for ballooning on the outboard side of tokamak due to toroidal and finite pressure effects.

Secondly, the measured magnetic field B ~ 3.7 Gauss (poloidal) at the sensor is partially due to eddy currents in the shell upon which the sensor is mounted. These eddy currents add to the poloidal field, to 0th order they completely null the radial field components and produce an additional poloidal field of equal amplitude as that produced by the plasma, so that the field due purely to the perturbed plasma kink is taken to be roughly 50% of the recorded value.

A Mathematica code was written (which made use of the Radia package[71] from the ESRF facility in Grenoble) to calculate the radial magnetic flux on the plasma surface due to an $m/n = 3/1$ mode on that surface when the control coils are driven to produce fields with these mode numbers. That flux was projected onto the $m/n = 3/1$ eigenfunction for the torus, given by: $\psi_{3/1} = \sqrt{2}\cos\left(3\theta^{*} - \phi\right)$ and is defined by:

$$\Phi_{\text{plasma}} = \int_{\text{surface}} \psi_{m/n}\, \vec{B} \cdot d\vec{a} \tag{4.3-4}$$

The normal component of that flux is illustrated in Figure 4.3-2. The normal component of the flux on the plasma surface is then calibrated using the poloidal sensor measurements.

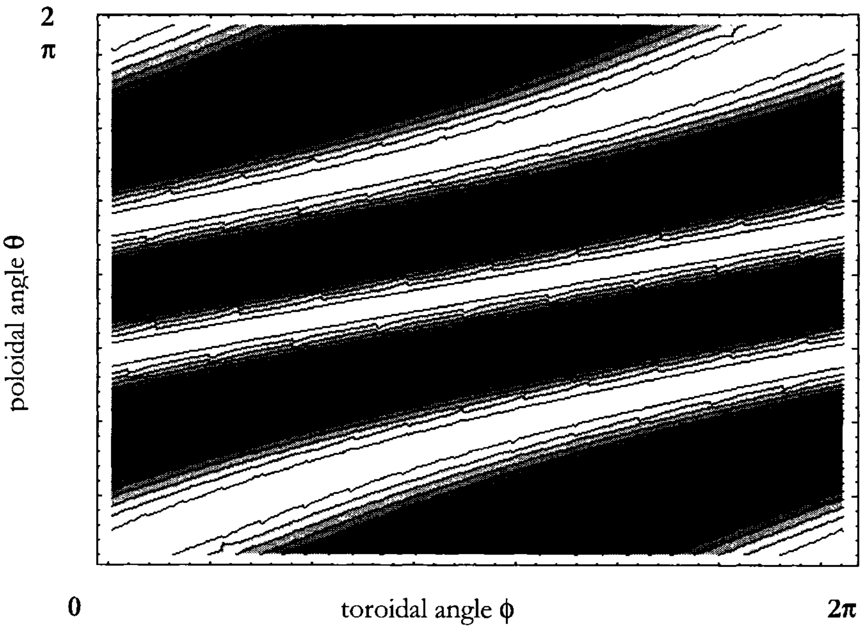

Figure 4.3-2: Contour plot of $m/n = 3/1$ mode flux produced by perturbed plasma currents

To compute the flux produced by the control coils, a model was created which placed the coils at realistic positions and calculated the magnetic field on the plasma surface produced when the coil array was phased appropriately to produce the maximum 3-1 radial flux and powered with 6 Amperes. In the model the control coils are arranged in space with $R = 92$ cm and $r = 16$ cm. The magnetic field is calculated on 52,000 points on the plasma surface, which is located at $r = 15$ cm. A picture of the model is given in Figure 4.3-3, which shows the surface over which the flux was computed as well as the position of the control coils. The resultant flux is graphically depicted in Figure 4.3-4.

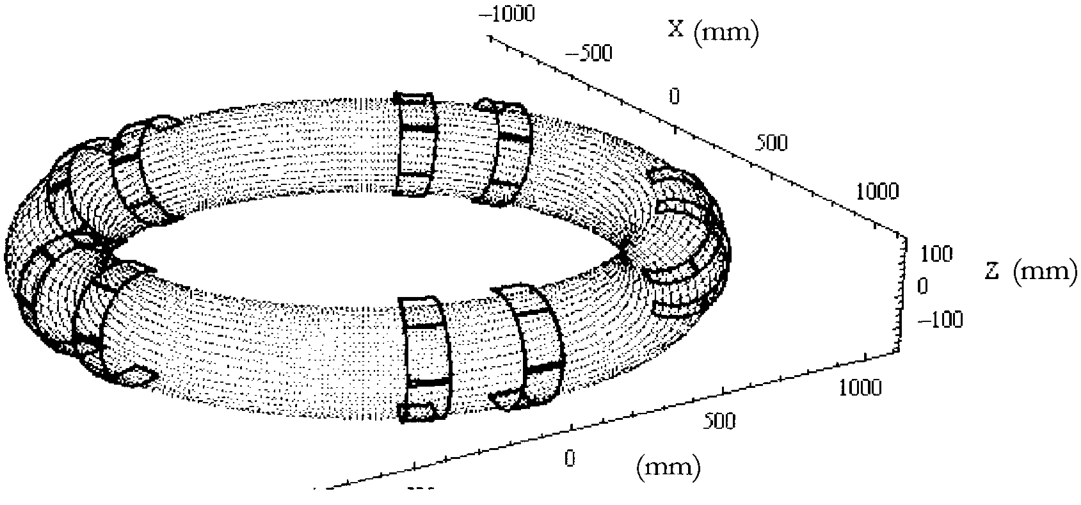
-1000
-500
0
500
1000
X (mm)
100
0
-100
Z (mm)
1000
500
0
(mm)

Figure 4.3-3: 3D depiction of model for control coil flux produced on plasma surface.

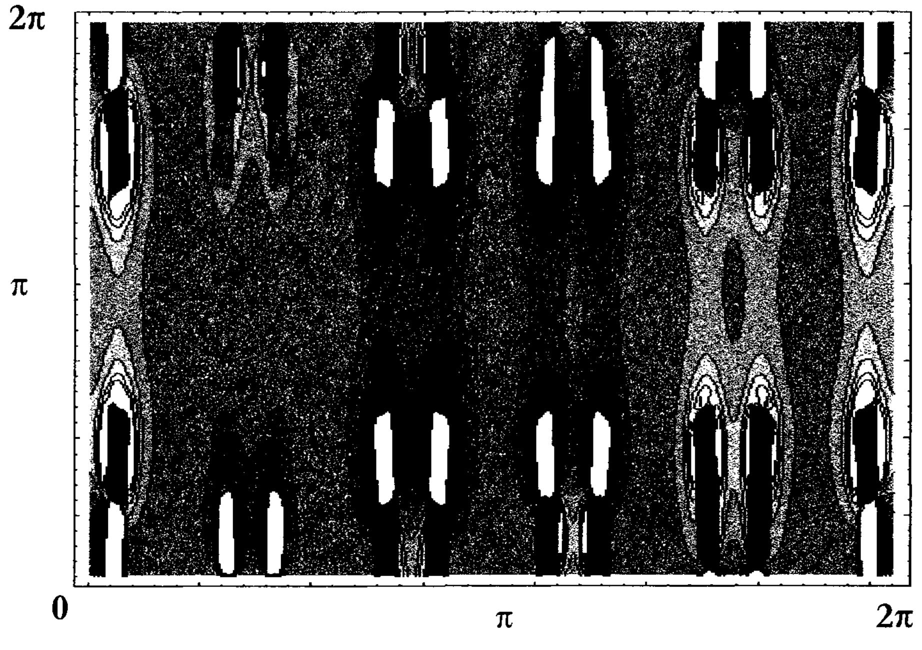

Figure 4.3-4: Contour plot of flux produced by control coils vs. poloidal and toroidal angles

The 3-1 total flux is evaluated using

$$\Phi_{\mathrm{ccoil}} = \int_{\mathrm{surface}} \psi_{m/n} \vec{B} \cdot d\vec{a} \tag{4.3-5}$$

and the gain of the system evaluated:

$$G_{3/1} \equiv \frac{\Phi_{ccoil}}{\Phi_{plasma}} \approx 0.25 \tag{4.3-6}$$

Finally, the amplitude of the perturbations for external kink modes is much larger on the outboard side of the tokamak, partially due to toroidal geometry, but largely due to the relative strengths of the equilibrium field on the inboard vs. the outboard side. As will be seen in section 5.1, a more detailed equilibrium analysis reveals that the perturbed magnetic flux is nearly a factor of five larger on the outboard side. Since the control coils are all arranged on the outboard side as well, it might be reasonable to weight the control coil flux on the outboard side more heavily when calculating the gain of the system. With all the assumptions, approximations, and uncertainties in these calculations, the result is only indicative of the order of magnitude of the gain: it is found to be approximately unity, $G_{3/1} \approx 1 \pm 50\%$. This calculation applies to feedback shots with maximum signal levels and amplifier settings as high as possible without causing distortion.

The pre-amplifiers in the control loop are capable of much higher gain than what is possible to use in an experiment. With infinite power in the control coil amplifiers, the system gain is ultimately limited by the small mutual inductance that is present between the control coils and the sensor coils and imperfections in the construction geometry. In practice it was determined that the feedback system starts to self oscillate at high frequencies when the gain is increased to $G_{3/1} \approx 10$, as is described below.

Vacuum shots with an initial seed pulsed magnetic field (using the vertical field of the equilibrium field coils) reveal what the maximum achievable gain in the mode control geometry is. With the feedback system turned on at t = 1.5 msec, miniscule residual magnetic perturbations are picked up by the poloidal sensors which drive the control coil arrays. In Figure 4.3-5 the output currents are shown for the bottom poloidal group with a normalized gain setting of 1 (representing the maximum gain that can be used during plasma operation without saturating the available amplifier power): in the absence of plasma noise, the feedback system remains quiet. At gain settings of 10, the limit of the available gain starts to become evident as seen in the feedback coil output. For a gain setting of 40, the system becomes unstable, and the sensors pick up a component of the control coil flux which leads to self oscillations at about 16 kHz. The higher gain setting data is shown in Figure 4.3-6 and Figure 4.3-7, again for the currents in the bottom poloidal group. Additional filtering may be able to reduce the coupling between control coils and sensors still further.

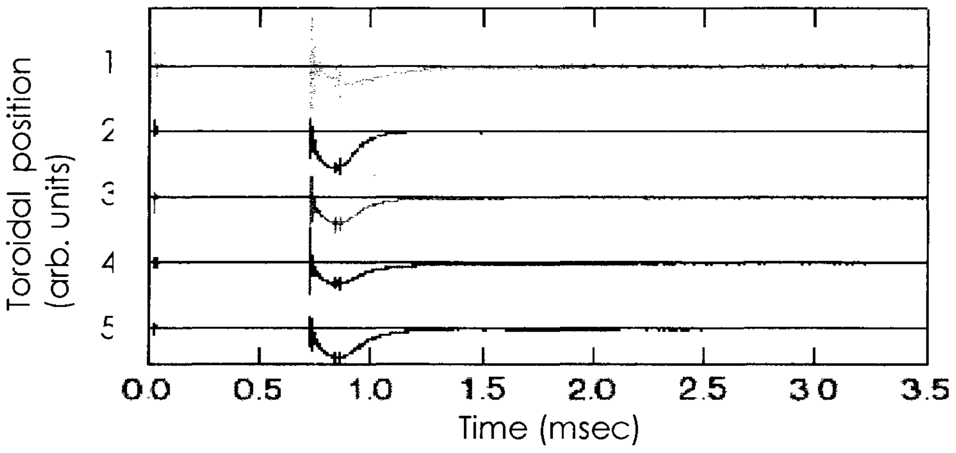

Figure 4.3-5: Control coil currents for vacuum shot with normalized gain G = 1 (as used in subsequent experiments)

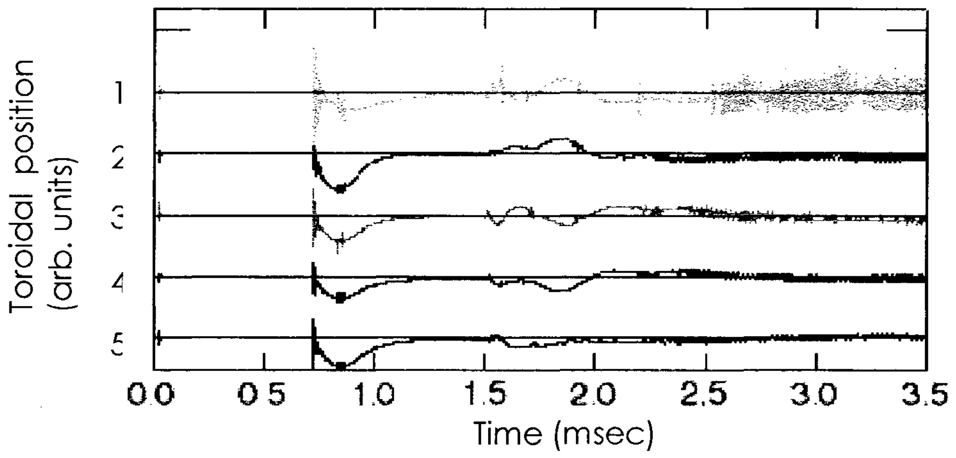

Figure 4.3-6: Control coil currents for vacuum shot with normalized gain G = 10

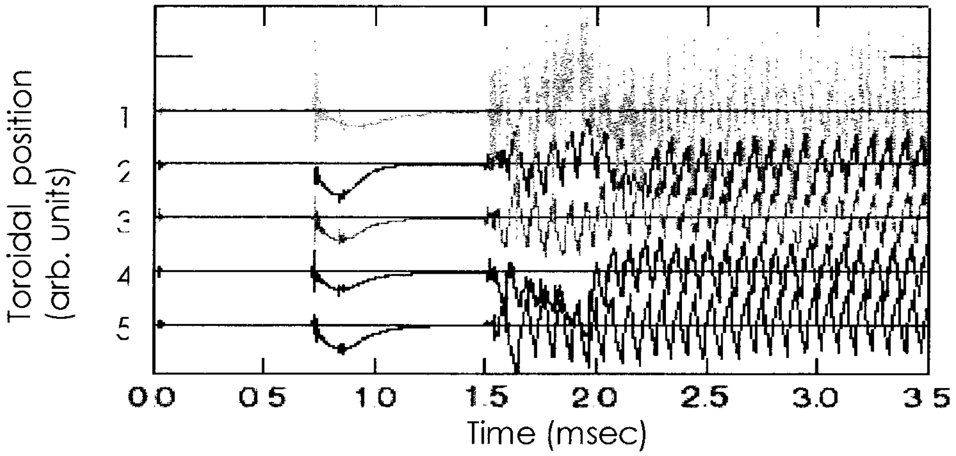

Figure 4.3-7: Control coil currents for vacuum shot with normalized gain G = 40

4.4 Latency

Latency is the time it takes for the feedback loop to process signals and generate a response to a perturbation. The latency of the mode control system is largely set by the analog to digital (AD) converters in the National Instruments modules, and to a lesser extent by the digital to analog (AD) converters and the processing speed of the FPGA chips. Latency is a crucial system parameter for any feedback control system because it sets the upper limit on the growth rates for the process to be controlled. If the controlling force cannot react in time to prevent significant development of the external kink mode, the arrangement will be unstable even for very high gain. Basically, the latency period must be comparable to or less than the growth time of the instability. For rotating modes, matters are complicated further, because a time delay introduces a phase shift proportional to frequency; for significant latency the slope of the phase transfer function can become steep enough to severely limit the bandwidth with stable phase margin, even with aggressive compensation filters.

The latency for the mode control feedback system was kept to a minimum of 10 μsec. This is adequate to track and control perturbations with frequencies up to 10 kHz and growth times much shorter than 1 msec. Because the typical conducting shells in experiments have wall times on the order of msec, the mode control system represents a high speed feedback system which should allow for stability of modes up to the ideal wall limit. An oscilloscope trace showing the system latency and loop rate period is shown in Figure 4.4-1.

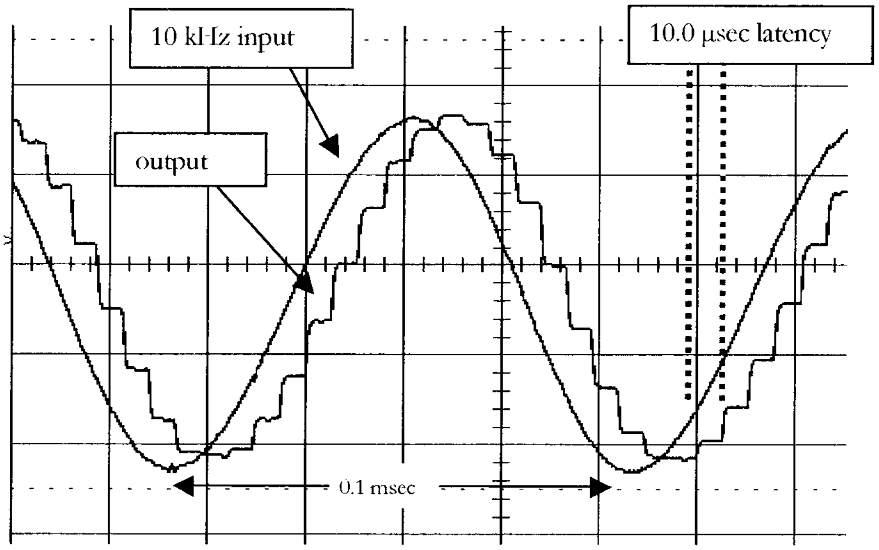

Figure 4.4-1: oscilloscope traces of input and output for NI 7831R FPGA modules

CHAPTER 5) EQUILIBRIUM AND KINK OBSERVATION

5.0 Basic Equilibrium and Feedback Effects

The type of discharge used throughout this dissertation is known as "current ramp" in the HBT-EP group. These discharges are characterized by a low initial ohmic heating pulse, which is ramped up aggressively in order to increase the plasma current rapidly and bring the safety factor at the edge to a value of $q \approx 3$ at around two msec into the shot. Because the current is induced in the plasma at the edge and is taken up by the hotter plasma core at the magnetic diffusion rate, such plasmas are characterized by a broad, relatively flat current profile. Such profiles tend to be kink unstable, while simultaneously being less susceptible to internal kink (a.k.a. tearing) modes, allowing for clear interpretation of the data and experimental results. The general methods of discharge programming have been described elsewhere in more detail[72,73]. The discharges used throughout the experiments in this dissertation will be described briefly below.

An initial breakdown is achieved with a an Ohmic transformer pulse, creating about 7 kA of plasma current. The transformer is then ramped via a larger and slower capacitor bank to provide a nominal 2 MA/sec current ramp starting at about $t = 1$ msec. A vertical magnetic field is programmed to keep the plasma positioned at fixed major radius during the discharge evolution. At $t \sim 2$ msec the edge safety factor q_a crosses 3. With the $q = 3$ surface now external, the $m/n = 3/1$ external kink mode is destabilized and begins to grow on a time scale of 100 μsec, as seen in Rogowski coils and an array of poloidal magnetic sensors mounted on the inside of one of the thick aluminum shell segments (called "shell mounted probes", SMP). The mode typically rotates toroidally at 4 kHz with the electron fluid. The diagnostics reveal an $m = 2$ internal tearing mode later on in the shot, leading to eventual disruption.

The edge q_a remains near 3 for more than 1 ms as the plasma moves slightly inboard and expands. Regardless of the feedback action (negative feedback, positive feedback, feedback off) the gross plasma behavior and basic plasma parameters were nearly identical in all shots used for this thesis, and only the kink mode growth and character appeared to be affected by feedback application as seen in Figure 5.0-1.

In the absence of any feedback, the kink mode growth rate appears to be approximately $(5 + i\, 2\, \pi\, 5) \times 10^{3}\ s^{-1}$, although the real part of the growth rates are nearly impossible to determine with any precision because the equilibrium is rapidly evolving. The measured kink growth rate is consistent with expectations near the ideal wall limit. The growth rate was observed to be independent of the position of the Al wall segments as expected for rotating ideal kink instabilities at or above the ideal wall limit. When the thick Aluminum wall segments were fully inserted, the characteristics of the kink instability did not change, but subsequently all the shots used in the data analysis had these shells withdrawn to five cm from the plasma surface. A variety of magnetic diagnostics identified the mode's helical 3/1 structure.

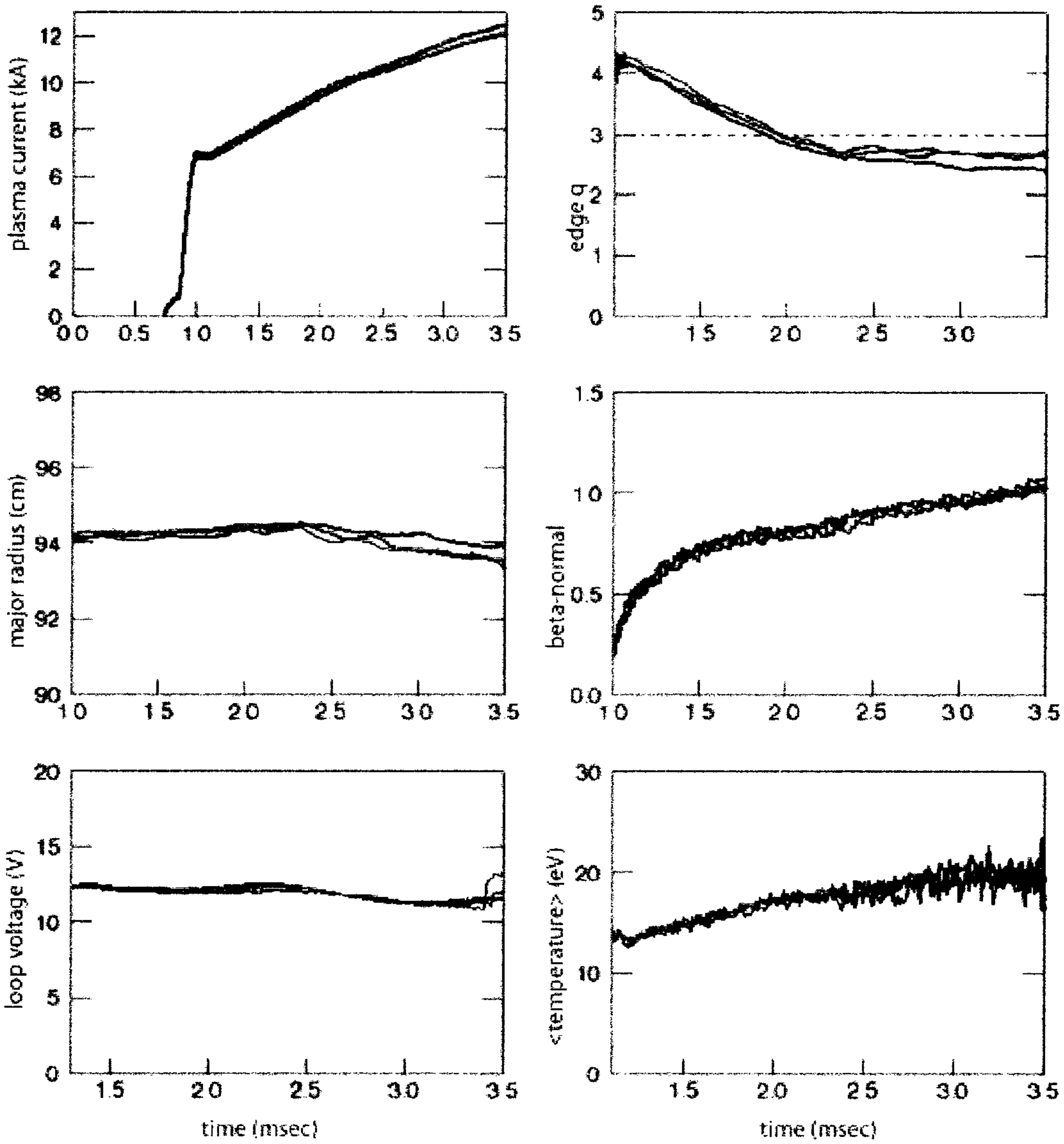

Figure 5.0-1: Basic plasma parameters: shot #43481 (black, no feedback), #43482 (red, positive feedback), #43494 (blue, negative feedback)

The major plasma parameters along with the surrounding vacuum vessel and magnetic field coil characteristics can be imported into a code such as TokaMac[74], an equilibrium solver that assumes simple pressure and current profiles. Although this does not incorporate the time history of the discharge (and therefore misses the flatness of the current profile for these types of shots), it does provide a general estimate of what the plasma equilibrium looks like.

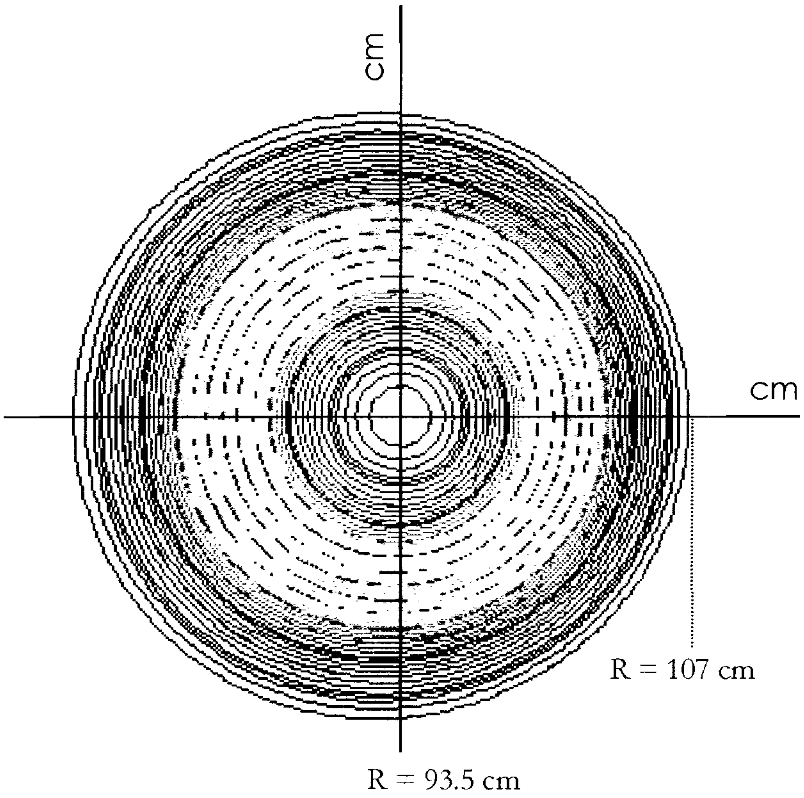

Figure 5.0-2: TokaMac output for shot #43268 (pressure profile and flux surfaces)

5.1 Stability of equilibrium

The equilibrium in turn can serve as input to a stability code like DCON which performs an MHD stability analysis on axisymmetric toroidal plasmas for both internal and external modes by calculating the change in energy (δW) arising from small amplitudes of each of these modes. Additional calculations with DCON can compute the δW 's for perturbations that have the same mode structures but negligible plasma current and pressure – thus calculating δW 's in a vacuum[75], so that the stability parameters ($s_{n,m}$) can be determined. These numbers represent a measure of the force driving a particular unstable mode, are a direct calculation of error field amplification by the plasma, and also can be used to calculate theoretical growth rates of the unstable modes found by DCON in the VALEN code.

Measurements of major and minor plasma radius, plasma current, toroidal and vertical fields, and as much information from other diagnostics were used to reconstruct an equilibrium file for shot #43268 (a typical discharge without feedback applied), which was then put through the DCON analysis. The results are described in this section.

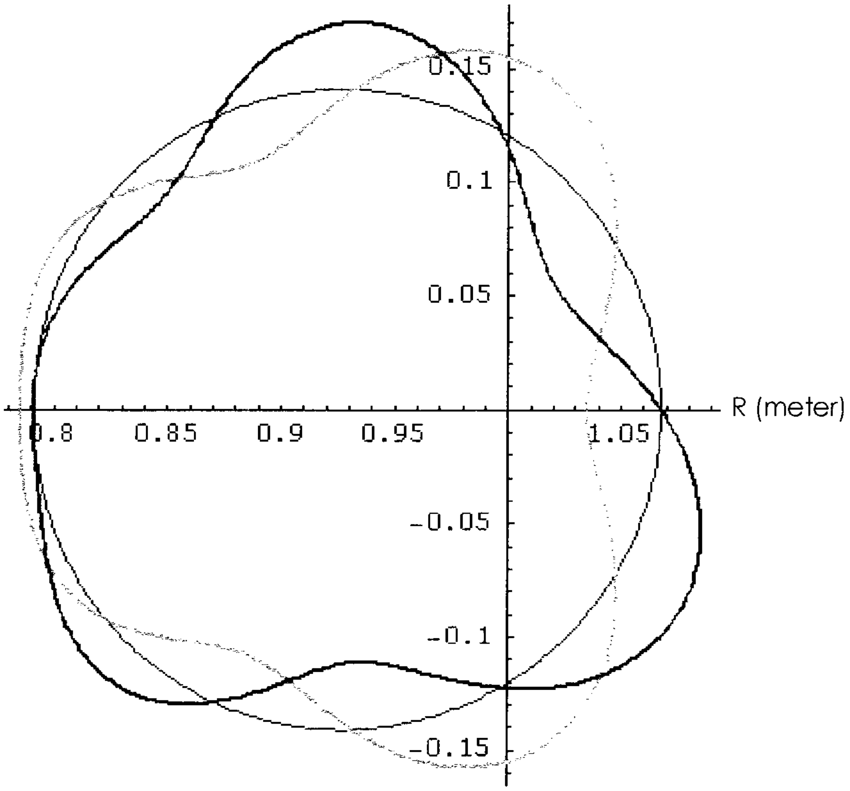

Figure 5.1-1: Radial magnetic field of $m/n = 3/1$ unstable mode in shot #43268 as computed by DCON

The plasma stability (s) values calculated for HBTEP shot # 43268 in the time interval {0.002-0.003} sec for a spectrum of plasma modes are listed in Table 2. Also listed are some important DCON input parameters that are used to obtain s-values for the spectrum of the 19 most unstable n = 1 plasma eigenmodes.

Energy of mode, δW	Inductance matrix, Λ	Dominant m number	s parameter
-6.88E-02	**-4.58E-06**	**3**	**0.14**
8.07E+00	**2.26E-04**	**4**	**-0.13**
4.92E+01	**2.23E-04**	**?**	**-0.22**
7.48E+01	**2.02E-04**	**?**	**-0.28**
1.03E+02	**1.87E-04**	**?**	**-0.43**
1.64E+02	**1.80E-04**	**?**	**-0.52**
2.30E+02	**1.75E-04**	**?**	**-0.55**
2.99E+02	**1.62E-04**	**?**	**-0.68**
4.80E+02	**1.51E-04**	**?**	**-0.89**
4.84E+02	**1.45E-04**	**?**	**-1.04**
5.45E+02	**1.42E-04**	**?**	**-1.20**
6.74E+02	**1.23E-04**	**?**	**-1.32**
7.86E+02	**1.00E-04**	**?**	**-1.40**
8.97E+02	**7.74E-05**	**?**	**-1.78**
1.03E+03	**5.47E-05**	**?**	**-4.15**
1.21E+03	**3.19E-05**	**?**	**-5.33**
1.34E+03	**2.77E-05**	**?**	**-10.49**
1.58E+03	**1.52E-05**	**?**	**-11.08**
3.28E+04	**5.19E-07**	**?**	**-607.27**

Table 2: DCON output: s parameters and δW's for least stable n = 1 eigenmodes

The 3/1 mode has a structure where magnetic field perturbations tend to be larger on the outboard side than on the inboard side. This is a toroidal effect and is quantified with DCON, as shown in Figure 5.1-2 where the radial fields in the two eigenvectors of the dominant unstable mode at time = 2.5 msec are plotted as a function of poloidal angle. The two eigenvectors are the sine and cosine-like components of the $m/n = 3/1$ mode, and their combined amplitude ($\sqrt{a^2 + b^2}$) are plotted in Figure 5.1-3.

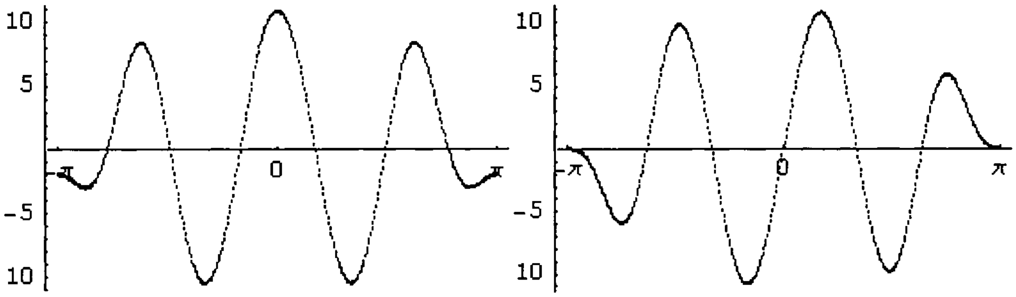

Figure 5.1-2: Cosine-like and Sine-like mode structure for 3-1 mode in shot#43268 as computed by DCON

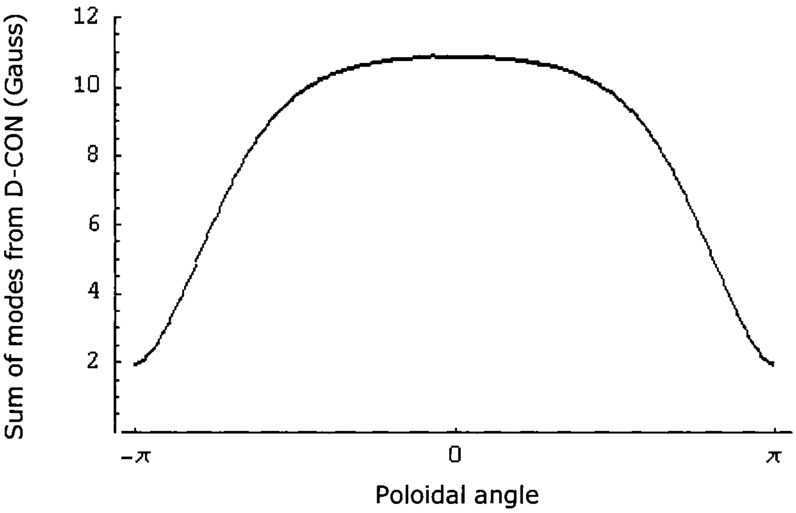

Figure 5.1-3 $m/n = 3/1$ mode amplitude vs. poloidal angle for shot #43268 as computed by DCON

VALEN is a finite element electromagnetic code which takes the output from DCON and calculates growth rates for unstable modes based on Allen Boozers formalism where the perturbed plasma mode is modeled as a perturbed plasma current on the unperturbed plasma surface in a particular geometry (conducting structures nearby are modeled as finite elements). Recently, VALEN has included the effects of rotation into its estimation of growth rates. For the discharges used in the experiments, the critical s-parameter at which kink modes will grow even if the walls are modeled as ideal conductors is s ~0.2. For s values less than this, kink modes are stabilized by rotation, as shown in Figure 5.1-4. Because kink modes are clearly observed, and they rotate at frequencies of _ > 3×10^4 s^{-1}, the plasmas are assumed to be ideally unstable, as depicted in the shaded region in the figure.

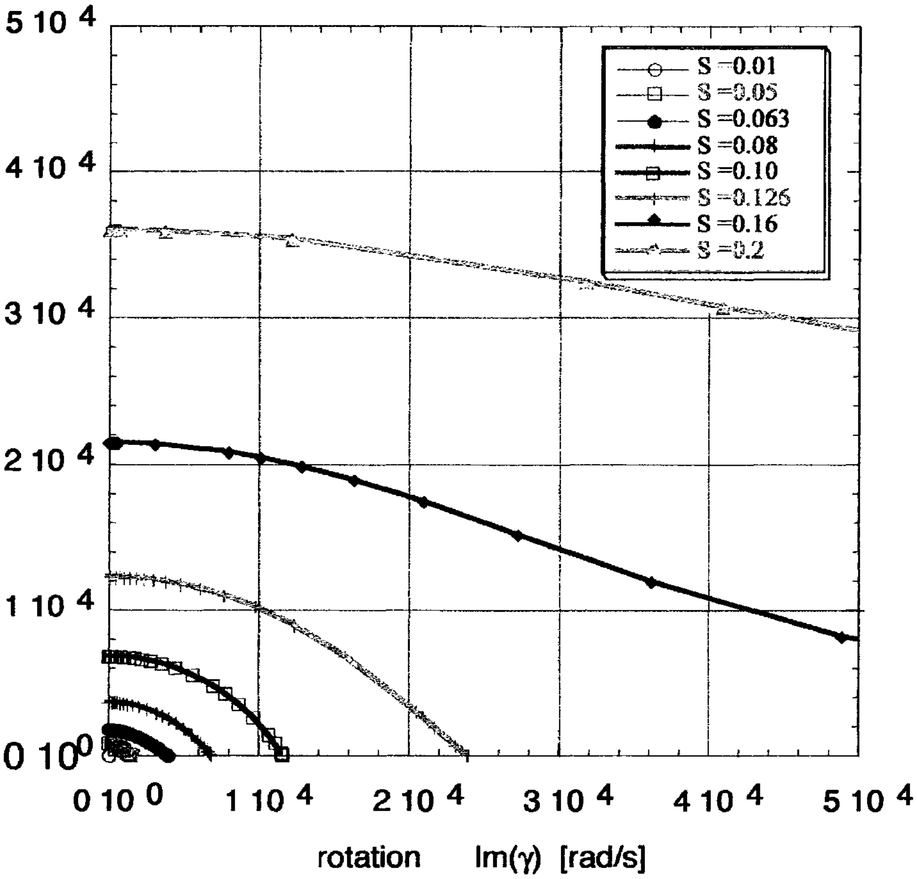

Figure 5.1-4: VALEN predictions for growth rates of external 3/1 kink modes for several s parameters as function of mode rotation

5.2 Kink Mode Identification

As soon as the rational surface m/n = 3/1 falls outside of the plasma, the 3/1 external kink can be seen to grow in the time interval $2 < t < 3$ msec. An m = 3 selecting Rogowski coil records several cycles of this rotating mode, which quickly saturates and is later followed by tearing mode activity and a disruption of the plasma column. An m = 2 selecting Rogowski coil is relatively quiet during this period, indicating that the mode is predominantly m = 3. The shell mounted poloidal field coil array (SMP) also records MHD activity and identifies the poloidal mode structure and shows the effects of feedback, although this diagnostic is not as clear as will be discussed later. The signal levels in the toroidally distributed poloidal sensors (which are used to drive the feedback coils) can also be used to characterize the fluctuations and quantify feedback effects.

The MHD activity is subject to a rotation which is of the same magnitude as the electron drift and in the same direction. A back of the envelope calculation for this drift is quickly done using an educated guess for the density and the known current and volume of the plasma:

$$n_e \sim 1'10^{13}\mathrm{cm}^{-3} \;,\; \mathrm{Volume} \approx \pi\, a^2 \cdot 2\pi R \approx \pi\,(15\,\mathrm{cm})^2 \cdot 2\pi \cdot 94\,\mathrm{cm} \;,\; I_p \sim 10\,\mathrm{kA}$$

These parameters give an estimate for the electron drift frequency near the outer flux surfaces of about 5 kHz, which is what the observed magnetic fluctuation rotation rates are.

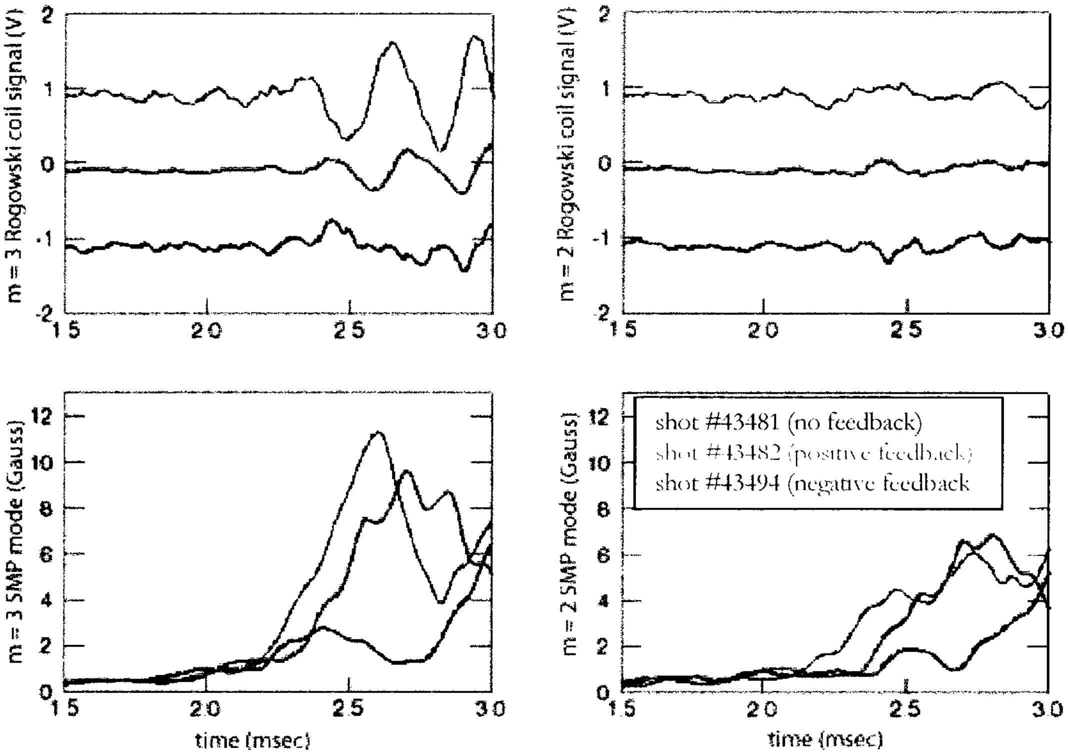

Figure 5.2-1: m = 3, m= 2 fluctuations in Rogowski coils and from modal decomposition in the SMPs

5.3 Poloidal Sensor Array Phase Analysis

The sensor array that provides the input signals to the feedback system can also serve as a useful diagnostic for MHD activity and even global plasma parameters. The integrated signals from these poloidal field coils yields the equilibrium poloidal magnetic field and therefore provides an additional measure of the total plasma current. The sensors are designed to measure fluctuations of course, and because they are distributed uniformly toroidally, and cover substantial poloidal sections, they give a good indication of the global MHD mode structure.

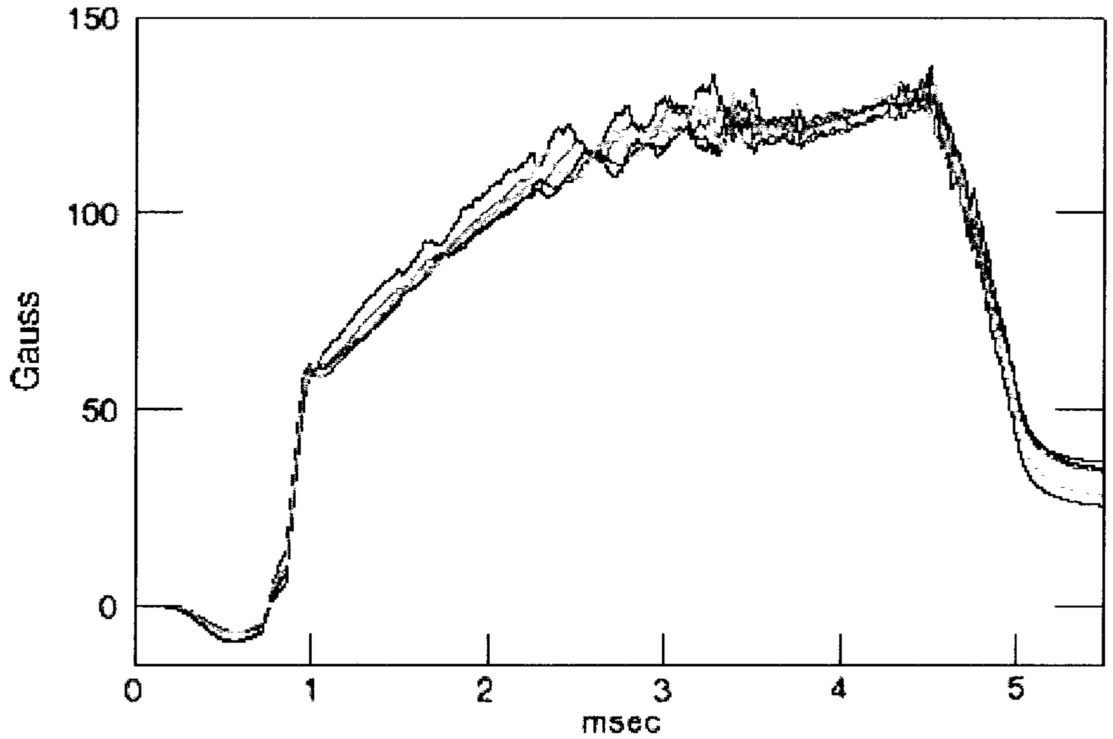

Figure 5.3-1: Integrated signals from top poloidal sensor group, shot #43075

As was discussed in section 4.3, toroidal geometry and plasma pressure effects distort the poloidal symmetry and cause perturbations to have a ballooning character on the outboard side of a tokamak. The analytical expression that approximately describes this distortion has already been introduced in section 4.3, namely $\theta^* = \theta - \lambda \sin\theta$. The modified poloidal angle incorporates purely toroidal effects (aspect ratio) as well as plasma pressure and current effects, and results in distortions away from cylindrical geometry, especially on the outboard side of the tokamak. The m = 3, 4 mode structures are illustrated in Figure 5.3-2, where the exaggerated lobes are drawn for a range of ballooning parameters, $0 < \lambda < 0.5$. On HBT-EP, the _ parameter had been previously assumed to be on the order of 0.4 for other discharges in previous experiments. However, every discharge has a peculiar λ parameter, which depends not only on the major radial position of the plasma, but also the current profile. The poloidal beta estimate is purely of an order of magnitude type. Therefore, it is not at all clear what the shape of a particular harmonic $m/n = 2,3,4\ldots$ looks like for a given plasma, and the shape function itself may evolve in time as plasma parameters change.

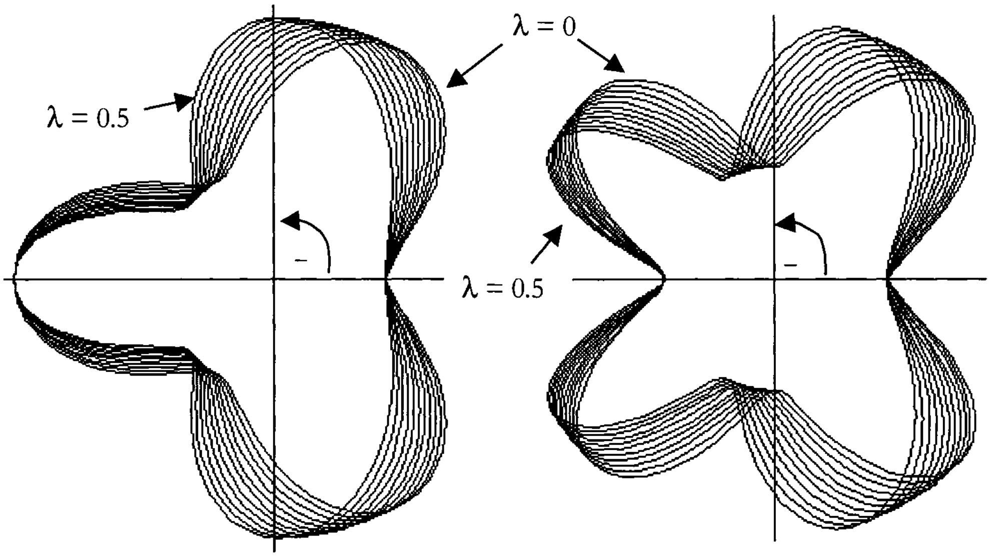

Figure 5.3-2: Exaggerated lobe structures with modified poloidal anlges for several λ values

The poloidal sensor array can yield information about the ballooning character of external kink modes and therefore perhaps some information about global plasma parameters such as the pressure and/or current profile. A novel analysis was performed in which the phase relationships of n = 1 perturbations between the individual poloidal groups provides a direct measure of the λ parameter. This analysis is fairly robust and uniquely incorporates noise suppression, and could be further refined and developed to be used as a general plasma diagnostic technique to determine plasma equilibrium information.

Relying upon a measurement of the phase relationship between the n = 1 modes that are identified in each poloidal group, the method requires only a knowledge of the position of the sensors and the major radius of the plasma column, and does not require a calibration of the sensitivity of the sensors. Because the signal amplitude in each sensor is a function not only of the local mode amplitude, but also the distance between the plasma surface and the sensor, the sensor sensitivity, as well as the rate of rotation of the mode, a brute force analysis of all the sensors to try to determine the shape of an MHD perturbation can be cumbersome or even impossible. However, if it is the case that only one poloidal mode is dominant in the plasma, the phases between oscillating signals in each of the sensors are determined uniquely.

The fact that the sensors are distributed uniformly in the toroidal direction makes the identification of the toroidal mode number trivially simple via a discrete Fourier transform, so we can look for MHD fluctuations with n = 1 only and discard other mode numbers. This also serves to reduce noise in the measurement. Each of the four poloidal sensor groups then provides a single number, the phase orientation of the n = 1 mode at a given poloidal angle.

The poloidal mode number is not identified as easily. Knowing the plasma position, and therefore the angle that each sensor group forms with the current centroid, one can calculate a characteristic spectrum that is produced when m = 2,3,4,...which depends very strongly on the plasma pressure and current profile (i.e., λ). To illustrate, the analysis is applied to shot # 43482. The plasma major radial position is determined to be 94 cm at t ~ 2.5 msec, and the expected phase differences between the n = 1 phase in the four poloidal groups are calculated for a range of values of the λ parameter. The result is shown in Figure 5.3-4.

Because the sensor groups are symmetric with respect to the vertical mid-plane ($\theta = 0$), two of the phase differences are redundant (the expected phase difference between groups 1 and 2 as well as 1 and 3 are expected to be identical to those between 3 and 4 as well as 2 and 4, see Figure 8.3-1), hence the overlapping yellow/black and pink/purple curves.

The recorded phase differences during the shot are shown in Figure 5.3-3. A clear mode does not emerge until t ~ 2.3 msec. A comparison with the expected spectra of phase differences indicates that the mode which appears after 2 msec is an m = 3 with a low λ parameter of about 0.3. Curiously, the spectrum also fits well with an m = 4 mode with λ parameter much larger, between $0.4 < \lambda < 0.5$. The actual plasma mode is not, of course, a pure m-numbered structure. In fact, the mode goes smoothly over from predominantly m = 3 to m = 4 when the m/n surface is inside or outside of the plasma edge. Because many other diagnostics tell us it is m = 3 (and because that is what one would expect if the edge safety factor is just below 3), we conclude that the mode is an unambiguous $m/n = 3/1$ external mode.

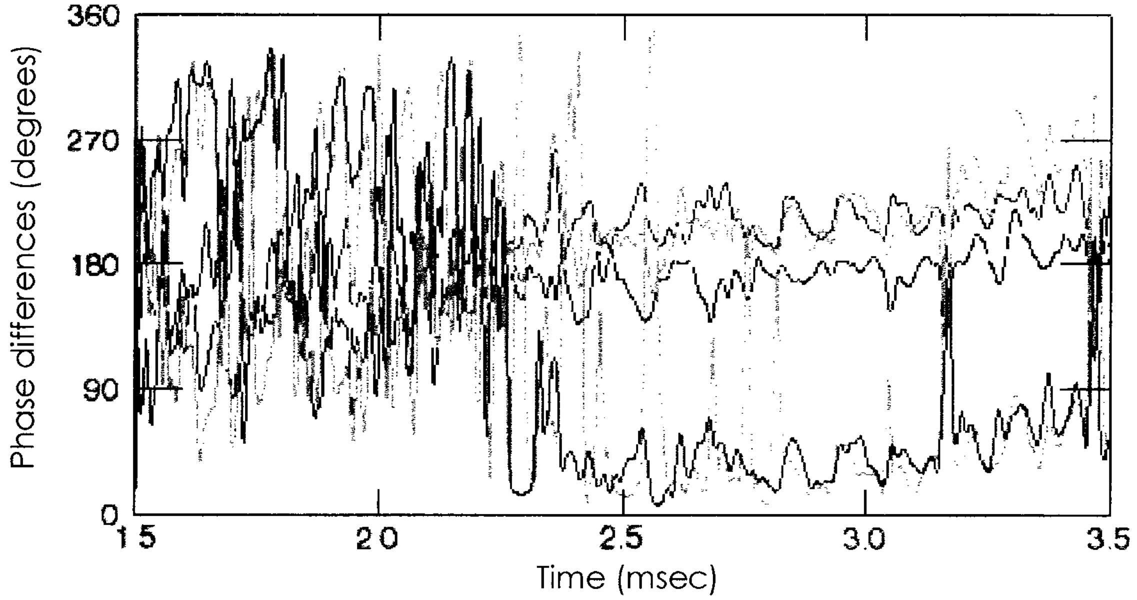

Figure 5.3-3: Phase differences between n = 1 phases in the four poloidal groups for shot #43482

Figure 5.3-5 shows the expected phase spectrum for the shot if one assumes a λ of 0.15. The spectrum evolves because the major radial position of the plasma is changing slightly, so that the angle formed between the magnetic axis and the sensors evolves during the shot.

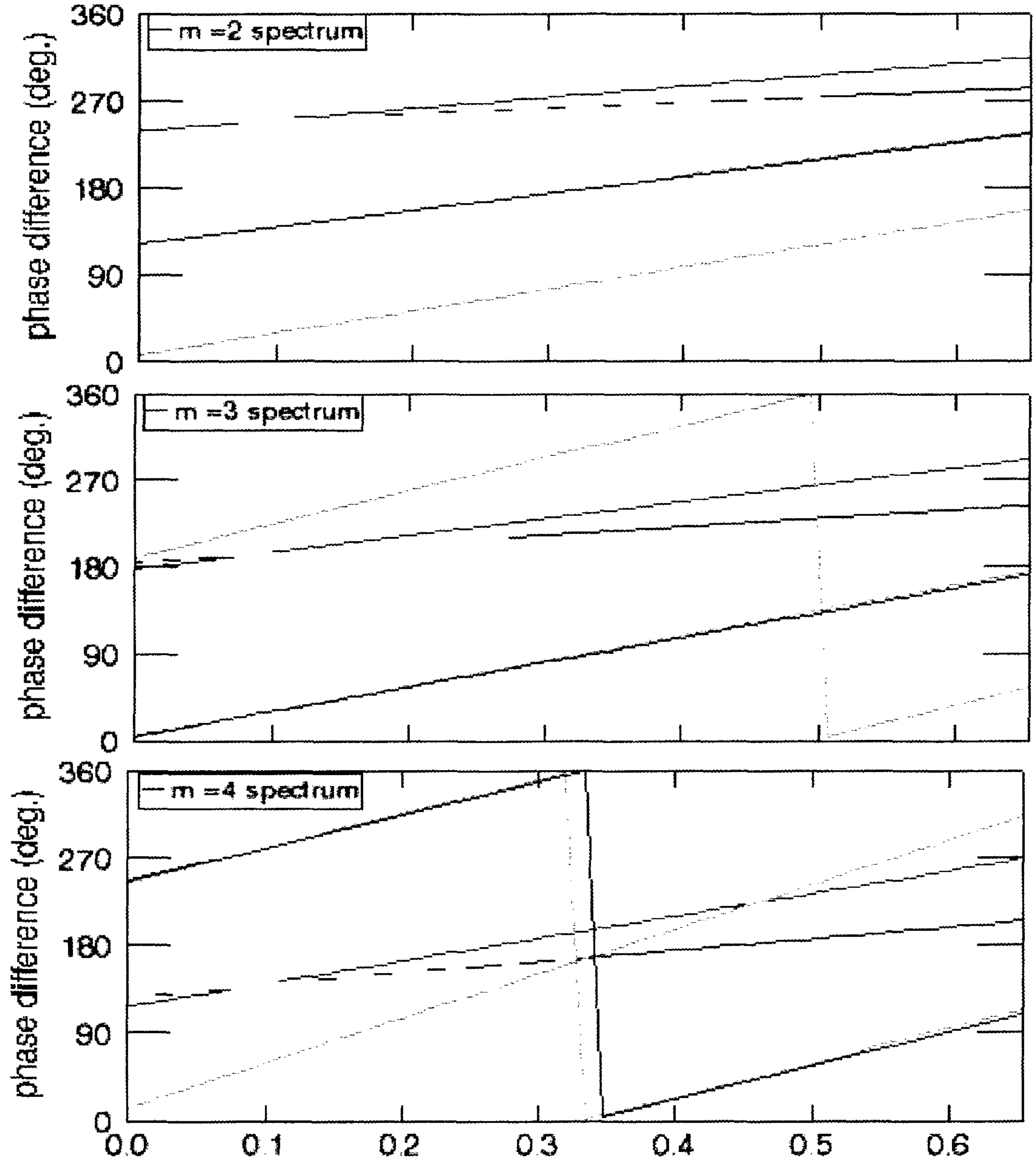

Figure 5.3-4: Expected n = 1 phase differences between the four poloidal groups based on known plasma and sensor positions

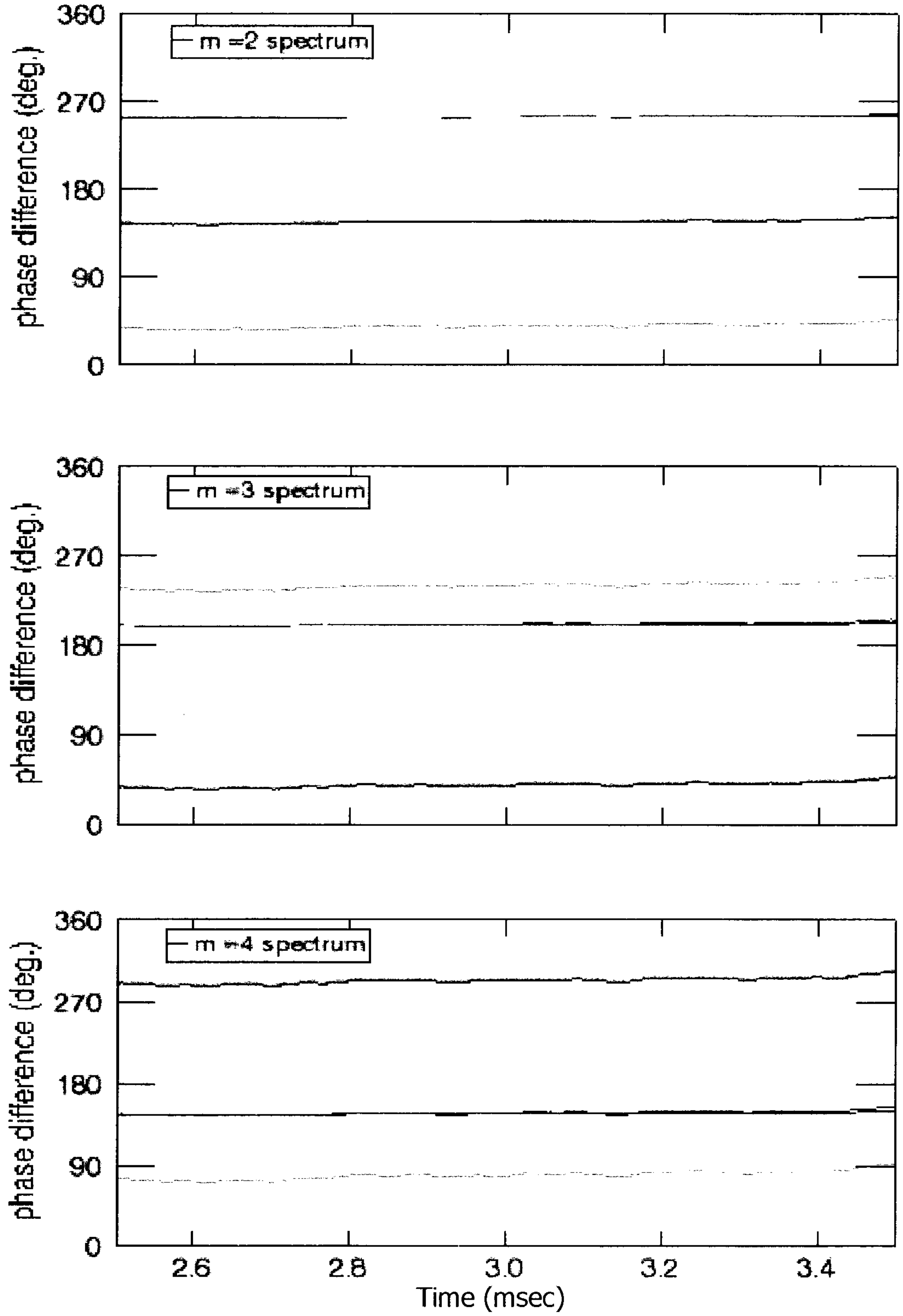

Figure 5.3-5: Expected phase difference spectrum for shot #43482, with λ =0.15

CHAPTER 6) OPEN LOOP EXPERIMENTS

6.0 Mode Direction

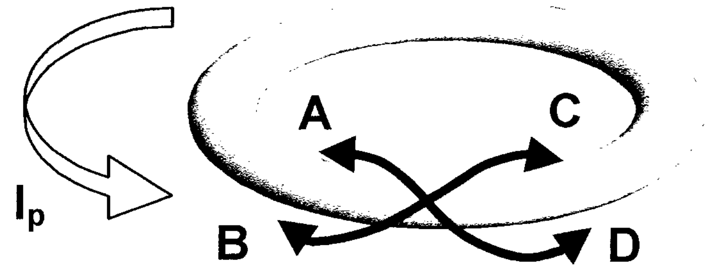

Figure 6.0-1: Four possible helical rotation directions in tokamaks. Mode rotation is in direction (A)

Initial feedback system experiments were conducted in an open loop configuration, i.e. the control coils were driven with pre-determined waveforms regardless of input signals from the poloidal sensors. The control coil array was programmed to produce m = 3, n = 1 helical perturbations by routing a sinusoidal waveform to drive each coil pair independently. The waveform to each was phased according to the following prescription:

$$I_{j,k} = I_0 \sin\left[\phi \pm \frac{j2\pi}{5} + 3\left(\theta \pm A_k\right)\right]$$

with A =[1.43, 0.471, -0.471, -1.43 radians] reflecting the poloidal position of the control coils. Frequencies between 3 and 8 kHz were tried. The direction anti-parallel to the magnetic field ("A" in Figure 6.0-1) was determined to be the direction of kink mode rotation since open loop feedback caused the largest response when phased in that direction. This is the direction of the electron fluid drift that results from the Ohmic heating current drive, and is expected from Hall MHD considerations: the kink mode perturbations along with the total magnetic field are frozen into the electron fluid. If a dissipation mechanism is considered, the mode can move slower or faster than the electron fluid but will experience a torque if it does.

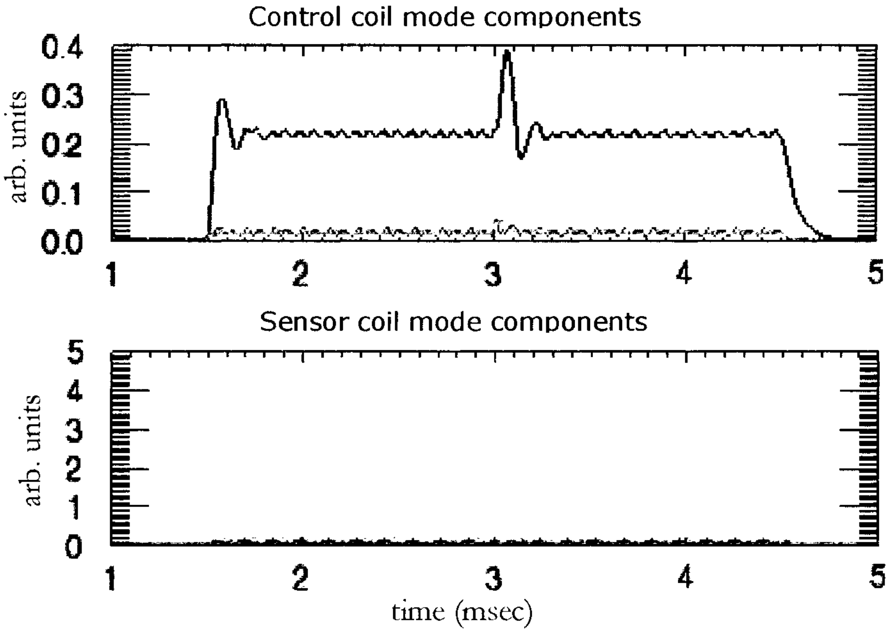

Figure 6.0-2: Open loop mode components (n = 0, 1, 2 = red, green, blue) in control coils and sensor coils (top poloidal array)

The vacuum coupling to the poloidal sensor coils proved to be negligibly small. Figure 6.0-2 shows the amplitude of the toroidal n =1 mode component in the bottom most (θ ~ -82°)

control coil and sensor coil groups. The control coils were driven with 5 Amperes of peak current at 4 kHz, representing near-maximum signal levels prior to distortion effects in the audio amplifiers. Built into the four synchronized FPGA generated waveforms was a phase flip of all signals at $t = 3$ msec, for possible spectroscopic studies along the lines of the experiments of M. Shilov[76], although this endeavor was abandoned in favor of closed loop feedback experiments. A cursory glance indicated that the plasma mode responds near instantaneously to the phase reversal, indicating that the kink modes are far from marginal stability, consistent with ideally unstable plasmas, at 3 msec into the typical discharge.

6.1 Mode Locking

An example of the determination of natural mode rotation, the relative phase between control coil toroidal $n = 1$ component of the coil currents and sensor coil voltages ($n = 1$ component) is shown for two different directions of the pre-programmed control waveform for the topmost poloidal group ($\theta \sim 82^\circ$) in the time interval $2 < t < 4$ msec, when the MHD activity suggests strong $m/n = 3/1$ kink mode presence. For shot # 43075 (Figure 6.1-1) phase locking clearly indicates that the direction of mode rotation is anti-parallel to the equilibrium magnetic field. The longest periods of phase locking occurred when the mode control coils were driven at frequencies of ~5 kHz, close to the natural mode rotation frequencies. The evolution of the phase relationship in Figure 6.1-1 suggests that the kink mode increases its rotation velocity with the increasing plasma current, while the frequency of the control coil waveform is fixed at 5 kHz.

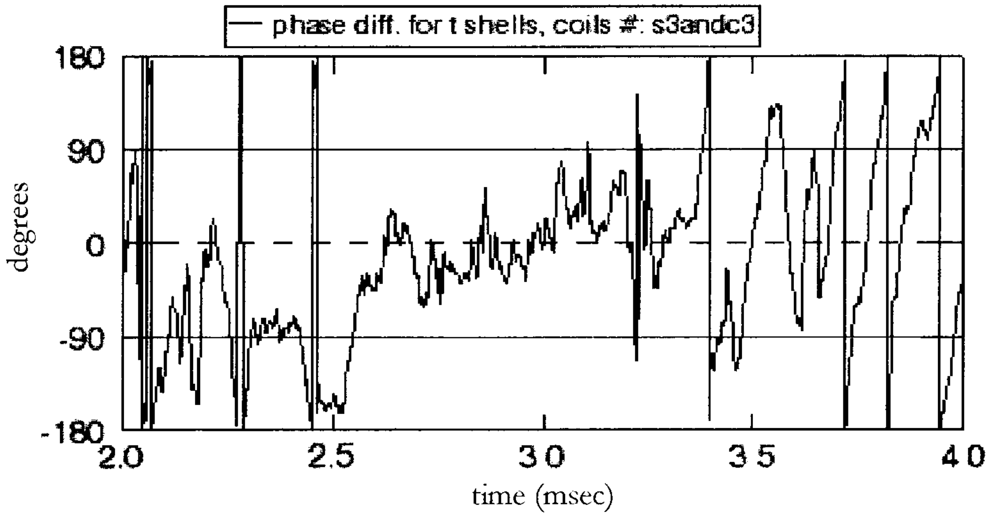

Figure 6.1-1: Phase locking between n = 1 components of control coil currents (5 kHz) and sensor coil voltages for shot #43075, waveform anti-parallel to magnetic field direction ("A" in Figure 6.0-1)

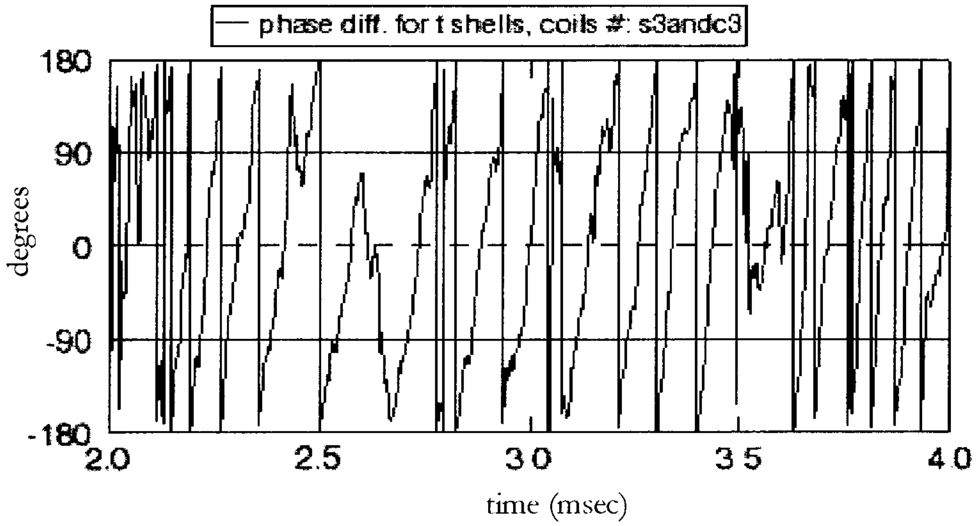

Figure 6.1-2: Phase relationship between n = 1 components in control coil currents (5 kHz) and sensor coil voltages for shot #43080, waveform parallel to magnetic field direction ("D" in Figure 6.0-1)

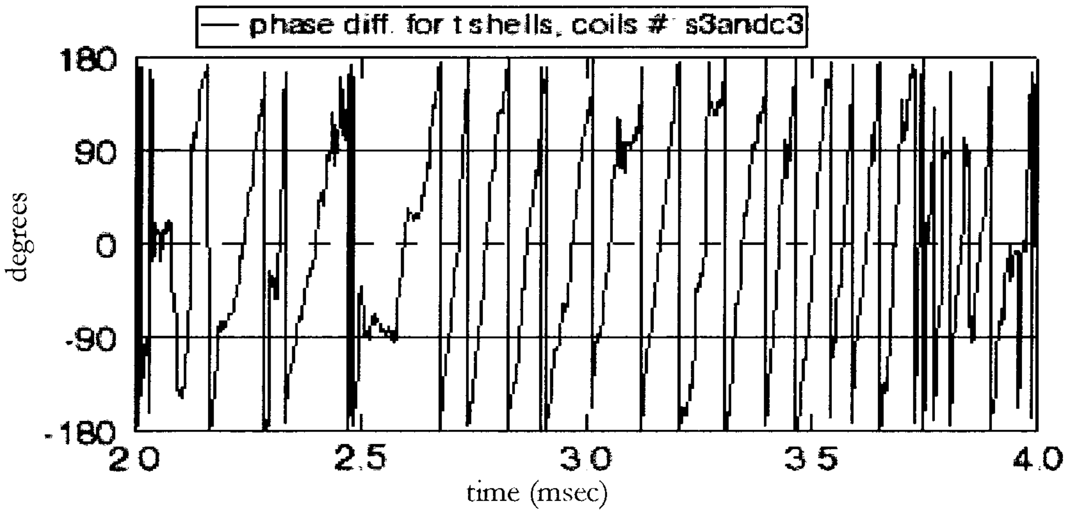

Figure 6.1-3: Phase relationship between n = 1 components in control coil currents (4 kHz) and sensor coil voltages for shot #43091, waveform in direction "B" in Figure 6.0-1

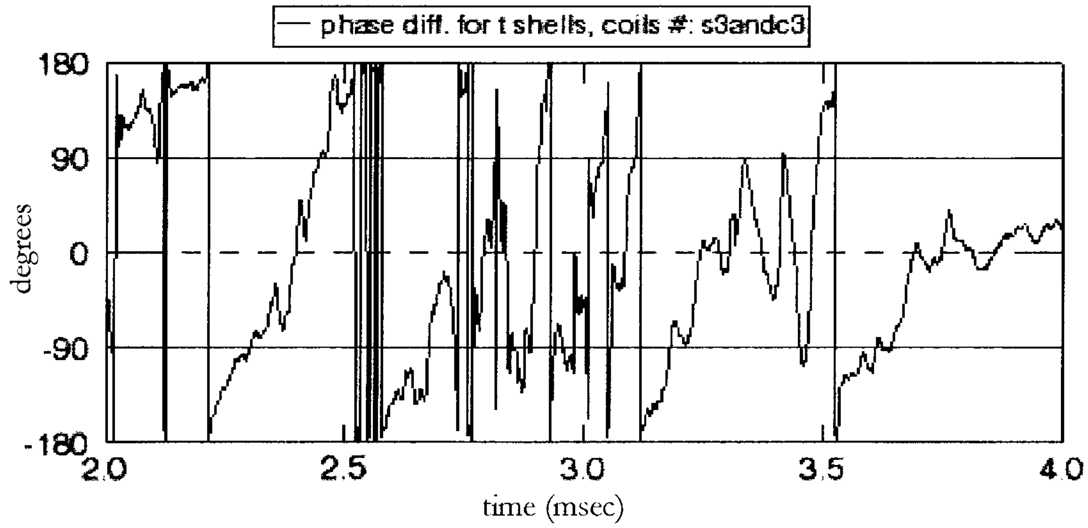

Figure 6.1-4: Phase relationship between n = 1 components in control coil currents (5 kHz) and sensor coil voltages for shot #43037, waveform in direction "C" in Figure 6.0-1

6.2 Resonant Error Field Amplification

When the plasma is near marginal stability, $|s| < 1$, the energy required to drive a helical perturbation on the surface of the plasma is less than the energy that would be required in a vacuum. Hence the plasma acts to amplify externally imposed fields which are resonant with the mode in question[77]. This effect can easily be seen on the m = 3 selecting Rogowski coil signal when comparing plasma and vacuum shots that have identical control coil waveforms.

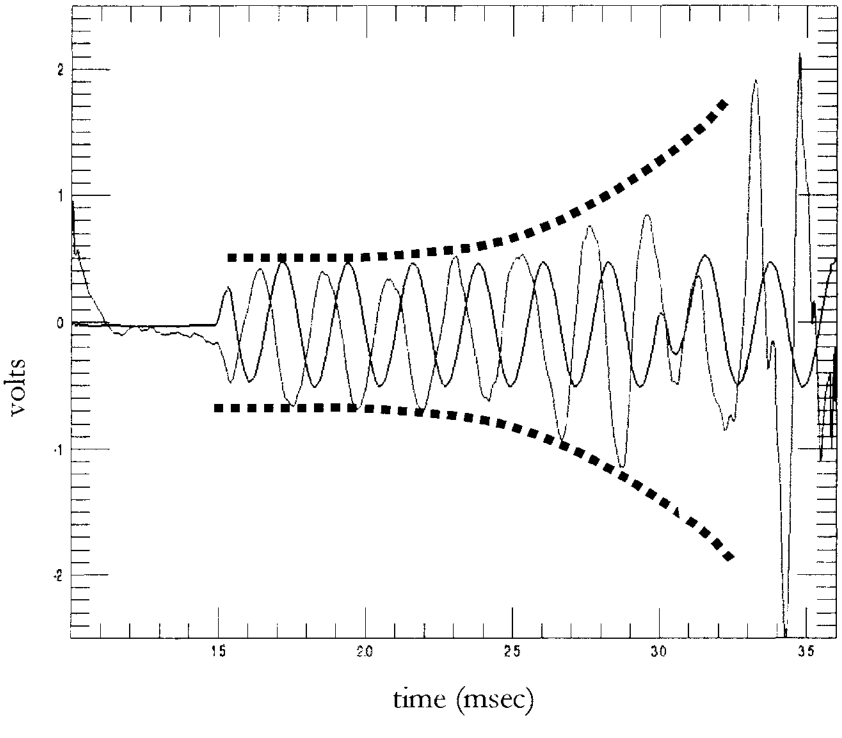

Figure 6.2-1: m = 3 Rogowski coil signals in vacuum (black), with plasma (red, shot #43075)

Assuming the voltage in the Rogowski coils is directly proportional to the amplitude of the perturbed magnetic fields (and it is, at fixed frequency), the degree to which the fields are amplified in the presence of a plasma allows in principle for some determination of the stability parameter, s, for the m/n = 3/1 external kink mode. In actuality, the 1/s amplification is not seen in strongly damped plasmas as discussed by M. Shilov[76]. The amplification factor was found to be relatively small in all cases, with a maximum amplification of about 2. A detailed study of the amplification factor was not performed as this has been done elsewhere[76], while the focus of this dissertation is closed loop feedback.

CHAPTER 7) LATENCY EXPERIMENTS

7.0 Theoretical Considerations

Latency in feedback systems is an important parameter which affects the ability of the feedback system to respond to perturbations with large growth rates. Obviously, if an instability grows substantially faster than the time it takes for the controlling force to react, the instability cannot be suppressed. When external kink modes are locked to the chamber walls (with no or little rotation, as in the DIII-D experiment), this is a simple minded concern. For kink modes on HBT, system latency plays an additional and crucial role in determining feedback effectiveness. As the modes rotate around the tokamak, the proper phasing between control coil signals and sensor coil signals must be carefully preserved, because the mode will have rotated by the time feedback fields are imposed the plasma. If the frequency dependent transfer functions of the system are not engineered to provide the proper phase response over a broad band of frequencies, the mode will experience positive feedback and be excited at some frequencies, resulting in amplitudes potentially larger than what would occur without feedback at all.

Incorporating latency into transfer function calculations results in a pure phase shift with unity gain. A fixed latency period effects a phase shift proportional to frequency, because at higher frequencies the latency period represents a larger fraction of the signal period. While there are means to reduce the frequency dependence of the phase transfer, this can only be accomplished up to a point (where the latency period is still small compared to the signal period). At high frequencies the transfer function phase shifts are radically steep and will cause the response field to be applied improperly for some band of frequencies. Figure 7.0-1 shows what is expected for several different latency periods in the feedback system on HBT-EP. The calculations include reactances from analog circuitry and coils, as well as digital phase lag/lead compensation. Assuming that a 0° phase shift implements optimal negative feedback, the feedback system will drive instability at frequencies where the phase shift is greater than $\pi/2$, as indicated by the red regions in the figure. For large latency periods, there are several bands of frequencies where this is the case. Only when the latency is kept as low as 10 μsec can the phase shift in the transfer function be kept near zero throughout the frequency band 1-10 kHz.

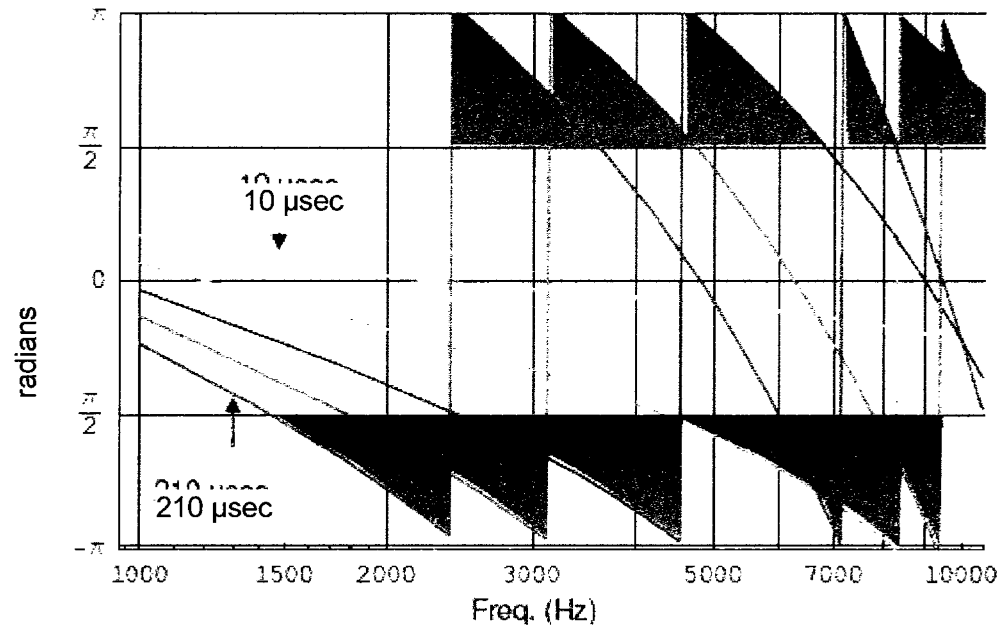

Figure 7.0-1: Calculated phase response of feedback with latency of 10, 60, 110, 160, and 200 μsec

Consequently, it is expected that when the feedback system is subject to substantial latency, and while performing negative feedback at the natural mode rotation frequency, it will end up exciting kink modes at other rotation frequencies. This was indeed observed.

7.1 Experimental Results

The FPGA algorithm was modified to include a programmable latency without affecting the loop and sample rate. This was done by writing the output data of the calculations to a FIFO buffer, and then reading the buffer in sequence for analog conversion. Latency ranges from 10 to 210 microseconds where used, and feedback effectiveness on m/n = 3/1 external modes measured. The data agrees with expectations from chapter 7.0 for such scenarios: when latency is added into the filtering algorithm without regard for transfer function phase shifts, negative feedback cannot be achieved except for at the lowest of frequencies, and positive feedback is seen as the phase shift due to latency becomes destructive.

In previous experiments, it was found that the optimum spatial phase angle between control coil and sensor coil n = 1 modes for negative feedback is approximately -90° at a particular setting for the spatial rotation matrix in the FPGA software. This setting was fixed for all the shots in the experiments, so that for 10 μsec latencies (the built-in minimum) the system provided negative feedback which resulted in mode suppression. For other latency settings, the spatial phase relation between control and sensor coils was therefore obviously changed, resulting in effects very different from negative feedback. For example, in Figure 7.1-1 are the time traces of m = 3 Rogowski coil signals for a no-feedback case and a feedback shot where a 60 μsec latency was added to the loop. Clearly, high frequency excitation occurs despite the fact that the feedback system was configured to suppress the mode.

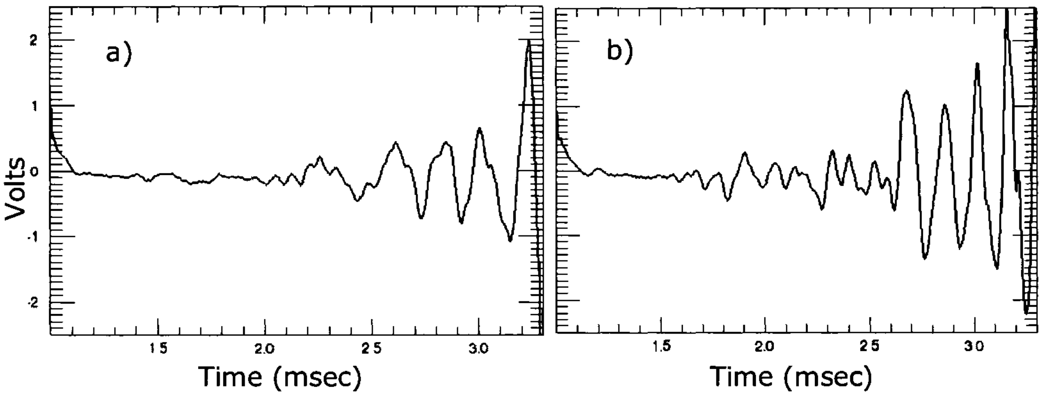

Figure 7.1-1: a) m = 3 Rogowski signal from shot #43312 (no feedback) and b) m=3 from shot #43305, negative feedback, but with 60 _sec latency

The kink mode amplitude and frequency were quantified using one of the m = 3 Rogowski coils. The coil voltage in the time interval 2 < t < 3 msec was Fourier transformed to yield a histogram of frequency components up to 20 kHz. The peaks in the spectra for different latency periods in the feedback system match the expected peaks from Figure 7.0-1 very well. The results for a number of these shots along with the expected peaks are shown in Figure 7.1-2. Clearly, only the smallest latency feedback scenario (10 μsec latency) resulted in suppression of the mode, all larger latency experiments caused amplification of the perturbations at some frequencies in the region of interest.

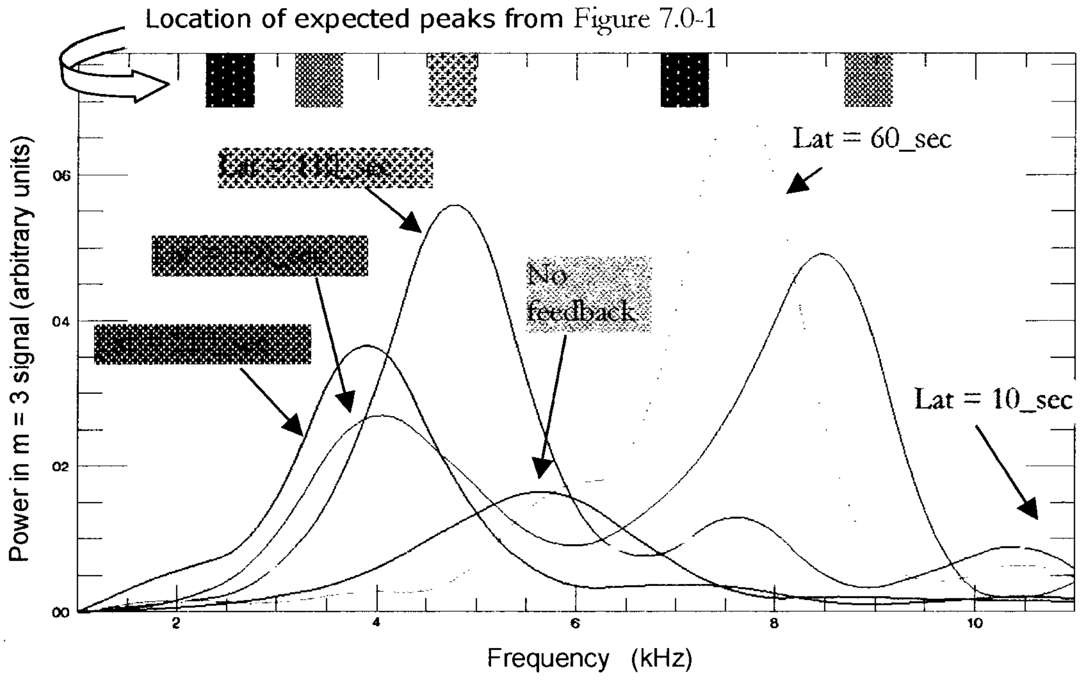

Figure 7.1-2: Smoothed histograms of m = 3 Rogowski signal amplitudes for various latency settings

CHAPTER 8) TOROIDAL PHASE ANGLE SCANS

Mode control feedback experiments were attempted in which the $n = 1$ toroidal phase difference between the sensor and control coil arrays was changed incrementally through 2π radians. Any $n = 1$ MHD external kink mode will have the toroidal position of maximum perturbed radial field and maximum perturbed poloidal field ninety degrees out of phase at fixed poloidal angle, and therefore the feedback system is expected to perform optimally when the applied radial control flux is a quarter toroidal wavelength rotated with respect to the poloidal mode flux identified by the sensors.

8.0 Transfer Function Variation

As described in section 3.4, the mode control feedback system has a rotation operator built into the digital algorithm. It is this operator which was adjusted to set the toroidal phase of the $n = 1$ output signals with respect to the $n = 1$ mode derived from the sensors. The operator was varied over the full circle in 5° increments from shot to shot and hundreds of shots were taken. The general nature of the discharge was very reproducible. The discharges were also very robust, only the signature of the external modes changed as a result of feedback.

To investigate the relationship between the transfer function of the feedback coils and the performance of overall feedback, I performed two sets of separate experiments: one with the phase shift transfer function varying considerably in the frequency band from 1-20 kHz, and a subsequent set of experiments in which the phase shift was relatively flat and constant over that range of frequencies. The different behaviors were the result of only small parameter changes in the coefficients of the digital filter, while all hardware components and gain settings remained the same. The two transfer functions for the configurations (hence forth referred to as the filter [A] and filter [B]) are shown in figure 17. Because the MHD modes observed in the tokamak rotate toroidally, a temporal phase shift in the feedback signals is equivalent to a toroidal spatial phase shift, and because the effectiveness of the feedback is critically dependent on the toroidal phase of the applied radial control fields, the use of digital filter [A] resulted in an inability of the control system to suppress perturbations at all frequencies.

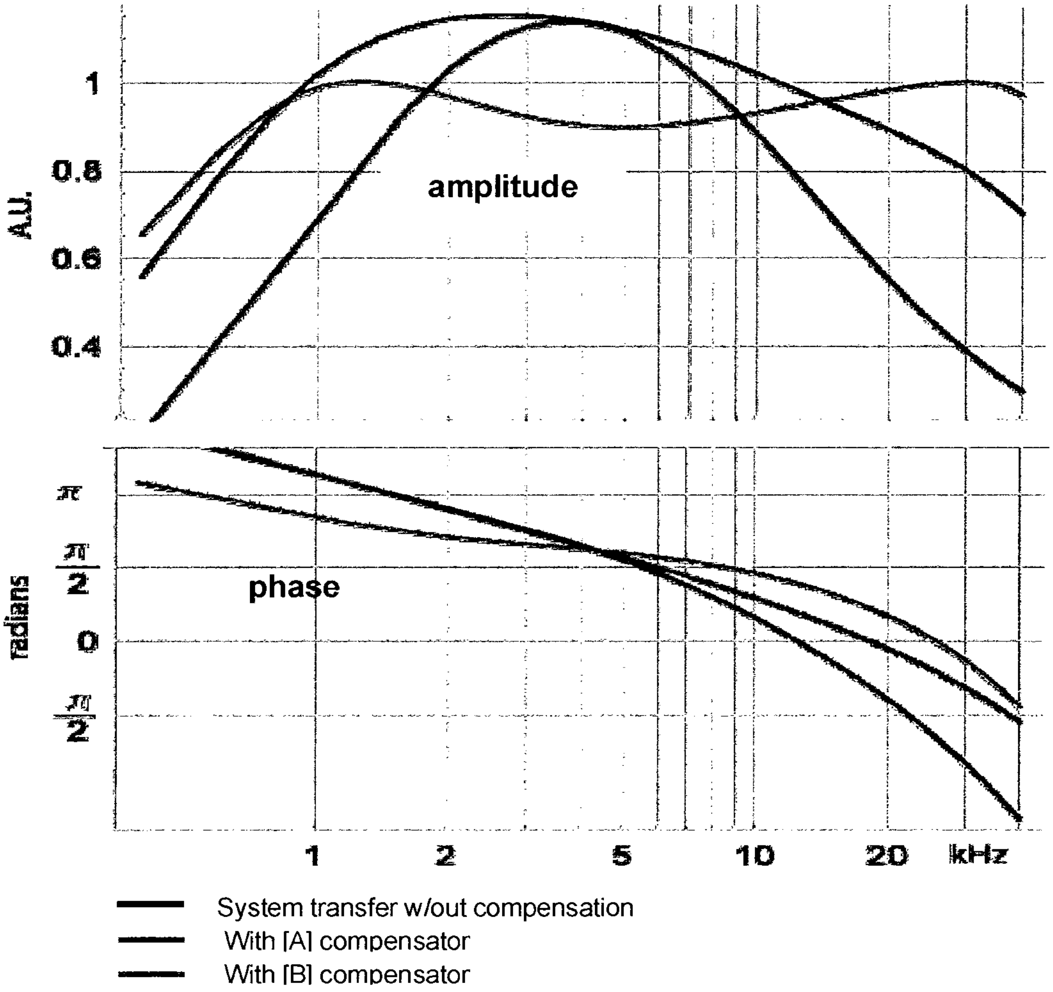

Figure 8.0-1: Total system transfer functions for the toroidal phase angle scan experiments

The real and imaginary parts of the transfer functions used in the experiments are shown in Bode plots in Figure 8.0-1. The black curves in the figure represent the transfer functions intrinsic to the hardware, without any digital filtering. The red and blue curves represent the effect of filter [A] and [B] respectively.

The rotation operator was incrementally adjusted, and the target phase angles used in the experiments are shown in Figure 8.0-2. In the figure, the different target phase angles are color coded for later identification, so the actual phase angle measured between the mode at the sensors and the mode produced by the control coils can be displayed with the target phase angle in mind in the results and analysis section of this chapter. The plot also introduces a type of polar plot in which the radial distance from the center indicates a frequency, used frequently throughout this chapter. For each data set, 72 different toroidal target phases were tried to provide a detailed map of feedback performance as a function of toroidal phase shift in the control coils.

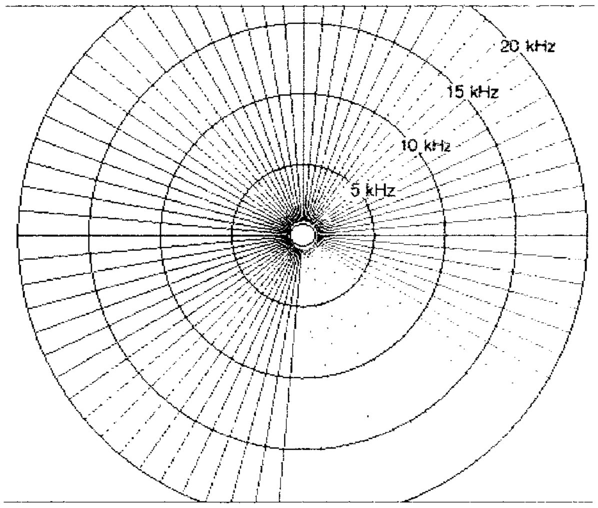

Figure 8.0-2: Target phase angles for feedback experiments using digital filters [A] and [B]

Because of the frequency dependent phase shift in the transfer functions of the control loop (even for the filter [B]), the toroidal phase angle between control field and sensor field depends on the frequency in question, and so for some fixed rotation operator setting, the result is that different frequencies are mapped into different toroidal phase relationships. Knowing the transfer functions, these maps can be drawn in the polar plot format for illustrative purposes and are shown in Figure 8.0-3. The result shows a spiral: if the spiraling is too severe, some frequencies will unavoidably experience positive feedback for any given phase angle setting as they are rotated by more than $\pi/2$ toroidally.

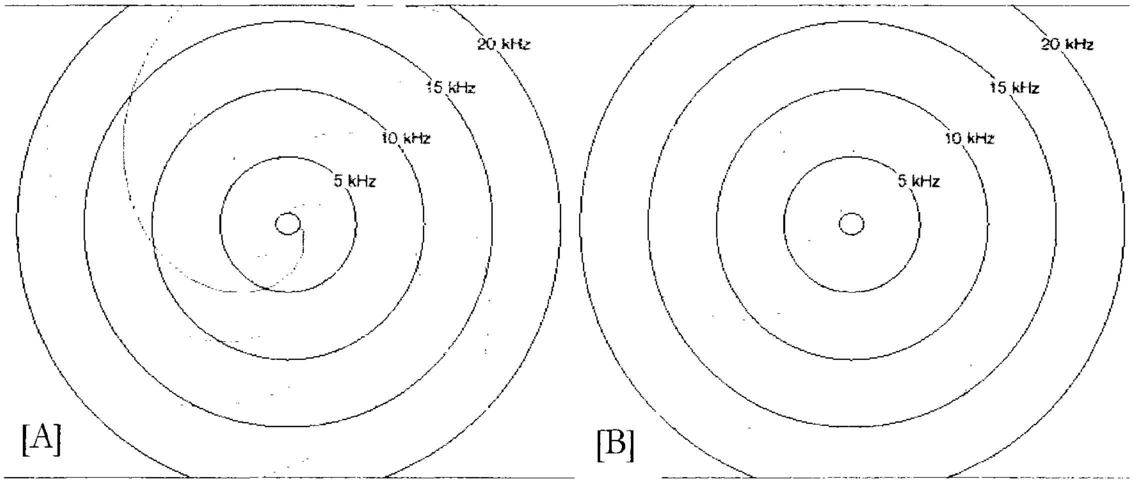

Figure 8.0-3: Transfer function toroidal phase mapping for system with filter [A] and [B]

8.1 Phase Stability and Tracking

When the control coils are not powered by the audio amplifiers (feedback inactive), they pick up magnetic fields and yield signals proportional to the rate of change of the radial magnetic field at their location. An analysis of the phase of the n = 1 component of these signals is then straightforward. The spatial phase relationship between control coil currents and sensor coil currents appears to be close to -90° (defined as clockwise when viewing the tokamak from above and shown in fig. 20), which is the phase expected to be optimum for suppression with feedback. * This may be understood by considering that the passive control coils produce a current to oppose the perturbed mode-flux (Lenz' Law). This current is in the same direction as that required to feed back suppressively upon the modes. An example of this is shown in Figure 8.1-1, where it is apparent that the phase relationship between n = 1 components of sensor voltages and control coil currents is ~ -90° after the mode is clearly established, around t = 2.5 msec.

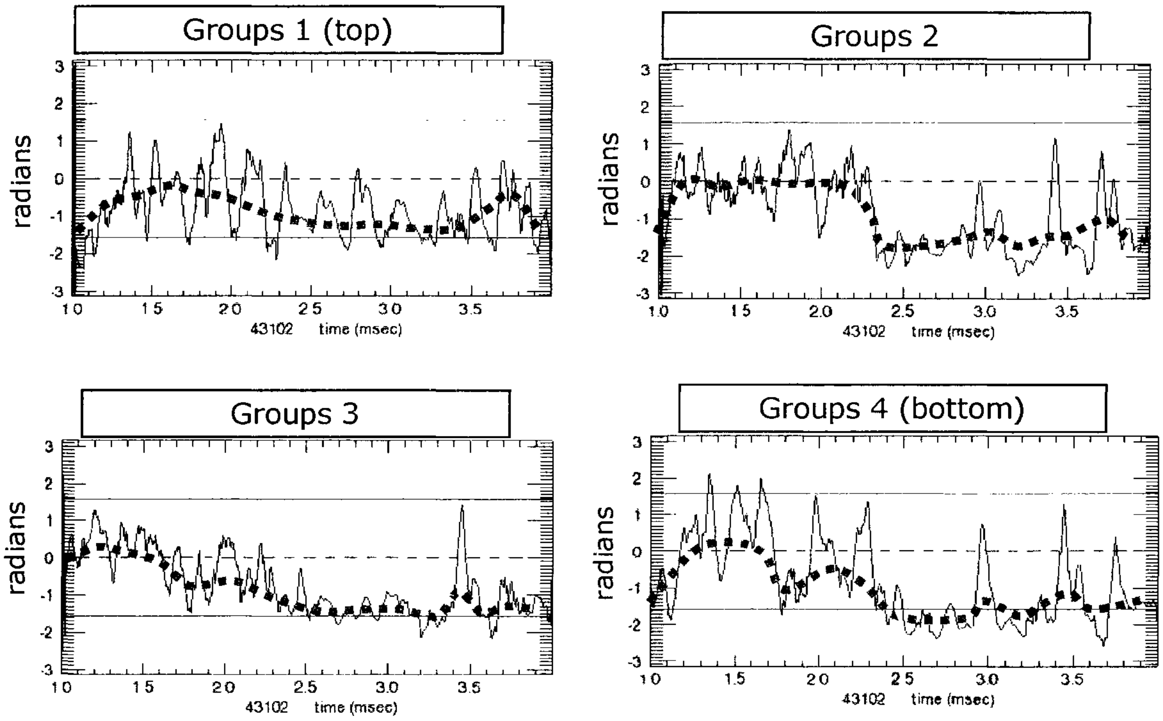

Figure 8.1-1: Spatial phase relationship between n = 1 components for the 4 control/sensor groups

---

[*] The c-coil and s-coil n = 1 currents are not exactly 90° apart because the resistance in the c-coil introduces a frequency dependant phase shift for lower frequencies (L/R ~ kHz), but determining the exact instantaneous frequency of signals is not possible.

With closed loop feedback, the measurements of the relative phase of the sensor and control currents reveal that when the frequency dependence of the phase shifts in the transfer function is reduced, the relative phase is well defined and tracks the target phase set in the algorithm very well. Then converse is true for the experiments using digital filter [A]. In Figure 8.1-2-B, the trouble at +/- 90° arises because for negative feedback, the mode suppression works very well and the phases are difficult to pick out (small amplitudes), while for positive feedback signal saturation also causes an ambiguity in the phases.

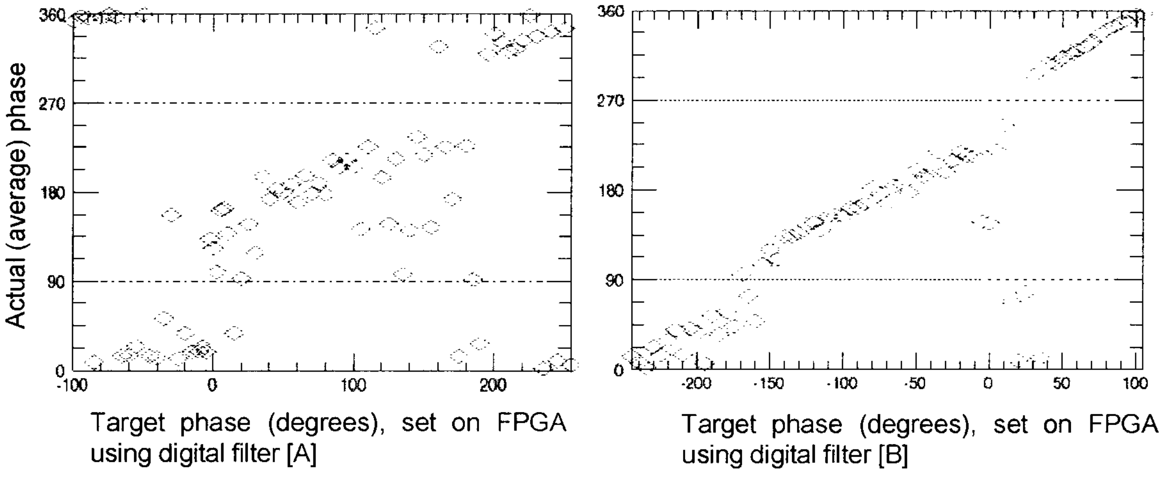

Figure 8.1-2: measured phase between n = 1 modes in control and sensor coil arrays (averaged over the four poloidal groups), for 2 < t < 3 msec vs. target phase set by rotation operator

Figure 8.1-3 shows the same data plotted in polar plot form for comparison with the target phase angles in Figure 8.0-2, which more clearly illustrates the differences between the effects of the two different phase lag/lead compensations.

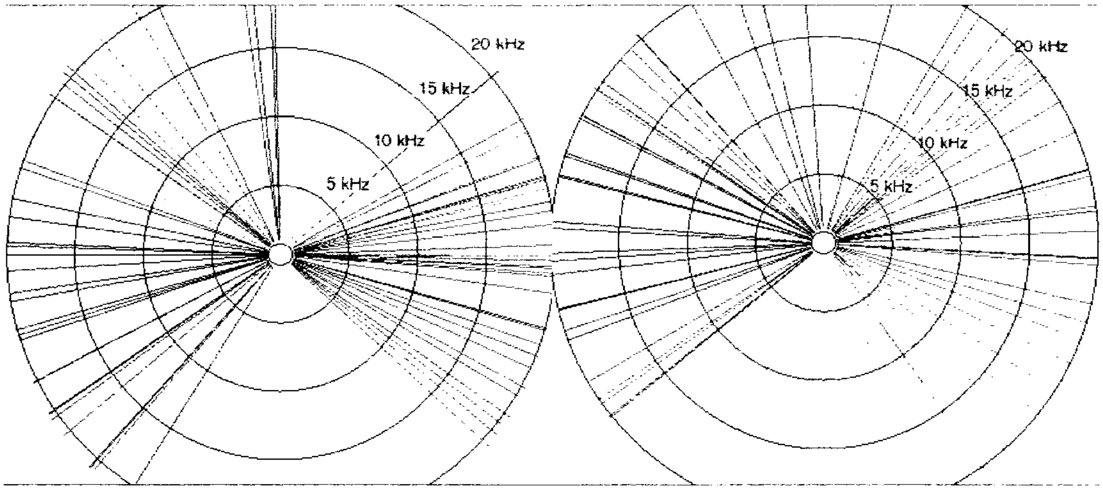

Figure 8.1-3: Measured (average) phases between n = 1 components of control and sensor signals, color coded to indicate target phase

The effectiveness of feedback was then quantified using several magnetic diagnostics on HBT-EP. As mentioned previously, there are two m =3 selecting Rogowski coils, a poloidal array of current loops at one toroidal position mounted on the inside of thick aluminum shells that surround the plasma (SMP's), and of course the feedback sensors themselves can be used to measure mode amplitudes.

8.2 Rogowski Coil Analysis

The m = 3 selecting Rogowski coils proved to be the most dramatic method for characterizing the feedback system performance. Rogowski coils are coils whose winding density is proportional to the amplitude of a particular Fourier component of poloidal fluctuations at the toroidal location where the coil is placed. In the absence of toroidal effects (in cylindrical geometry), a Rogowski coil in theory is a perfect Fourier selector and is immune to perturbations not explicitly resonant with the winding density. There are two m = 3 selecting Rogowski coils on HBT-EP, they each produced similar results. However, since one of these coils is slightly more prone to noise contamination, the following analysis deals with only the other.

The simplest analysis to do is to measure the fluctuation level of the raw Rogowski coil signal during the time window when the external kink is detected. It becomes then immediately obvious that the toroidal phase relationship of the control field relative to the poloidal perturbations at the sensors determines the action of the feedback system as seen in Figure 8.2-1. The relationship is smoothly varying in the sense that the effect on the Rogowski coil signals is proportional to the phase difference between optimum phase angle and actual phase angle, without exhibiting phase instabilities such as have been observed in tearing mode feedback studies[78]. Also clearly evident is that the digital filter with the flatter frequency response performs much better than the system in which phase shifts vary as a function of frequency. The raw Rogowski signals are a measure of the time rate of change of the magnetic fluctuations and tend to emphasize high frequencies. Integrating the signals yields information about the magnetic fluctuations directly (Figure 8.2-2). The feedback was able to suppress external kink fluctuations as measured by the Rogowski diagnostic completely. The integrated fluctuation amplitudes in Figure 8.2-2 are not reduced to zero because there is (mostly high frequency) noise in the signals which is unaffected by the feedback system.

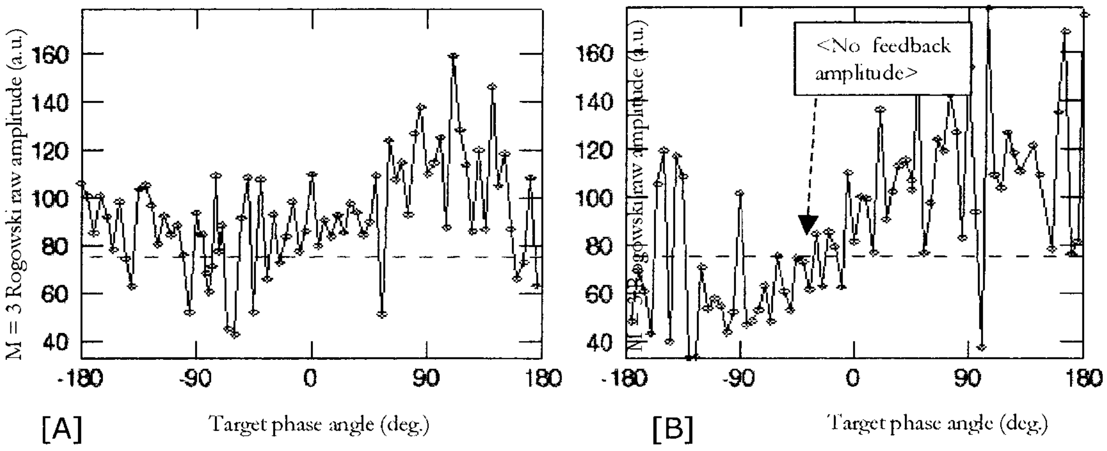

Figure 8.2-1: Raw m = 3 Rogowski coil signal amplitudes in interval 2 < t < 3 msec. A) with filter [A], B) with filter [B]

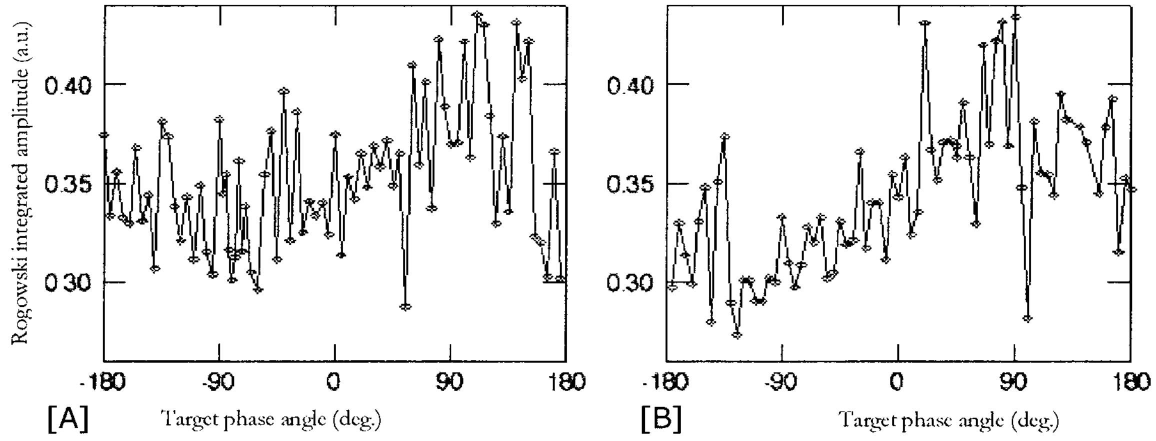

Figure 8.2-2: Integrated m = 3 Rog. coil signal amplitudes in interval 2 < t < 3 msec. A) with filter [A], B) with filter [B]

Much more revealing information is contained in the frequency content of the signals. Because of frequency dependent phase shifts, kink modes with faster than natural rotation rates may be excited if the toroidal phase of the control fields at high frequencies (~10 kHz) is more than 90 degrees shifted from the phase applicable to the natural rotation rate (~4 kHz). Figure 8.2-4 and Figure 8.2-5 illustrate this point.

The signal from the Rogowski coil was Fourier analyzed in the window $2 < t < 3$ msec, with the results plotted in polar plots where the radius is proportional to the frequency, and the amplitude is reflected in the choice of color for the particular point. The angle as before is a coordinate indicating the toroidal phase of the rotation operator in the digital feedback algorithm (0° is directly to the right, positive increase is counter-clockwise). For illustrative purposes, and to gauge how the feedback affects the naturally occurring external kink mode, Figure 8.2-3 represents this kind of analysis applied to three plasma-only shots (averaged) in which no feedback was applied. The angle is not defined, of course, and so the spectrum is simply reproduced for all angles around the compass. The interpretation of the plot is as follows: There is a naturally occurring external kink mode possessing a well defined frequency of 4.5 kHz and a characteristic amplitude (the Rogowski coils are not absolutely calibrated).

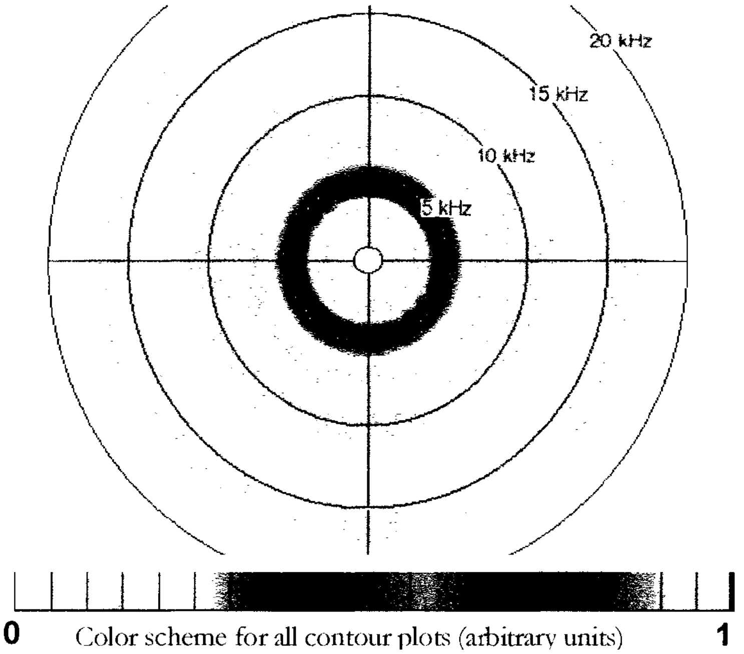

Figure 8.2-3: Natural (no feedback) mode, all angles (phase not defined without feedback)

Because the feedback transfer functions have frequency dependent phase shifts, and because the kink mode can experience a torque when the phase of the feedback field is such as to "push or pull" on the mode, the data exhibits spiral patterns that are very instructive for the feedback system designer.

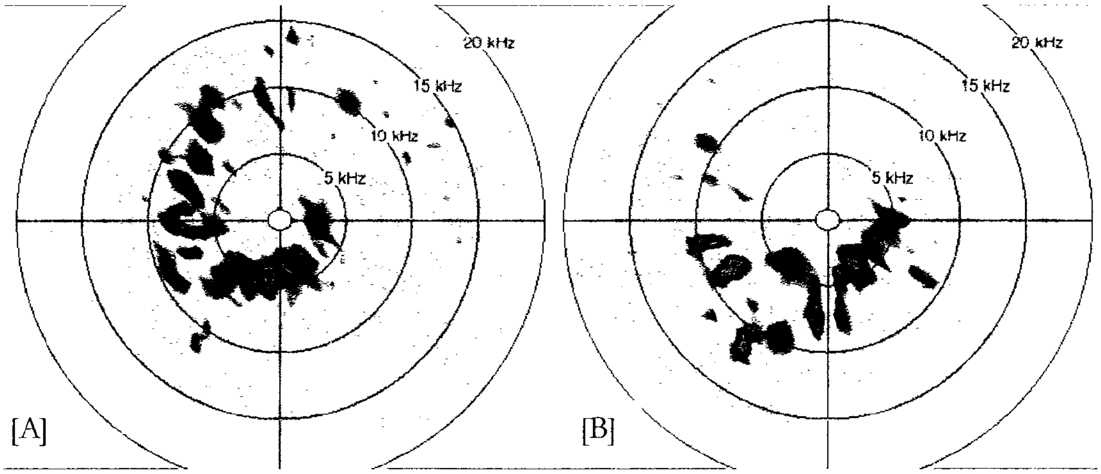

Figure 8.2-4: Amplitude of m = 3 Rog. signals (raw) for data obtained with digital filter [A] and [B]

Knowing how the phase of different frequencies is mapped toroidally (Figure 8.0-3), we can apply a transformation that "undoes" the phase shifting and produces a picture of the data which might have been obtained with a feedback system whose transfer functions exhibited no frequency variation in the phase transfer function. When this is done, the data obtained with filter [A] looks identical to the data from the filter [B] experiments as seen in Figure 8.2-5, and indicates that there is a broad phase angle which allows for negative feedback. It appears that as long as the control field has components which oppose the perturbed mode flux, it will act to reduce the perturbation, even if the phase is not perfectly adjusted for maximum results.

The raw Rogowski coil data is a measure of the rate of change of the magnetic fluctuations. To get a picture of the fluctuation amplitudes as a function of toroidal phase shift of the control field the signals were integrated and the analysis repeated. This data is shown in Figure 8.2-6.

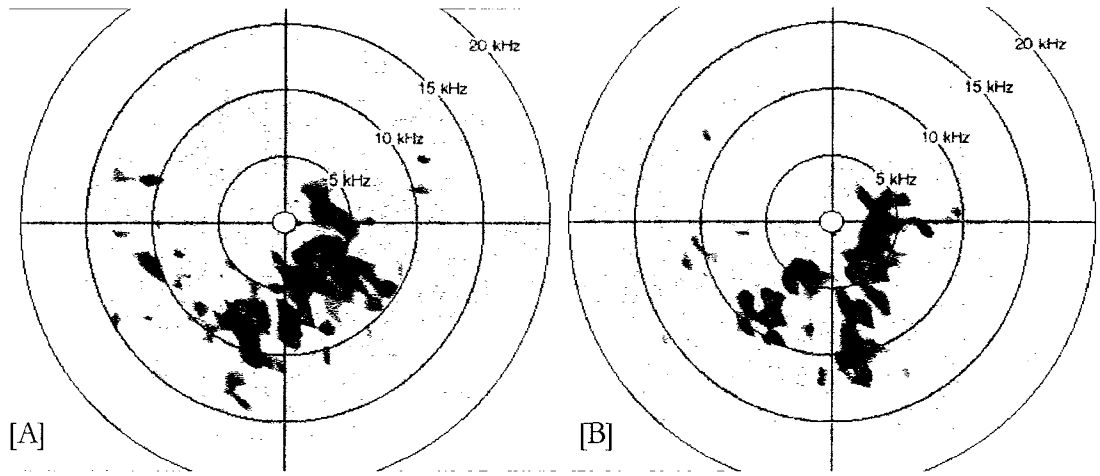

Figure 8.2-5: Amplitude of m = 3 Rogowski data with inverse toroidal phase mapping applied to compensate for transfer function phase shifts

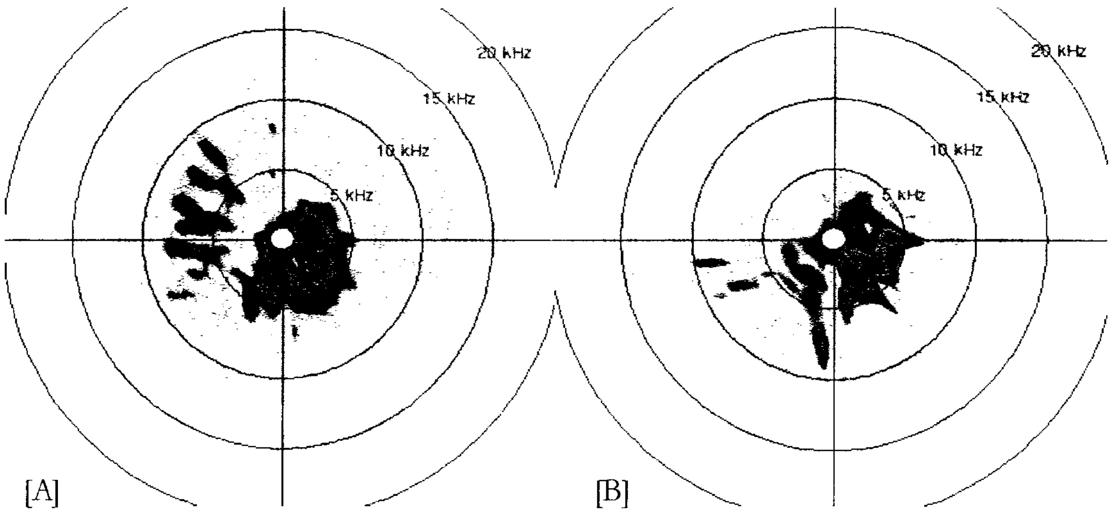

Figure 8.2-6: Amplitude contour spectrum plots of magnetic m = 3 fluctuations detected by Rogowski coils (integrated signals for data set obtained with digital filter [A] and [B]

In order to verify that the signals picked up by the Rogowski coils are entirely due to plasma MHD activity, and not direct vacuum coupling (magnetic inductive pickup) between the

Rogowski coil and the nearest control coils, the control coil currents as they were recorded during feedback shots were reproduced by calculating the voltage into the audio amplifiers required to drive the particular currents in the inductive coils and programming the digital processors to produce these voltages. The result shows that direct vacuum pickup constitutes a small fraction of the recorded Rogowski coil signals. For illustrative purposes, the data from two shots are shown in

Figure 8.2-7. The vacuum simulated shots were run with higher current levels (by almost a factor of two) to make sure to overestimate the vacuum coupling. Evidently, vacuum magnetic pick up is present, but negligibly small as seen in Figure 8.2-8.

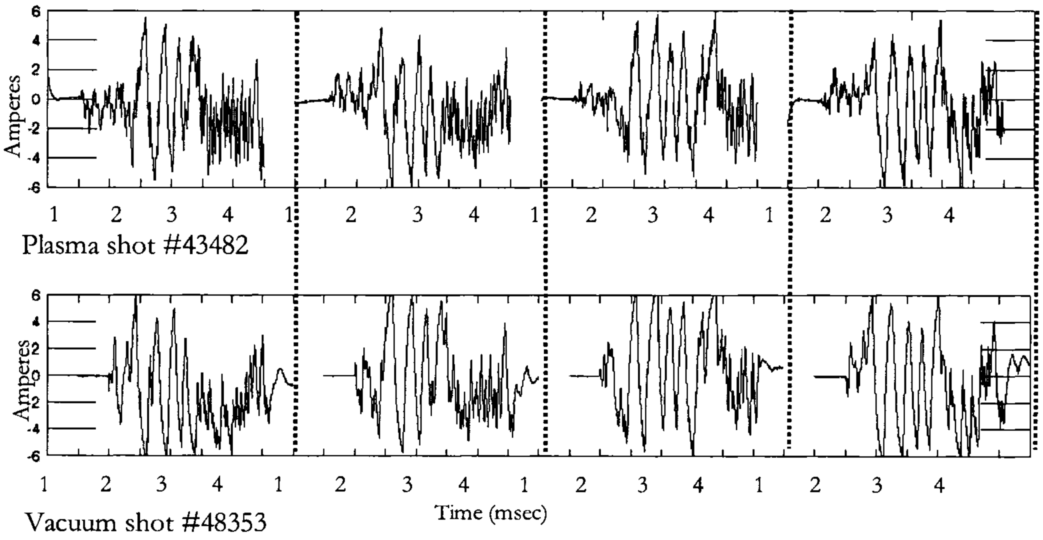

Figure 8.2-7: Control coil currents in coils at toroidal position T3 (near Rogowski coil) with and without plasma

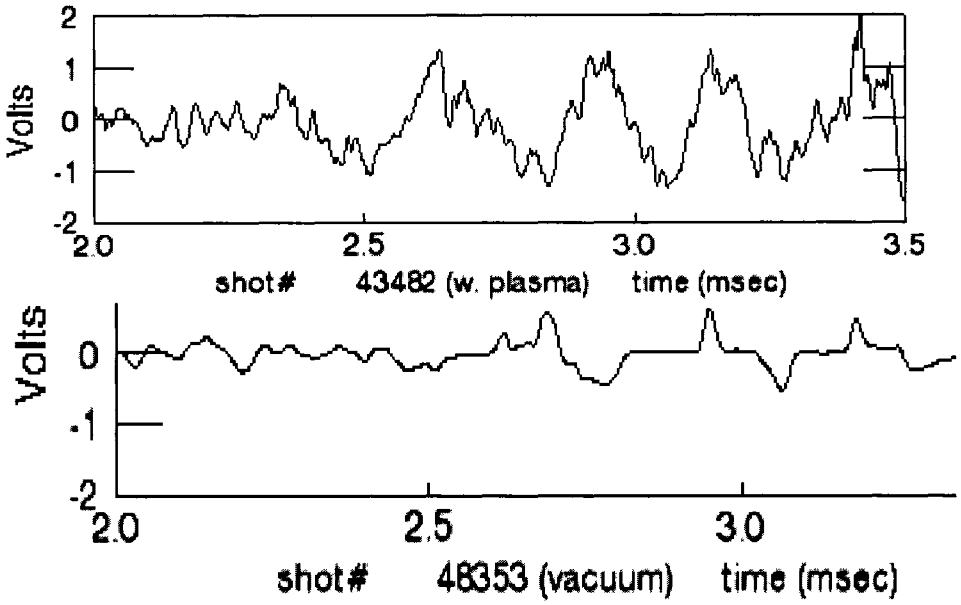

Figure 8.2-8: m = 3 Rog. coil signals for plasma (positive feedback) and vacuum shot with similar control coil currents

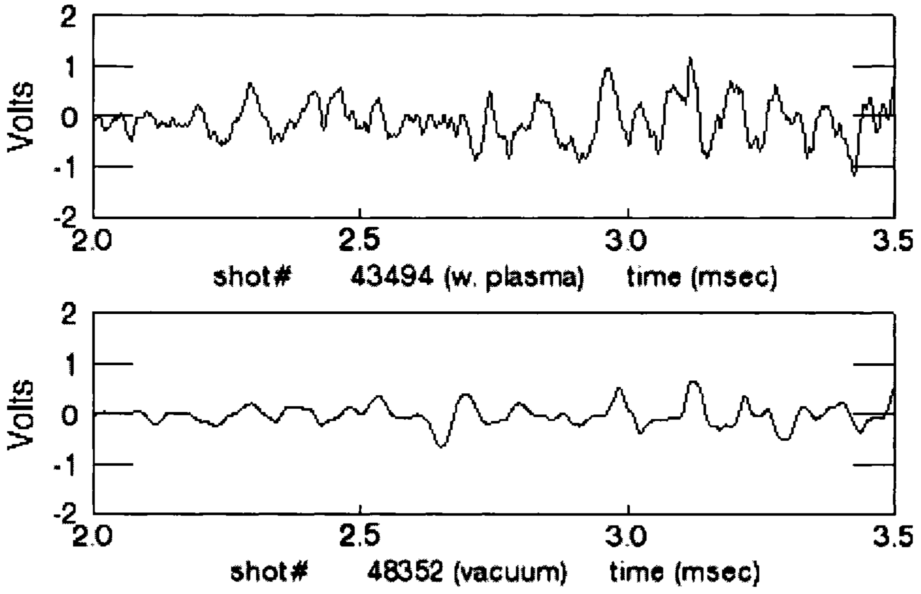

Figure 8.2-9: : m = 3 Rog. coil signals for plasma (negative feedback) and vacuum shot with similar control coil currents

8.3 Poloidal Sensor Analysis

The sensors which drive the feedback coils can also be used to gauge feedback effectiveness. They give a more global picture since they are arranged around the entire outboard of the tokamak, and should be more immune to noise from various sources because it is possible to look at only the n = 1 component of fluctuations via a discrete Fourier transform for each poloidal group. In addition, because the poloidal sensor array forms the input to the feedback system, and because there are no ambiguities about what Fourier modes are present in the system (toroidally), one expects the phase angle scan experiments to result in data that is a clearer indication of feedback effectiveness when compared to the Rogowski coil analysis. This was not necessarily the case, although the data does clearly indicate that the toroidal phase of the output signals sets the action of the feedback, as expected and consistent with the Rogowski data. However, the data from the poloidal sensor arrays was prone to noise even with the Fourier selection of the toroidal n = 1 component of the fluctuations, especially for the shots involving digital filter [B]. Those experiments occurred on a different day, and otherwise undetectable differences in the plasma equilibrium and chemistry seemed to have a strong effect on the signal quality from the sensors.

The first conclusion that is reached from the poloidal sensor analysis is that the plasma column sits low with respect to the vacuum chamber and toroidal field coil mid-plane. This can be seen by comparing the signal levels in the four poloidal groups. There is a consistent tendency for the sensors in the bottom shell to record larger amplitudes than the top shell sensors (Figure 8.3-1). Other diagnostics on HBT-EP subsequently confirmed the asymmetry in the tokamak geometry. This feature should not have much of an effect on the performance of the feedback system.

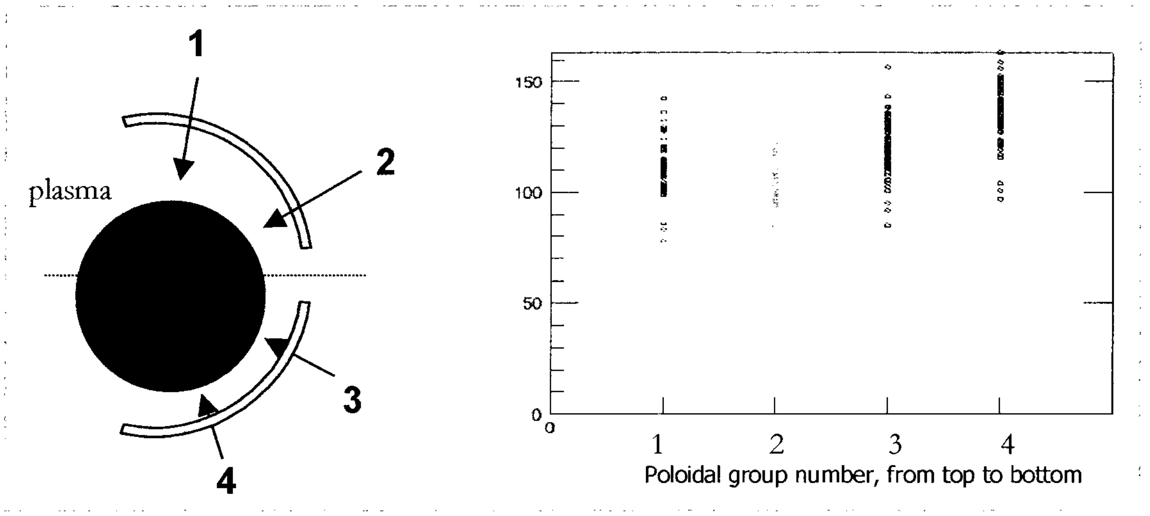
1
2
3
4
plasma
150
100
50
0
0
1
2
3
4
Poloidal group number, from top to bottom

Figure 8.3-1: Geometry of poloidal groups and average n = 1 fluctuation signal levels (71 shots) in each group

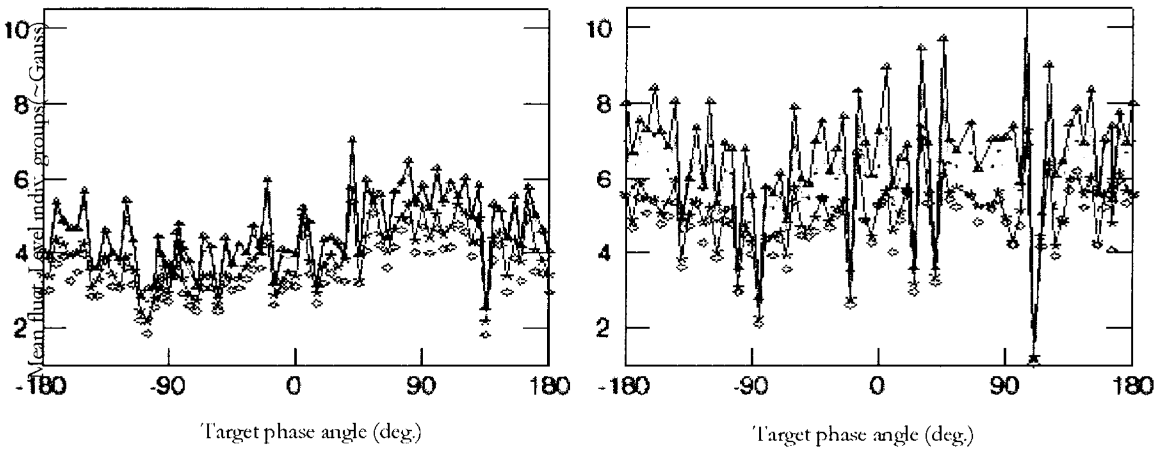

Figure 8.3-2: n = 1 component of magnetic fluctuations recorded by poloidal sensor arrays vs. target control field phase shift, data from four poloidal groups shown separately by color

8.4 Shell Mounted Probe (SMP) Analysis

The shell mounted probes consist of an array of sixteen small coils mounted on the inside of one pair of the thick aluminum shells and are schematically drawn in Figure 8.4-1. They are sensitive to poloidal magnetic field fluctuations, and because they are far removed from the nearest control coil (being located centrally in the control coil coverage gap between two toroidal control positions) they should give a good indication of the global external kink behavior under feedback. For all experiments described in this dissertation, the aluminum wall segments with the SMP's were moved to within 1 cm from the plasma surface so as to maximize signal levels.

The aluminum shells have a wall time that is much longer than the period of kink mode rotation (and even longer than the discharge itself). Consequently, the magnetic field at these sensors is subject to boundary conditions approximately the same as those for a field near a perfect conductor. These conditions are such that the radial field component vanishes at the surface of the shell, and the poloidal field component is approximately twice as large as would be found in a vacuum, both due to eddy currents in the shells which cancel the radial field and re-enforce the poloidal field at the shell's surface.

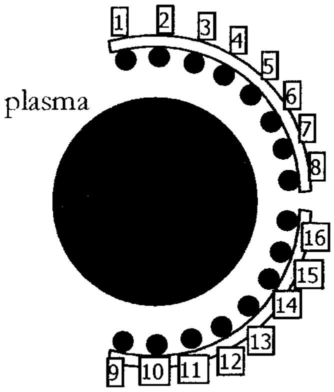

Figure 8.4-1: Schematic of poloidal shell mounted Mirnov array (SMP)

A contour plot of the partially integrated data from the SMP coil array yields a picture of magnetic fluctuations over a large (~200°) poloidal angle in HBT-EP. Figure 8.4-2 is a contour plot of the partially integrated signals and shows raw magnetic fluctuations as a function of time and poloidal angle. The expected m = 3 structure of the external kink mode is clearly evident, along with its time evolution (growth and rotation).

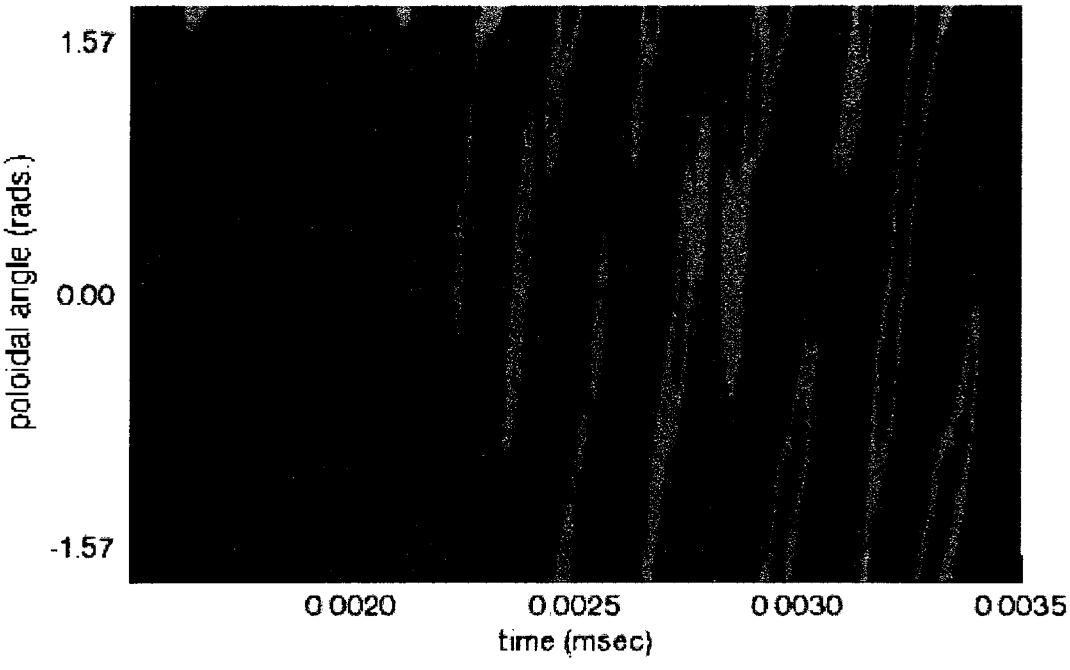

Figure 8.4-2: Contour plot of magnetic fluctuations in SMP for shot # 47169

Analysis of the SMP data can be performed in several ways. Fitting the data to a set of cylindrical Fourier modes might seem to be the natural way to proceed, but this method is not the most elegant for a finite ß plasma confined in a torus when the data is not evenly sampled poloidally. The Fourier decomposition can be improved when redefining the poloidal angle as outlined in section 5.3, and normalizing each channel of the array to reduce the effect of plasma vertical asymmetry, but this requires knowledge of the plasma current and pressure profile. The most effective analysis tools for the SMP array was determined by Cates to be based on a bi-orthogonal (also called singular value, SVD) decomposition[79], which separates all the data into the dominant temporal and spatial orthogonal modes regardless of plasma parameters and without a priori assumptions about the geometrical mode structures to fit to. This is especially advantageous in the case of data from HBT-EP since the plasma sits below the general experimental mid-plane. As an example, a bi-orthogonal analysis for a typical shot is presented in Figure 8.4-3 and Figure 8.4-5, which show the spatial and temporal structure of the six most dominant modes produced by the SVD computation. The modes come in pairs, akin to the sine and cosine components of a Fourier analysis. As is seen in the figures, the dominant mode has poloidal wavelengths comparable to an m = 3 Fourier mode, and its time evolution shows that it is by far the most important mode in the time interval 2 < t < 3 msec. The spatial mode structure that emerges from the SVD decomposition of the SMP array compares very well to the predicted DCON shape for the unstable m = 3 mode, which is shown in Figure 8.4-4.

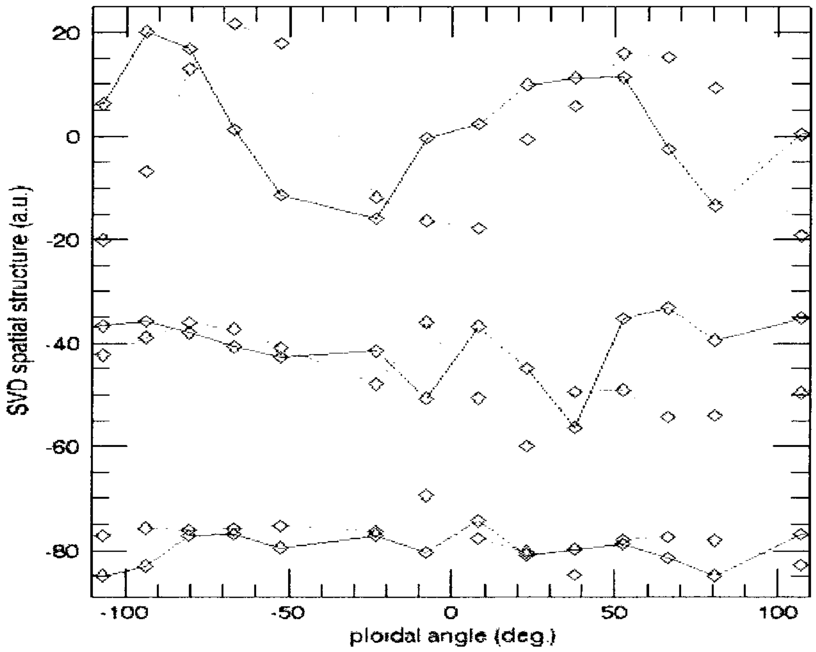

Figure 8.4-3: Spatial mode structure from SVD analysis in shot #44257 (each SMP signal normalized)

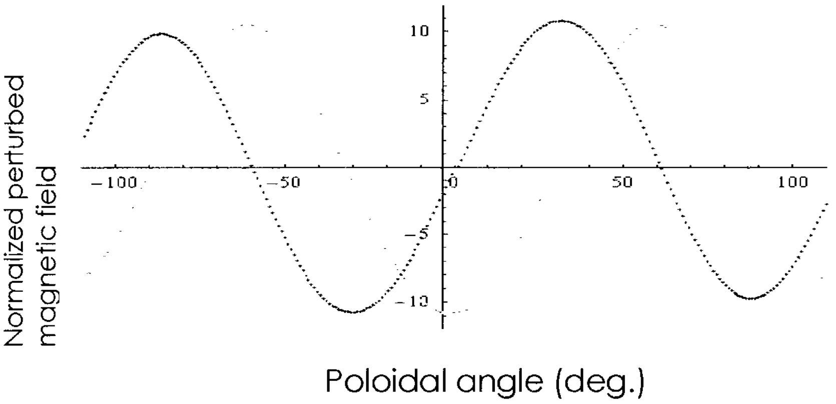

Figure 8.4-4: Unstable mode structure for m/n = 3/1 mode for shot #44257 as predicted by DCON

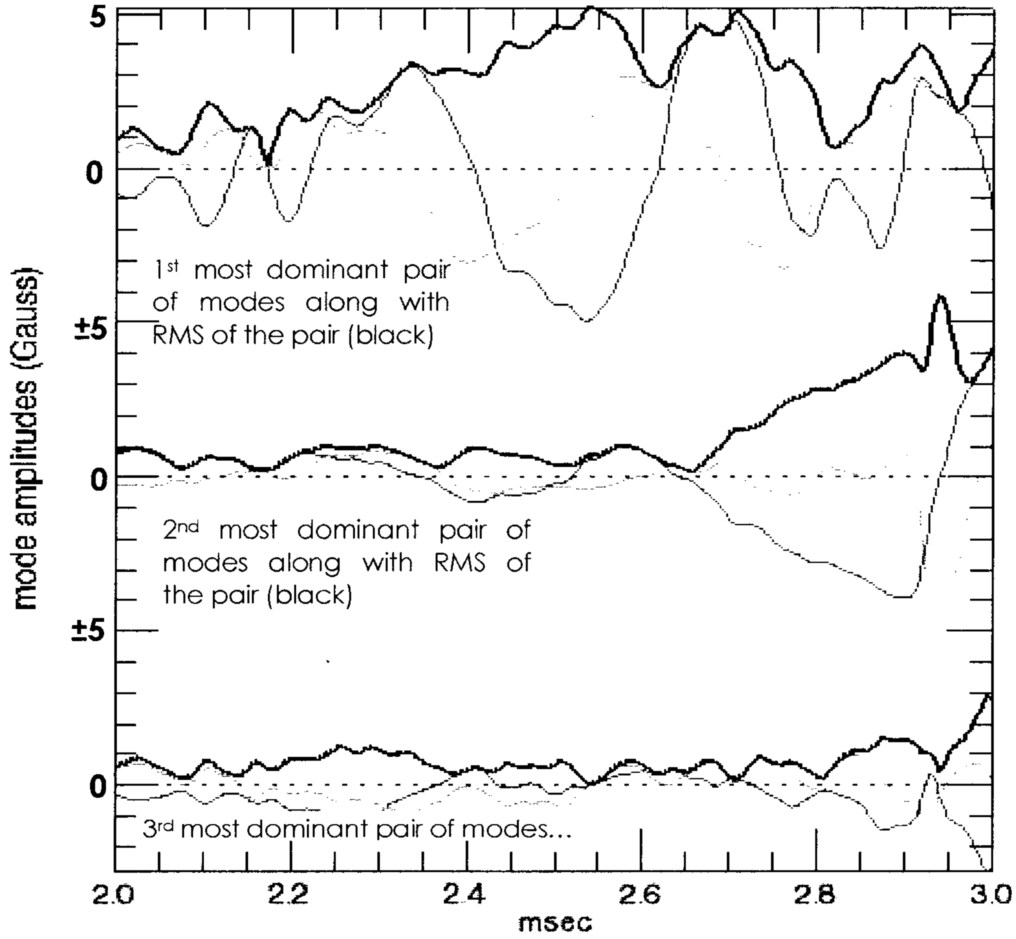

Figure 8.4-5: Time evolution of paired most dominant SVD modes (shot# 44257)

The mean amplitude of the dominant modes (m = 3) in the time interval 2.4 < t < 2.7 msec are plotted for all the discharges using digital filter [A] in Figure 8.4-6 (smoothed over shots). Again it is evident that maximum excitation of kink perturbations occurs when the toroidal phase shift of the radial response field is at 90° with respect to the measured poloidal mode component. The data for the discharges obtained with lead/lag compensator [B] and the SMP's in general is unfortunately relatively noisy. Choosing the time window when an automated analysis routine will pick out consistent mode amplitude differences is a challenge because small variations in the bulk discharge parameters will cause substantial time variation in the growth phase of the kink mode. Figure 8.4-7 depicts the m = 3 mode evolution for three discharges that had absolutely identical equilibrium parameters (see Figure 5.0-1), with and without feedback. For these shots, the effect of feedback is very clear.

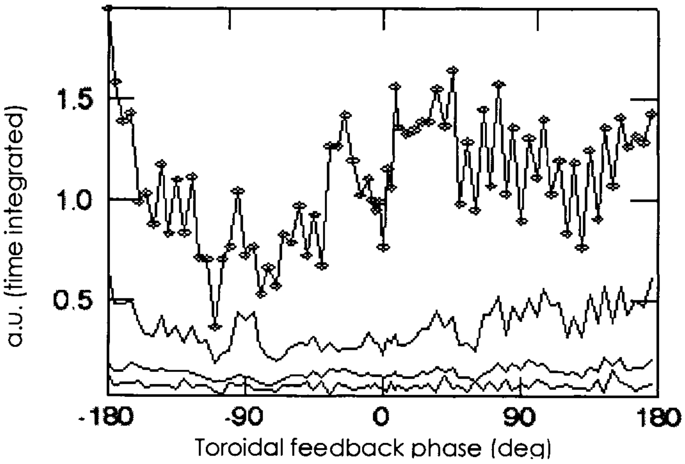

Figure 8.4-6: RMS of four most dominant mode pairs as identified by the SVD analysis from SMP signals during 2.4 < t < 2.7 msec (diamonds: mean m = 3 amplitude)

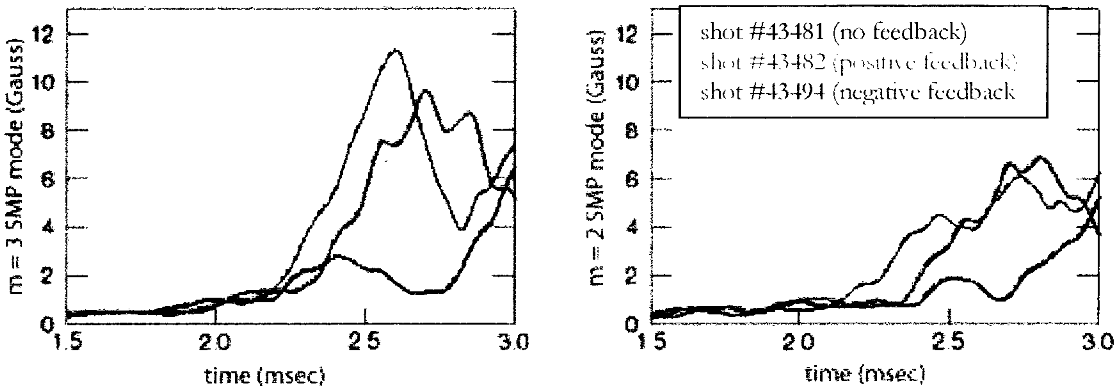

Figure 8.4-7: m = 3 and m = 2 mode evolution from SMP decomposition for three shots with and without feedback

To eliminate shot noise from the data, Figure 8.4-8 only shows the mean m = 3 mode amplitude for five shots each taken with feedback configured for maximum suppression and excitation of the external kink. That the feedback system has an effect on the SMP modes is clear, but the difference between using filter [A] and filter [B] is obscured by the discharge variability.

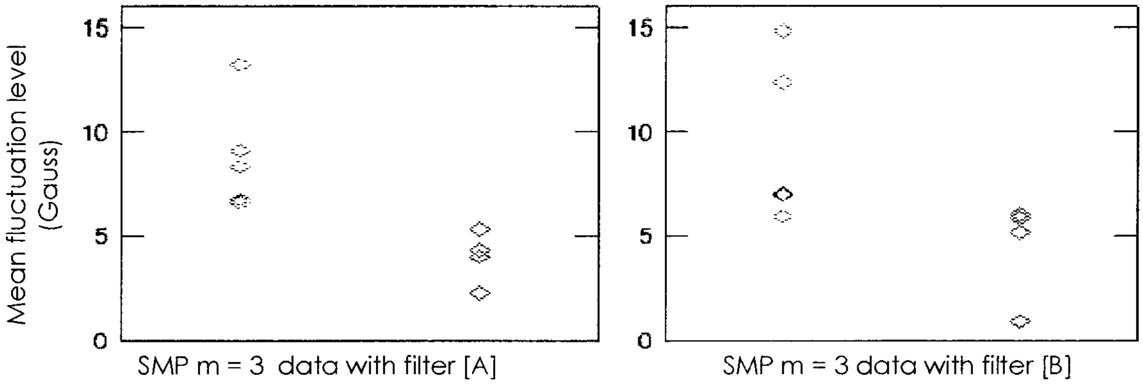

Figure 8.4-8: Several shots with control phase adjusted for maximum excitation (red) and supression (blue)

In summary of chapter 8, the data from Rogowski coils, shell mounted poloidal probes, and the distributed poloidal sensor array all indicates that feedback suppresses the external kink mode, and performs optimally when the phase of the radial control field is -90° toroidally shifted from the poloidal sensor field as would be expected for any $n = 1$ mode structure. Similarly, when the phase of the control field is inverted, maximum excitation of the modes is observed due to a positive feedback loop.

CHAPTER 9) GAIN SCANS AND GENERAL GAIN LIMITATIONS

In section 4.3 it was shown that the gain limits in the feedback system are much larger than the unity gain used in the feedback experiments. Even at lower gain settings however, the finite power available in the audio amplifiers limits practical gain in the system. For given sensor signal amplitudes it is unwise to increase the gain of the amplifiers to the point where waveforms cannot be accurately generated in the control coils due to power limitations. Distortion of the control coil waveforms introduces frequency components that are not desired and that will cause ambiguity of the $n = 1$ control phase, as well as introduce additional mode number components in the control field. The contamination of the control fields with $n = 0, 2$ components can be seen in Figure 9.0-1, where the toroidal mode amplitudes of the control output currents are plotted for two gain settings in the feedback. Each plot contains data from negative feedback shots. A gain of 1 is the setting used for all the feedback experiments and represents the maximum level of gain before obvious distortion of the waveforms is apparent. For a gain of 2, the amplitude of $n = 0$ and $n = 2$ mode components becomes significant.

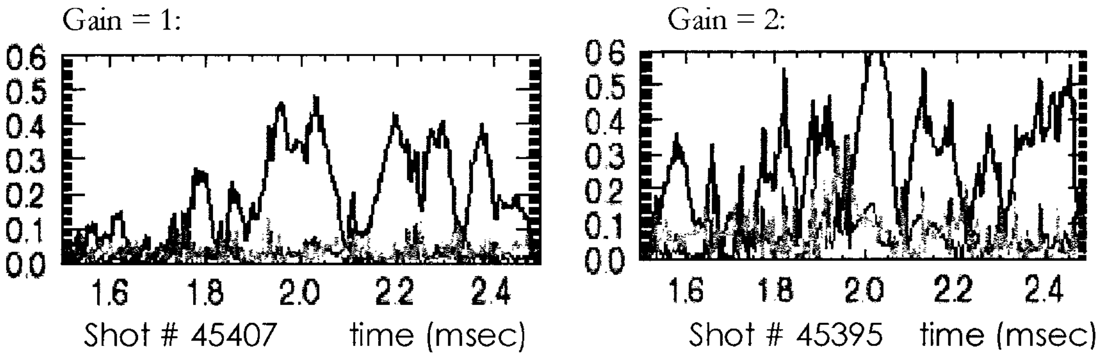

Figure 9.0-1: Control coil current mode amplitudes in bottom poloidal group for gain = 1, 2. Red: n = 1 mode amplitude, green and blue: n = 0, 2 mode amplitudes

Feedback performance was reduced if gain settings higher than 1 were used in the experiments. A set of detailed gain scan experiments was performed where six shots at six different gain settings were taken with feedback. At each gain, the rotation operator in the feedback algorithm was set to provide maximum excitation on kink modes for three of the shots, and maximum suppression for another three shots. The data clearly indicates that only for modest settings does the system perform negative feedback, and that as the gain is increased the system causes the excitation of a number of modes resulting in MHD activity which is greater than if no feedback was performed at all. In addition, the ability of the system to excite external kink modes is reduced for high gain settings as the feedback system cannot adequately track individual modes. To illustrate these results, Figure 9.0-2 depicts kink amplitude as recorded by the m = 3 selecting Rogowski coil for the gain scan experiments.

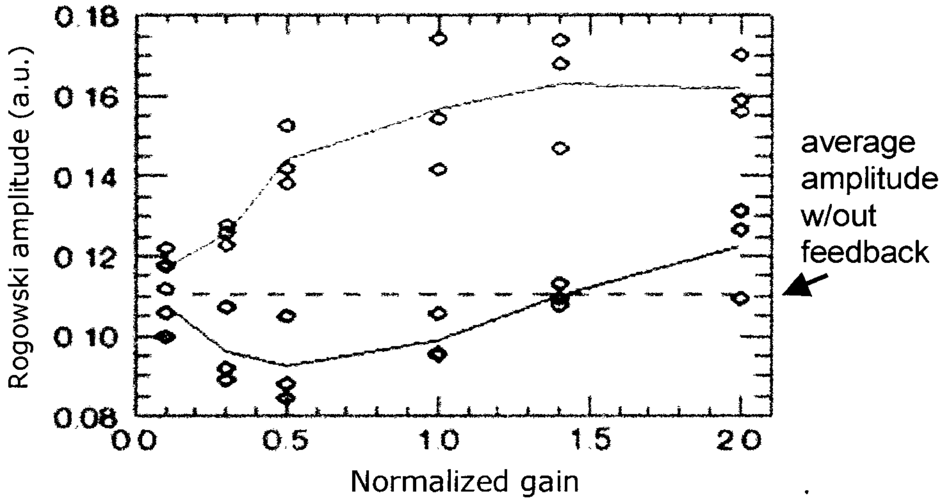

Figure 9.0-2: Mean m = 3 Rog. Coil amplitudes for exciting (red) and suppressing (blue) feedback shots at various gain settings during 2.2 < t < 2.7 msec

CHAPTER 10) PARTIAL COVERAGE SCANS

10.0 Mode Rigidity

An important question for the designers of MHD feedback control systems is: Can multiple, small, discrete coils be used to generate adequate fields to suppress long wavelength instabilities without having to resort to extraordinary gain and without driving large amplitudes in other (stable) modes? In the Boozer treatment of external kink mode physics, the plasma is represented as a simple and rigid electrical circuit. Furthermore, the single mode theory asserts that only the least stable eigenmode is sensitive to external perturbations and control fields, implying that the collection of circuits which form the set of eigenfunctions are not coupled. In such a world, the precise details of the control coil geometry only matter in that they determine the net mutual inductance between the coils and the dominant, least stable eigenmode, which in turn determines how effectively the system will couple to the mode and suppress instabilities. This sort of model will be inadequate to describe the kink mode dynamics if one of the following applies:

- If the mode is not in fact rigid, but changes shape in response to applied feedback fields
- If the dominant mode only represents part of the available set of modes into which substantial plasma kinetic energy can be expressed
- If the individual modes are coupled by internal non-linear mechanisms, toroidal effects, or via the feedback system

In the limit of infinitely small yet powerful control coils, all of these conditions must arise. These conditions are in fact all expressions of the same thing, namely, the relaxation of the constraint of mode rigidity. Furthermore, if there are multiple modes that are near marginal stability, one would expect these to respond noticeably to external magnetic perturbations that resonate with these modes. Extremely small control coils create fields that are rich in harmonic content, akin to the broad frequency spectrum found in the well known delta-function. Recent feedback experiments in a reversed field pinch (RFP) have confirmed that gaps in the coverage of control coils causes the excitation of kink modes with several mode numbers[80]. It is important to note that in the RFP there are usually a multitude of higher n numbered modes near marginal stability, while on the tokamak there is usually only one. But is this true near the ideal limit? There is theoretical work that predicts that gaps in the coverage of even a passive stabilization shell will allow the external kink mode to explode into the gaps when the mode is sufficiently unstable[81,82].

The problem of mode rigidity has only recently been addressed by a few authors[83,84], and the precise definition of what is meant by mode rigidity is not always consistent. In this thesis, mode rigidity is defined as the tendency for a particular MHD mode to retain a fixed geometry no matter what changes in external magnetic fields occur. An alternate popular definition involves the tendency for a given mode to retain its geometrical structure no matter what the bulk plasma parameters are. It appears in the literature on DIII-D that external kink and resistive wall modes are "rigid" when considering this latter definition.

10.1 Partial Coverage Phase Angle Scan Results

One simple experimental way to verify whether or not mode rigidity is a reasonable assumption is to measure magnetic fluctuations at some fixed location using a particular geometry of feedback coils, and then repeat the experiments with the feedback geometry modified in some way. In the absence of direct vacuum magnetic pick up from the control coils, the spatial structure of the recorded plasma fluctuations should not change, but only perhaps increase or decrease in amplitude as a consequence of altering the coupling coefficient between the control coil array and the plasma mode. Several such experiments were performed.

When additional gaps are introduced in the feedback coil arrangement, the data suggests that perhaps the kink modes are not perfectly rigid on HBT-EP. This may be peculiar to ideally unstable plasmas or a feature of external kink modes in general. The experiments involved the muting of control coils at two toroidal locations, labeled T1 and T3. Each of these two locations has one of the $m = 3$ Rogowski coils close by. If the $m/n = 3/1$ mode were completely rigid, both coils should record the same amplitude of signals for a given phase angle setting in the feedback loop for the case when the control coils at one or the other toroidal position are deactivated, because a) it has already been established that direct pick up in the Rogowskis is negligible, and b) there is no difference in coupling coefficient between control coils and the plasma in the two arrangements because the two scenarios represent merely a toroidal rotation of geometry. What was observed however, is that the Rogowski coil near whichever section was muted sees a generally reduced difference between feedback shots configured for exciting and suppressing phase angle. The data thus implies that mode control could potentially fail to completely and globally control MHD instabilities if there are large gaps in the arrangement where no control coils are located.

Described in this section, there are three sets of experiments. For the first, the toroidal phase angle scan was repeated with all control coils active as in chapter 8, because substantial time had elapsed since the earlier experiments and it was felt to be important to establish a base line and perform experiments with highly similar plasmas (HBT-EP, like most plasma experiments, is very sensitive to the surface conditions and chemistry in the vacuum chamber). The second set of experiments was conducted with the control coils near toroidal position T1 muted, without changing the algorithm for feedback and with all sensor coils active. Finally, the third set of experiments was identical to the second but with the control coils near toroidal section T3 muted instead. The arrangement of the coil coverages is shown in Figure 10.1-1.

For the full coverage scenario (36 shots), a clear and dramatic feedback effect is noted in the amplitude of the $m = 3$ selecting Rogowski coils both at positions T1 and T3, as seen in Figure 10.1-2. The difference between mode suppression and excitation are just as pronounced as detailed in section 8, and it seen that the difference between suppression and excitation is about a factor of two.

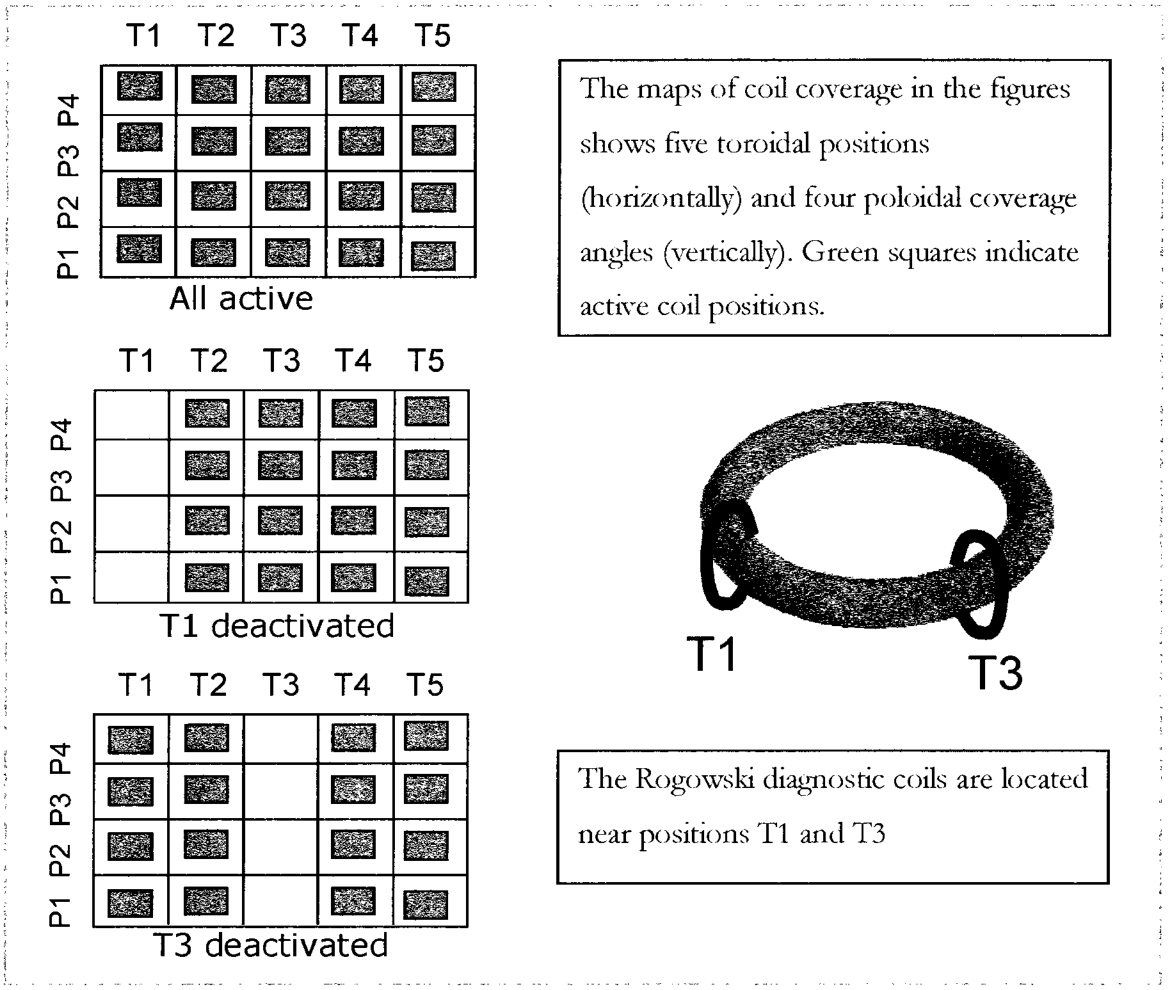
T1 T2 T3 T4 T5
P1 P2 P3 P4
All active
T1 T2 T3 T4 T5
P1 P2 P3 P4
T1 deactivated
T1 T2 T3 T4 T5
P1 P2 P3 P4
T3 deactivated
T1
T3

The maps of coil coverage in the figures shows five toroidal positions (horizontally) and four poloidal coverage angles (vertically). Green squares indicate active coil positions.

The Rogowski diagnostic coils are located near positions T1 and T3

Figure 10.1-1: Experimental arrangement for partial coverage phase angle scans: two Rogowski coils are at positions T1 and T3 near the control coils

When the control coils are deactivated at position T1, the diagnostic near that position indicates that the locally the mode appears to be less affected by the action of feedback system, as seen in Figure 10.1-3. The same sort of trend emerges when the control field is muted near position T3 (Figure 10.1-4). While the data is not overwhelmingly clear, this suggests a lack of mode rigidity in a region where there is a large gap in the coverage of control coils. With one toroidal position deactivated, the gap is very large (140°, nearly half of the toroidal circumference).

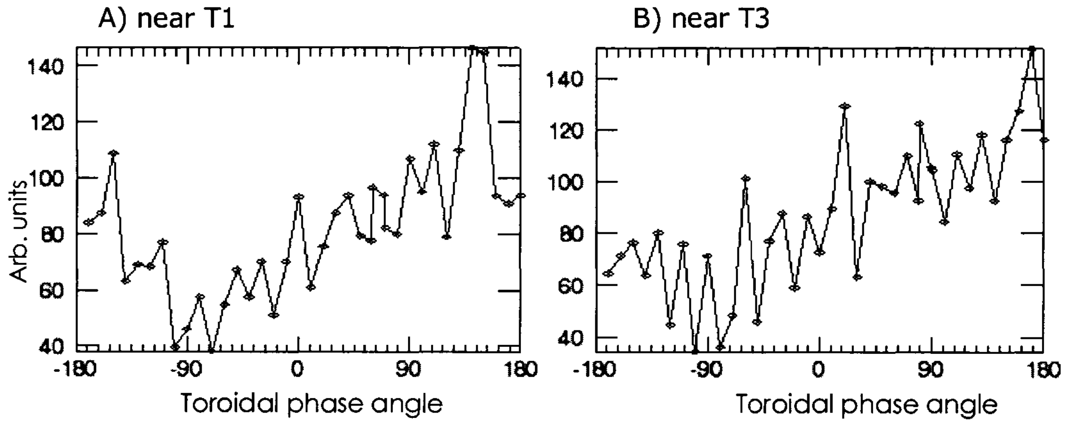

Figure 10.1-2: Amplitude of Rogowski coil signals vs. Feedback phase angle setting for each of the two Rogowski coils for 36 different shots, full coverage

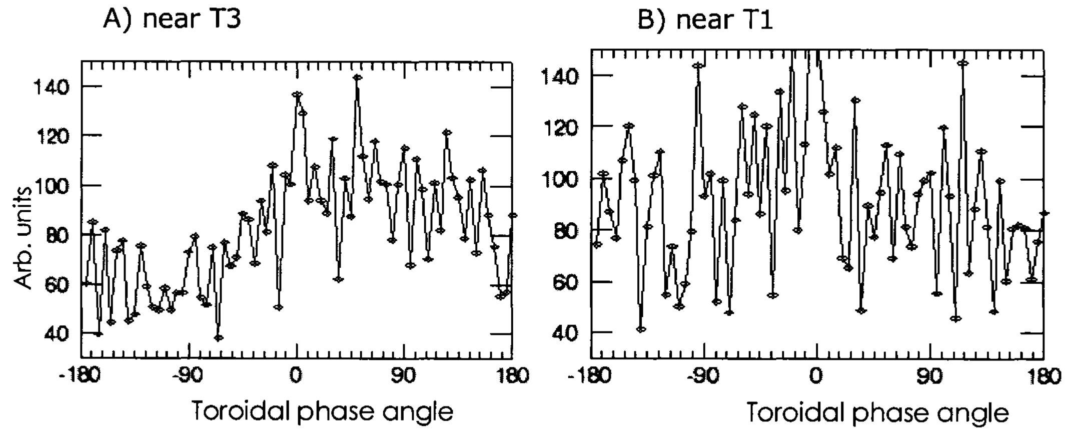

Figure 10.1-3: Amplitude of signals vs. feedback phase angle with coils near T1 muted

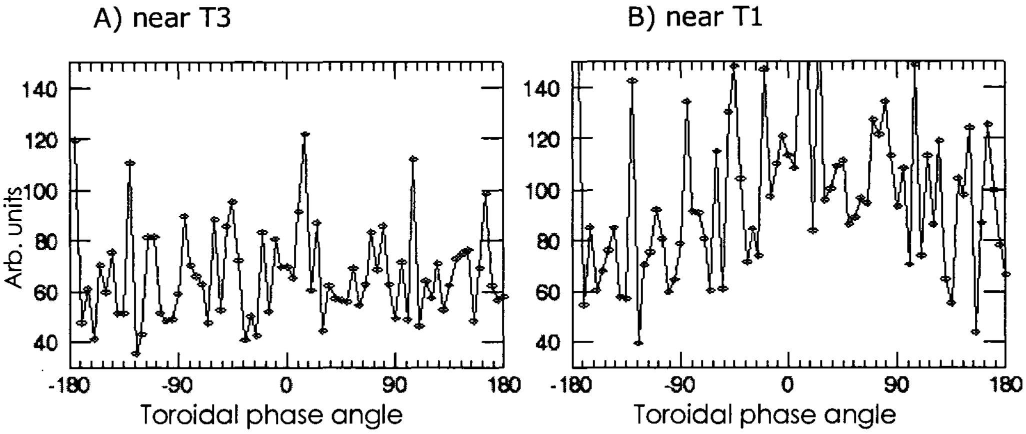

Figure 10.1-4: Amplitude of signals vs. feedback phase angle with coils near T3 muted

To summarize the results from the partial coverage experiments, Figure 10.1-5 shows several Rogowski coil amplitude data points for shots with the feedback system configured to produce maximum excitation as well as maximum suppression.

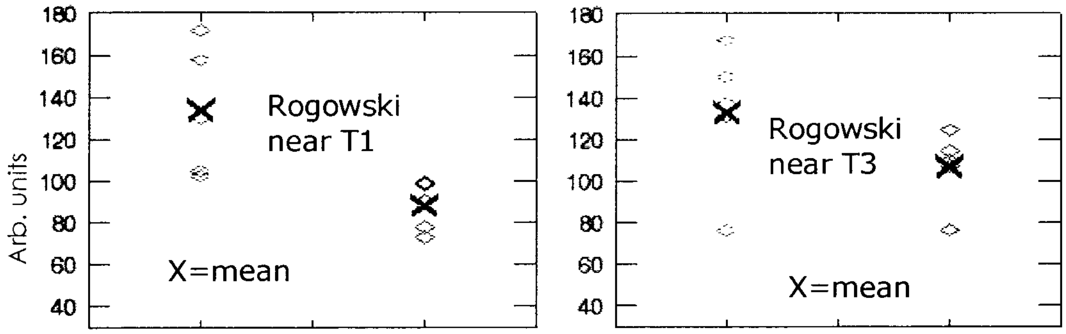

A) all c-coils active

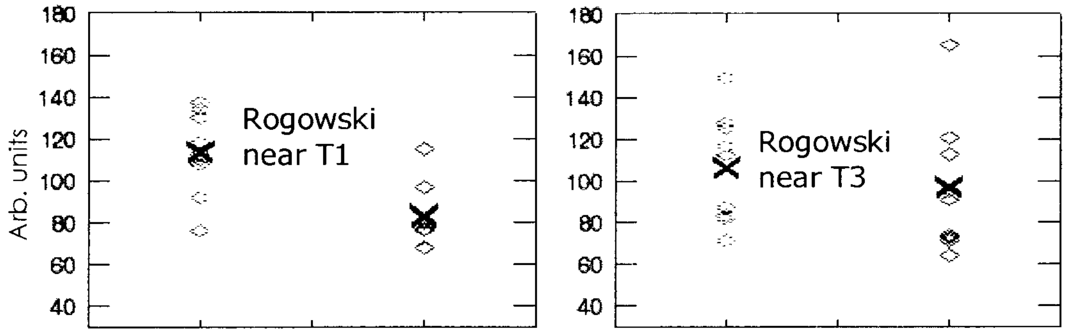

C) c-coils near T3 muted

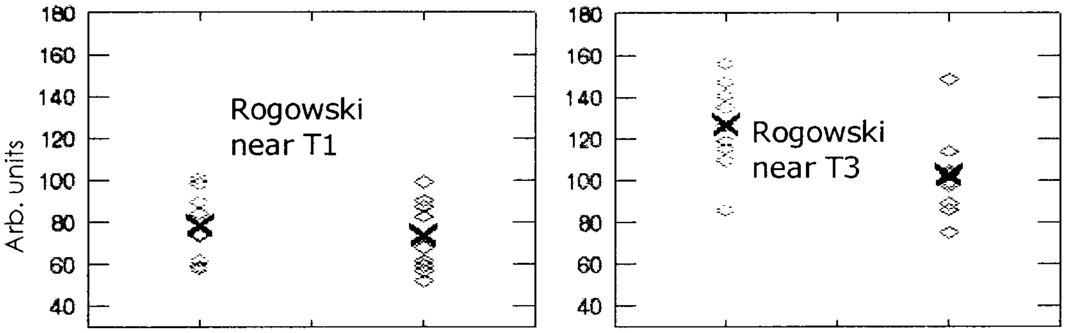

C) c-coils near T1 muted

Figure 10.1-5: Amplitude of Rog. signals for maximum negative (blue) and positive (red) feedback applied with a) all coils active, b) c-coils near T3 muted, c) c-coils near T1 muted

There is an oddity in the last two charts, indicating that suppressive feedback results in fluctuations with larger amplitudes near the active coils. This can be explained by noting that the two Rogowski coils have different sensitivities and gain, and that the sensor near T3 is generally much noisier. The ratios between exciting and suppressing data are more relevant.

The data from these experiments is not strong enough to merit a firm conclusion regarding mode rigidity, but certainly there exists a trend that would support the non-rigid mode picture. The issue should be examined in more detail in the future, with better statistics (more experiments) and additional coil and gap variability, as illustrated in chapter 11. Perhaps the non-rigid behavior is a feature peculiar to strongly unstable plasmas, as the discharges throughout these experiments are near the ideal stability limit. Perhaps the modularity of the control coils, especially with such a large toroidal coverage gap, prevents strong coupling between the coil array and the m/n = 3/1 kink mode, or it excites significant sidebands which could cause additional complications. This last issue is explored in section 10.2.

10.2 Side band excitation

The HBT-EP mode control system and smart shell control coil arrangement was modeled to determine how effectively the m/n = 3/1 mode is targeted when the coils are energized such as to drive the 3/1 mode and to compare the two systems in that respect. Because the mode control coils are highly modular, paired (connected in series) coils, they excite a multitude of sidebands, and only very little flux goes into the 3/1 mode as compared with the smart shell arrangement for example. In addition, when coverage gaps are introduced, this sort of analysis reveals how the data in section 10.1 might be explained in the context of an overall degradation of feedback system geometry and coupling between poloidal modes, many of which are near marginal stability.

The control coils and geometry for all the calculations were created using Radia, a free add-on package for Mathematica available from the European Synchrotron Radiation Facility (ESRF) in Grenoble, France. The method used in Radia belongs to the category of boundary Integral Methods and differs strongly from the Finite Element Methods (FEM), but the code has been benchmarked thoroughly in many different magneto-static applications. The magnetic field due to the coils (the current in each properly phased to produce a 3/1 eigenmode) was evaluated on a virtual plasma surface with circular cross-section, $R = 92$ cm, $r = 16$ cm. While the code can accommodate toroidal effects and rudimentary plasma _ effects, the results in this chapter were obtained with a simple Fourier analysis, treating the plasma surface as a periodic straight cylinder. The actual ratios of the various eigenmodes that are excited with the control coils are not expected to differ significantly from the results described in this chapter.

The plasma surface is divided into 720 toroidal and 72 poloidal points, and then IDL is used to evaluate the relative mode strengths for the two helicities (the helicity of the dominant 3/1 mode is defined as positive, the other helicity is identified with $n < 0$). The current in the control coils for the model is the same magnitude as that which is used in the HBT-EP experiment, but because the area elements of the surface are not included, the final mode flux amplitude must be multiplied by ~6 m^2 to have units of Weber. The important things to note are the relative amplitudes of the dominant mode and the sidebands for each configuration. The smart shell model uses currents which give the same voltage as in the mode control scenario (static current, so no inductance). Because the smart shell configuration has slightly longer current paths (for single turn coils), the current in the smart shell calculation is actually only ~65% of the current used in the mode control simulation, yet it couples very effectively to the 3/1 mode. The percentage of flux resonant with the m/n = 3/1 radial mode eigenfunction is calculated to be only ~3.4% for the mode control coils, as contrasted with 13.4 % with the smart shell configuration. These numbers are obtained in accordance with standard Fourier power mode analysis, with the flux percentage given by:

$$\eta = 100\sqrt{\frac{B_{3/1}^2}{\sum\limits_{m,n} B_{m/n}^2}} \qquad 10.2\text{-}1$$

The geometry of the smart shell model and the radial flux found on the plasma surface are shown in Figure 10.2-1 and Figure 10.2-2. Figure 10.2-3 shows the mode amplitudes in the Fourier spectrum for the first ten m numbered modes and n numbers up to +/- 50. A number of sideband harmonics are generated during feedback, but their amplitude is much smaller than the dominant 3/1 harmonic and the plasma is not expected to react strongly to these perturbations.

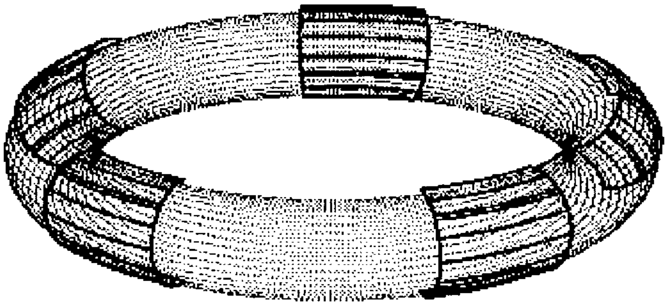

Figure 10.2-1: Smart shell control coil model showing location of control coils and plasma surface

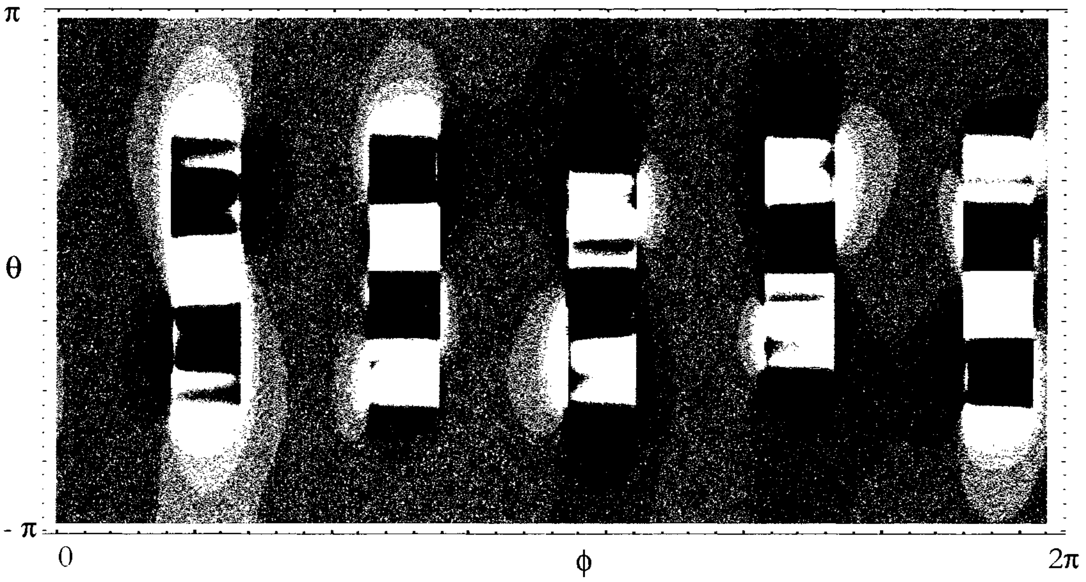

Figure 10.2-2: Flux contour plot of radial field on plasma surface produced by smart shell control coils

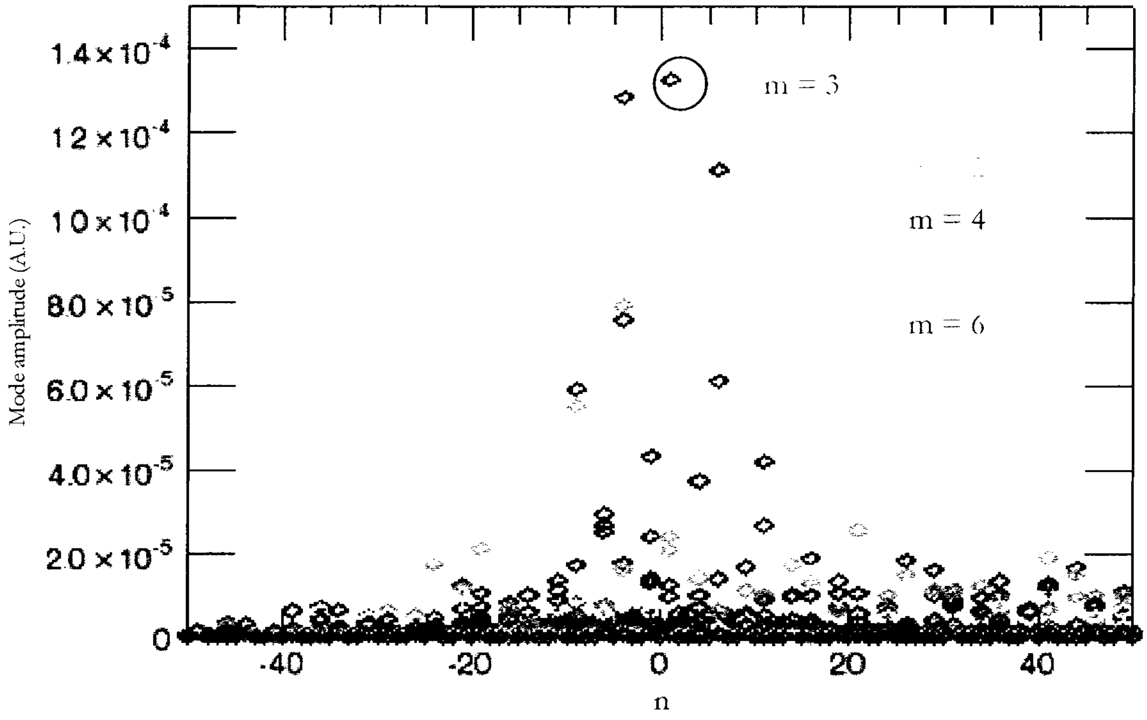

Figure 10.2-3: Mode spectrum from Fourier analysis for smart shell flux. 3/1 mode amplitude squared is 13.44% of the sum of all the modes squared

For the mode control model, the geometry and the resultant radial flux are shown in Figure 10.2-4 and

Figure 10.2-5. The mode amplitudes are shown in Figure 10.2-6.

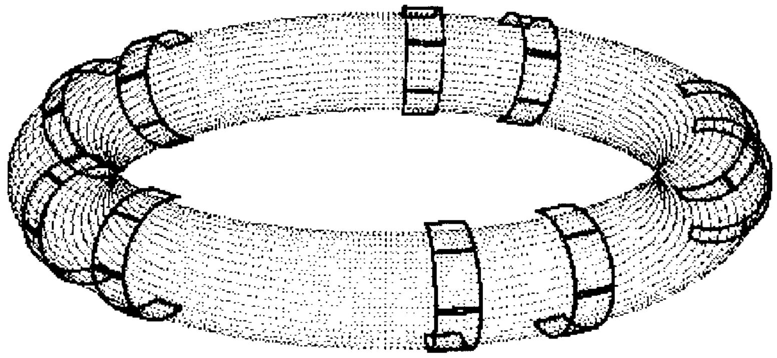

Figure 10.2-4: Mode control coil model showing location of control coils and plasma surface

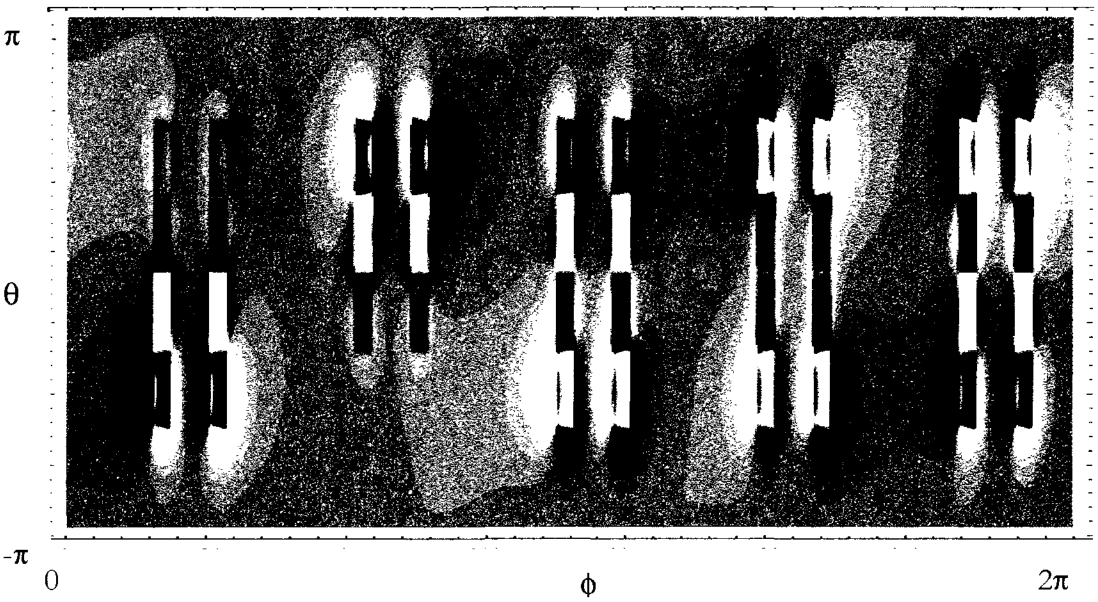

Figure 10.2-5: Flux contour plot of radial field on plasma surface produced by mode control coils

Apparently, a large number of sideband harmonics with substantial amplitude are generated during feedback. It is possible that some of these may be near resonant with the plasma. The feedback sensor array is sensitive to any n = 1 perturbation, and since the response consists of a multitude of n and m numbered harmonics, the modes are all coupled via the feedback system in a complicated way.

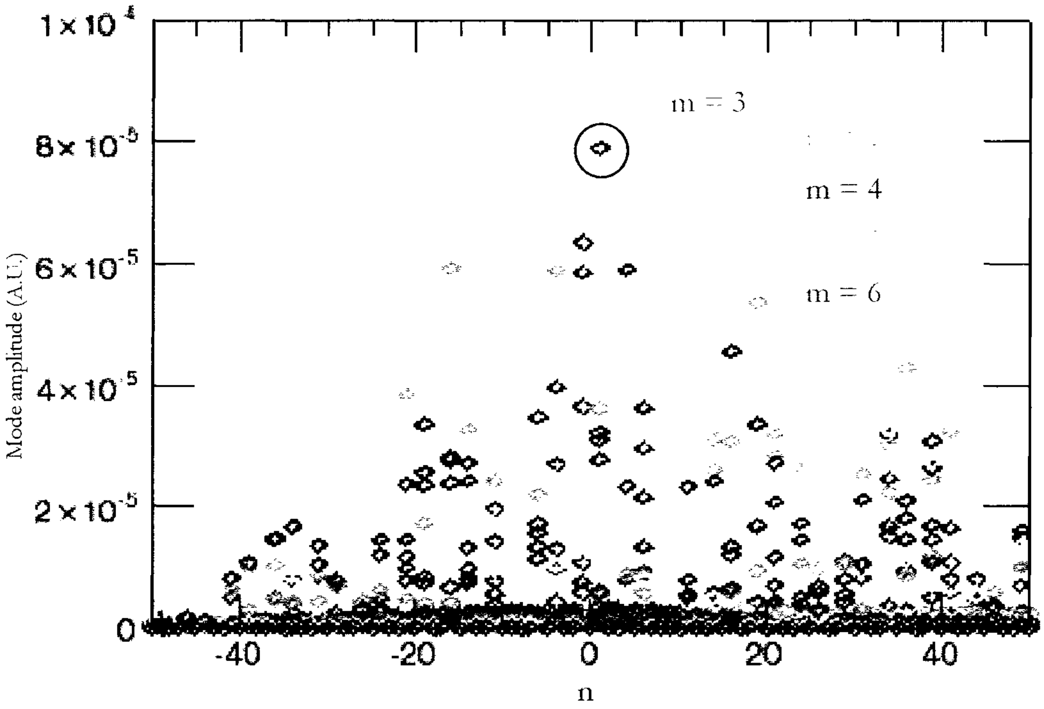

Figure 10.2-6: Mode spectrum from Fourier analysis mode control shells (paired). 3/1 mode amplitude squared is 3.4% of the sum of all the modes squared

The number and amplitudes of sidebands which are not the target of the control system becomes substantially greater when one toroidal position is host to a disabled set of control coils, since the toroidal coverage gap that results spans nearly half of the tokamak circumference. The analysis for this situation follows and is shown in Figure 10.2-7, Figure 10.2-8, and

Figure 10.2-9.

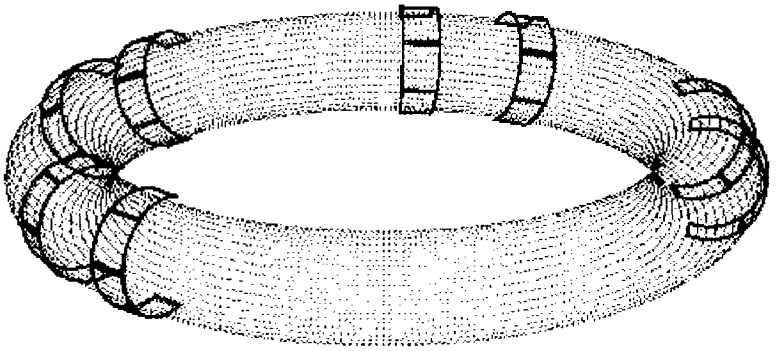

Figure 10.2-7: Mode control model with one toroidal coverage gap showing location of control coils and plasma surface

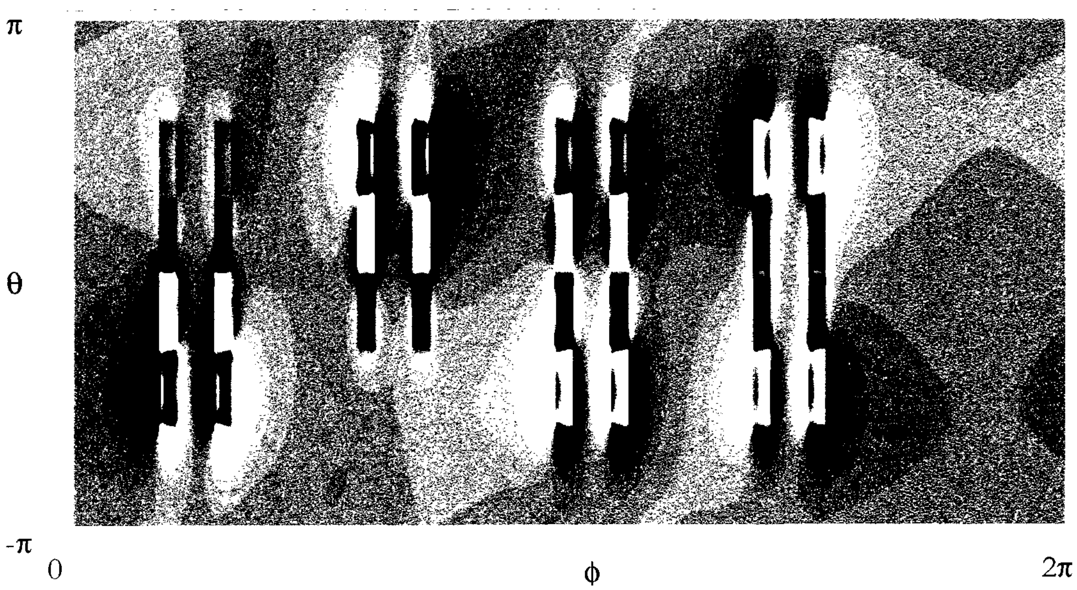

Figure 10.2-8: Flux contour plot of radial field on plasma surface produced by mode control coils with one toroidal position deactivated

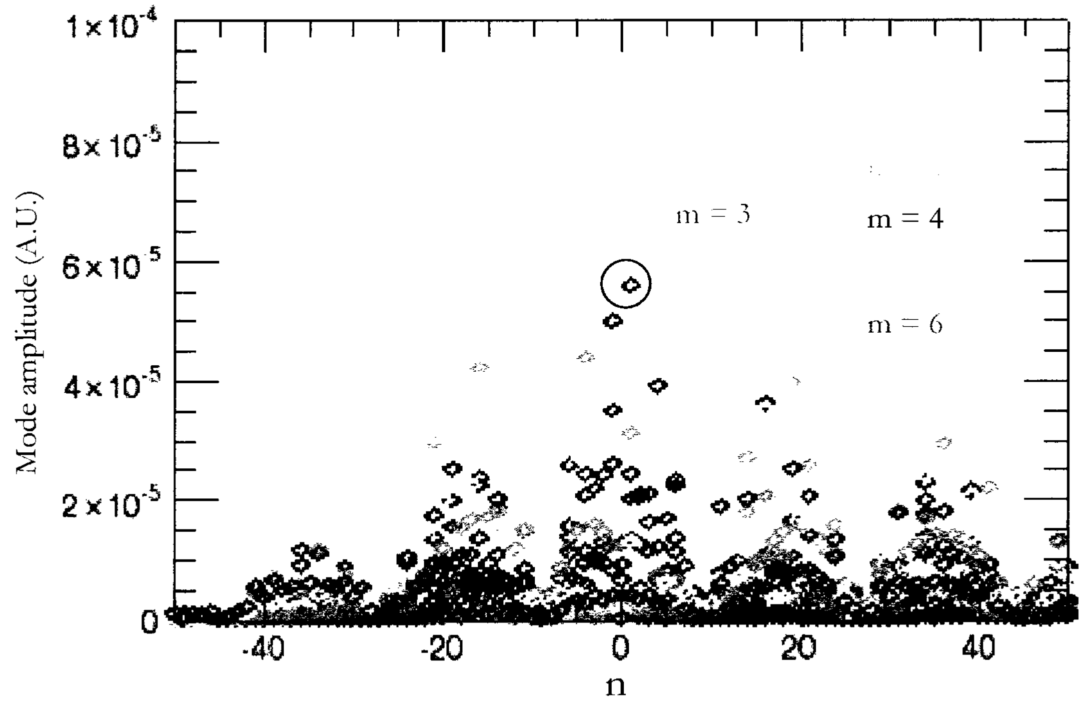

Figure 10.2-9: Mode spectrum from Fourier analysis mode control shells with toroidal coverage gap

Noticeable is that the m/n = 3/1 amplitude is reduced, but the number of sideband harmonics that is stirred up by the control coils is substantially increased. The plasma can produce a paramagnetic or diamagnetic response when interacting with a particular m/n numbered mode, depending on how far from marginal stability the plasma is for the mode in question. The instability parameter s from Boozer's kink mode treatment is well suited to consider each mode. It can be defined as the ratio of energies required to establish a unit amount of mode flux in the presence of a plasma over that energy required to do the same in a vacuum. For the typical discharge considered here, it turns out that there are a great number of modes (all of them stable) which can be considered to be near marginal stability, with Abs[s] < 1, as is seen in

Table 3 where DCON calculations for eigenmode energies reveal that many of these modes may cause a paramagnetic plasma response.. This gives rise to error field amplification, so that the plasma could react relatively strongly to a number of sideband harmonics.

Because the control coils generate a spectrum of modes, and the sensor coils may pick up the corresponding plasma response which in turn will drive the control coils, the multiple modes in the plasma are coupled together via the feedback system (they may be already coupled due to toroidal and/or non-linear plasma effects). Multi-mode coupling might allow the plasma to divert energy from the unstable mode into otherwise stable modes and thus avoid feedback stabilization. It could express itself as a kink that develops in the coil or wall coverage gap. The details of such a scenario are currently very difficult to model. At present, the VALEN code is being upgraded to accommodate multi-mode considerations.

n = 1		**n = 4**		**n = 6**	
δW	s	δW	s	δW	s
-1.53E-01	0.01	6.11E+01	-0.32	5.24E+02	-0.41
4.92E+00	-0.04	1.02E+02	-0.38	6.80E+02	-0.44
2.25E+01	-0.15	1.77E+02	-0.79	9.05E+02	-0.86
5.52E+01	-0.24	2.90E+02	-1.10	1.22E+03	-1.83
6.87E+01	-0.34	4.60E+02	-1.36	1.67E+03	-2.36
9.35E+01	-0.48				
1.35E+02	-0.52				
1.80E+02	-0.71				
2.94E+02	-0.80				
3.71E+02	-1.05				
3.86E+02	-1.32				
n = 9		**n = 11**		**n = 14**	
δW	s	δW	s	δW	s
2.25E+03	-0.33	2.70E+03	-0.22	4.36E+03	-0.31
2.89E+03	-0.95	3.51E+03	-0.45	5.57E+03	-0.39
3.70E+03	-1.67	4.48E+03	-1.15	6.95E+03	-0.99
4.22E+03	-2.66	5.30E+03	-1.70	6.99E+03	-1.78

Table 3: DCON output list several modes near marginal stability for shot #43268

CHAPTER 11) FUTURE WORK AND CONCLUSION

11.0 Future Control Coil Modifications

To experimentally thoroughly investigate the effect of modular coils and coverage gaps in feedback configurations as applied to the external kink mode, the shells and control coils will be modified on HBT-EP to include ten toroidal control locations (as opposed to the active five used in the experiments in this dissertation), with various sizes of control coils with differing toroidal extent which then can systematically explore the effect of coverage gaps and coil size. The issues dealing with mode rigidity and discreteness of the control coils is crucial because it is experimentally much easier to construct small modular coil systems, especially on a burning plasma experiment such as ITER. If there is a problem with coil modularity it should be determined before ITER construction. The proposed HBT-EP coil configuration is modeled on the following pages and proceeds just as the sideband calculations did in the previous chapter. It is clear from these calculations (and evident in the figures) that larger coils dramatically reduce the sideband structure and allows the target mode to better dominate the spectrum.

The plan is for three kinds of coil sets to be constructed, with 5°, 10°, and 15° toroidal extent for the individual coils. A picture of the proposed arrangement is shown in Figure 11.0-1. The modal analysis as presented in section 10.2 is performed in the remaining pages of this section.

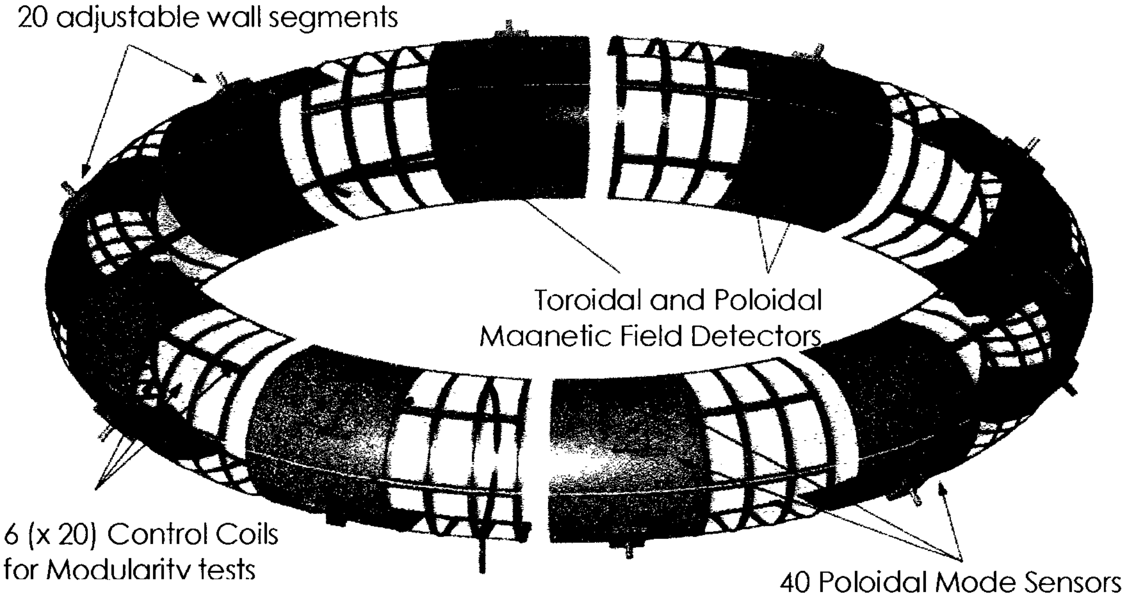
20 adjustable wall segments
Toroidal and Poloidal Magnetic Field Detectors
6 (x 20) Control Coils for Modularity tests
40 Poloidal Mode Sensors

Figure 11.0-1: Proposed feedback system to be installed on HBT-EP

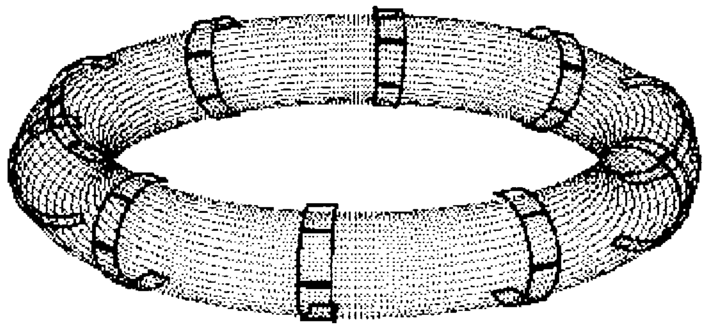

Figure 11.0-2: Model of future control coils (5° coverage) and plasma surface

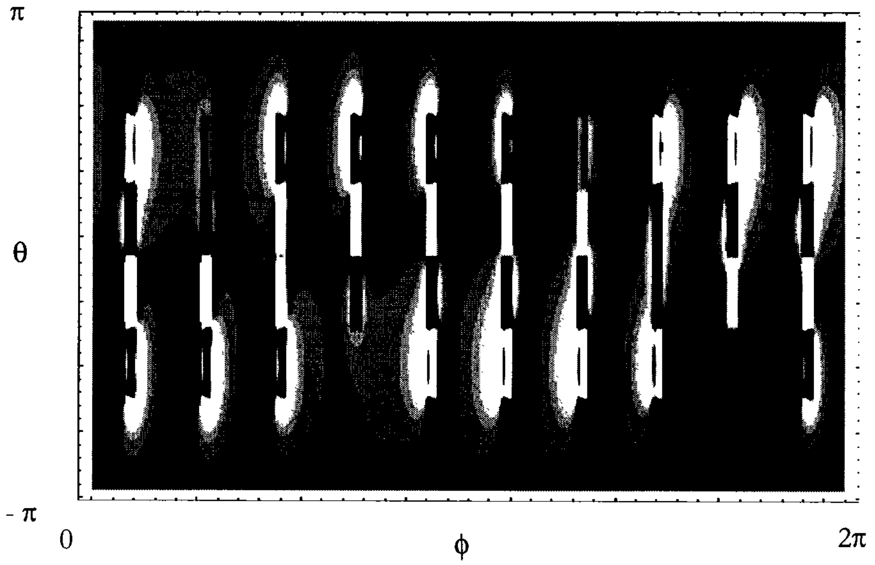

Figure 11.0-3: Flux contour plot of control field on plasma surface (5° coverage)

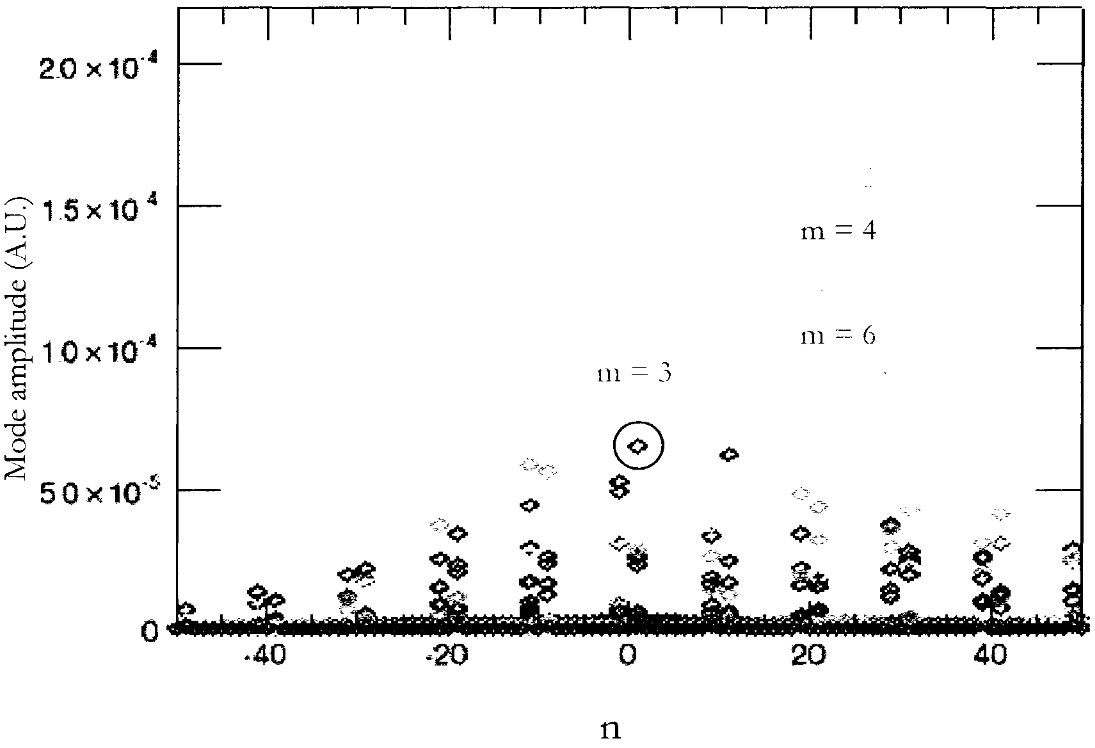

Figure 11.0-4: Mode spectrum from Fourier analysis when future mode control coils (5° coverage) are energized to produce m/n = 3/1 mode. The 3/1 mode amplitude squared is 2.6% of the sum of all the modes squared

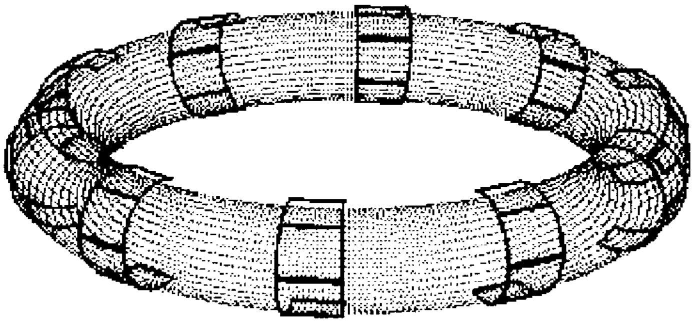

Figure 11.0-5: Model of control coils (10° coverage) and plasma surface

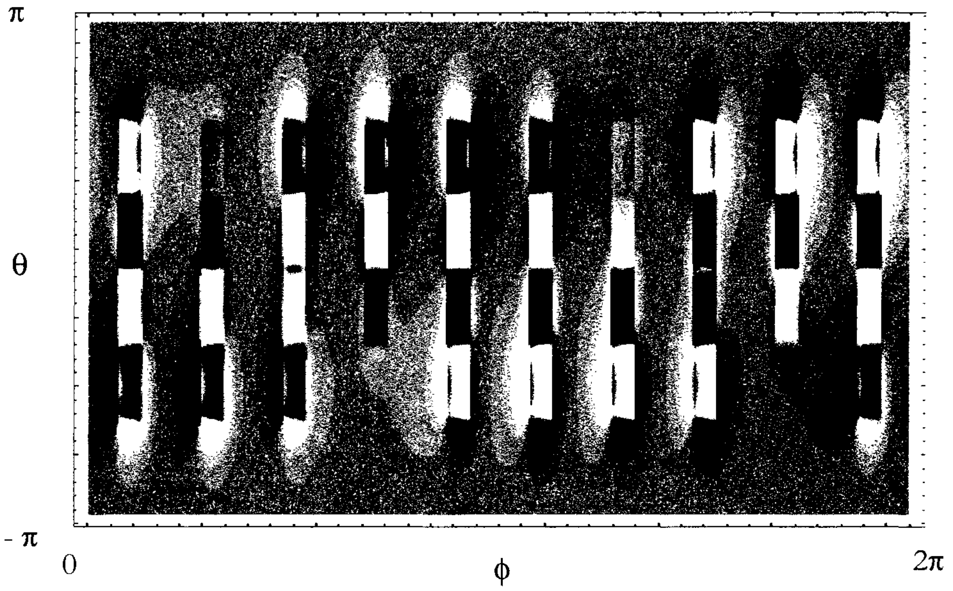

Figure 11.0-6: Flux contour plot of radial field on plasma surface produced by future mode control coils (10° coverage)

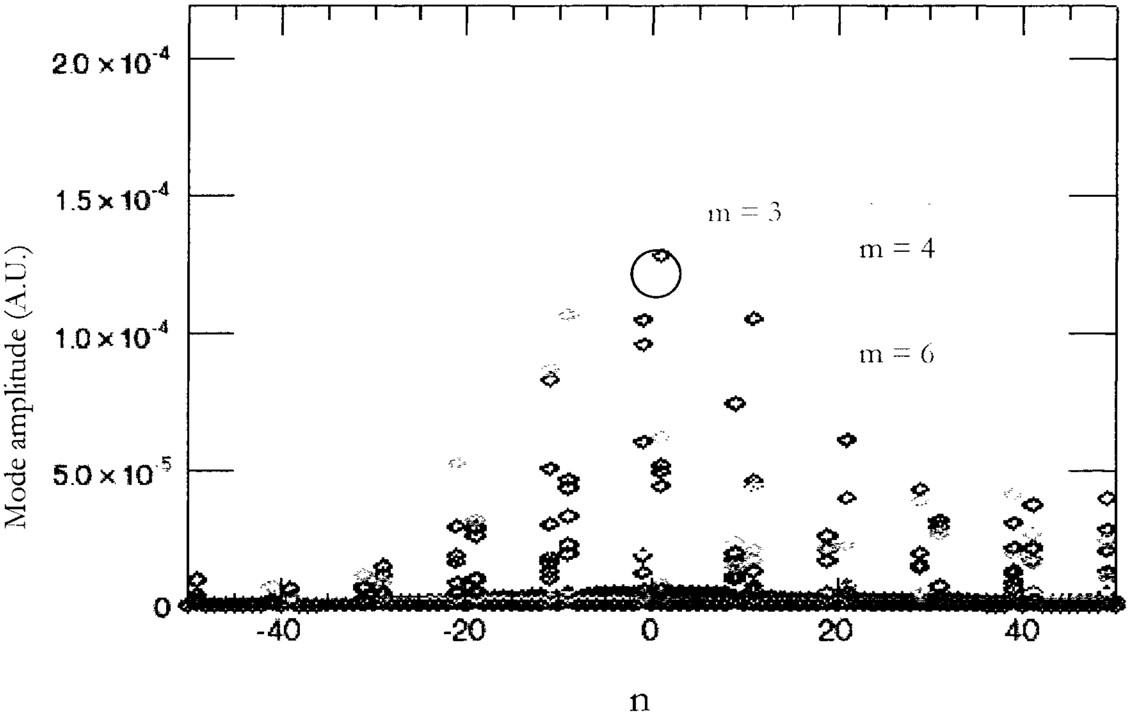

Figure 11.0-7: Mode spectrum from Fourier analysis when future mode control coils (10° coverage) are energized to produce m/n = 3/1 mode. The 3/1 mode amplitude squared is 5.92% of the sum of all the modes squared

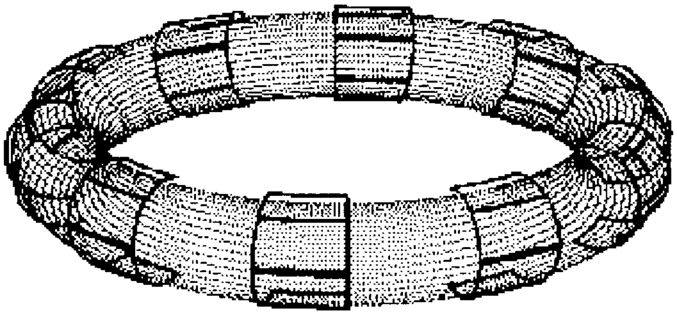

Figure 11.0-8: Model of proposed control coils (15° coverage)and plasma surface

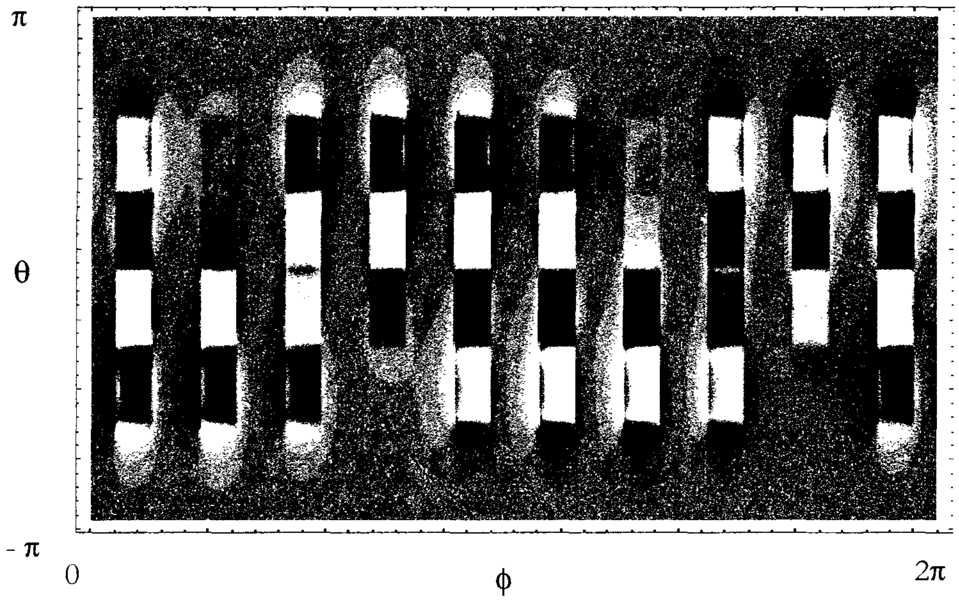

Figure 11.0-9: Flux contour plot of radial field on plasma surface produced by future mode control coils (15° coverage)

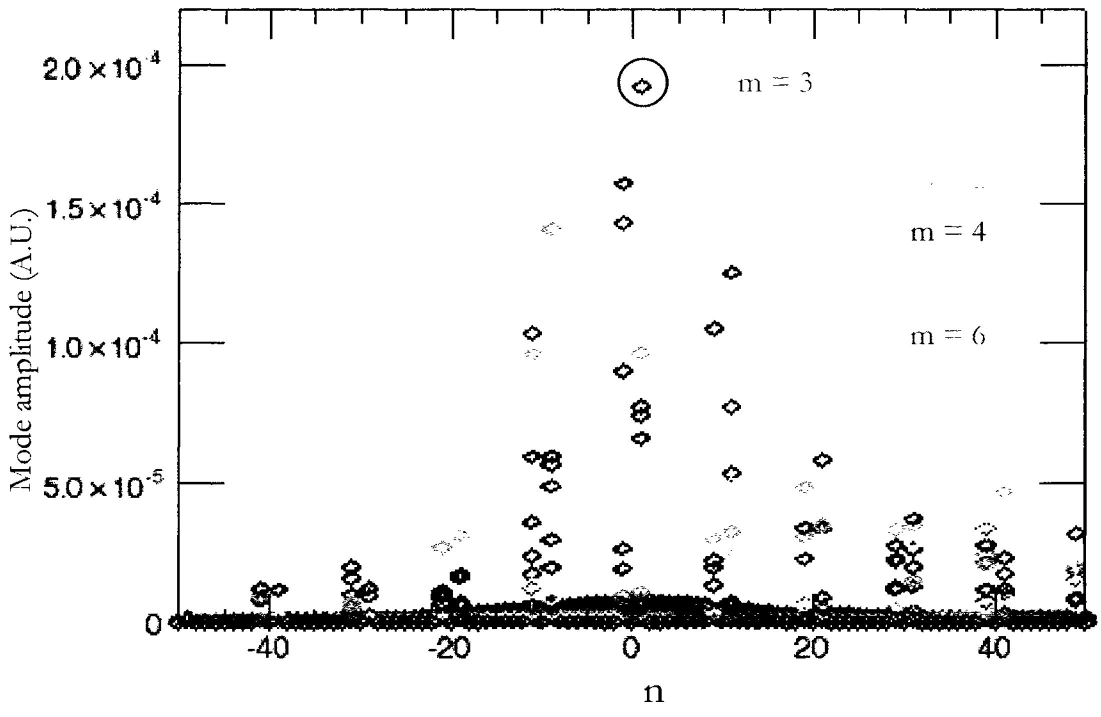

Figure 11.0-10 Mode spectrum from Fourier analysis when future mode control coils (15° coverage) are energized to produce m/n = 3/1 mode. The 3/1 mode amplitude squared is 9.4% of the sum of all the modes squared

11.1 Advanced Algorithms and noise reduction

In Chapter 8 the feedback suppression of external kink modes did not completely reduce the external kink mode amplitude to zero. While this is largely due to the noise introduced during the time averaging over a substantial window in the analysis, the system is also subject to noise on the magnetic sensors. The discrete Fourier transform operation which selects the n = 1 mode component of the toroidal signal array acts to reduce the noise in the feedback system considerably. Additional noise suppression can be achieved with the use of more sophisticated algorithms in the digital portion of the feedback. In particular, Kalman filters may prove to be a useful tool in designing feedback control algorithms that can reject non-kink mode events such as edge localized modes (ELMs) which are a concern in advanced tokamaks[85]. Additionally, plasma parameters could be incorporated into the feedback signal calculations to give tailor made response functions for different plasma regimes. The FPGA chips and National Instrument boards in the HBT-EP feedback system retain ample capability to incorporate a much higher level of complexity in the algorithms, without adding any significant latency for more than about one microsecond to the loop rates.

A short discussion of the NI 7834R modules will now be included in the context of future possibilities. The modules are ultra-compact PXI units with 8 analog in/out channels each, and 96 digital lines as well. Each module contains a large (3 million gates) LabVIEW configurable Xilinx II FPGA chip, flash memory, and 8 kilobytes of random access memory (RAM). They can be synchronized to external events and to each other to within a few nano-seconds. The power of these devices is that they can be instantly reconfigured to provide an entirely new feedback scheme at the touch of a button, and because the intuitive and familiar LabVIEW language is used to program the FPGA processors, programming itself is easily accomplished. The simple processing done for the experiments in this dissertation represent only a fraction of what could be done in terms of algorithm complexity. A module is shown in Figure 11.1-1 below.

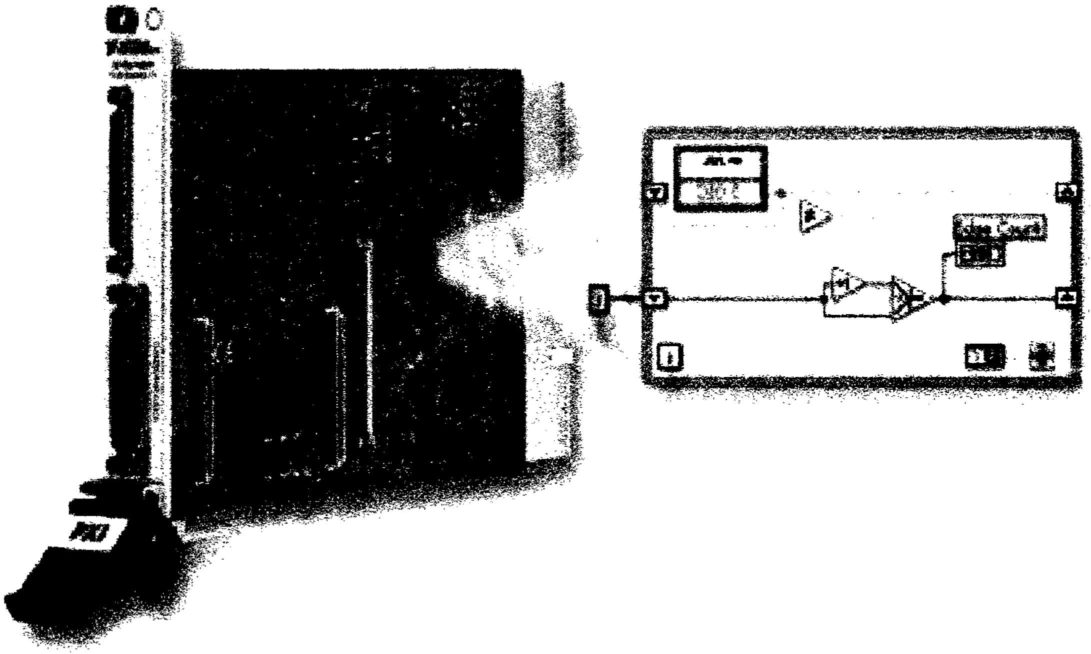

Figure 11.1-1: National Instruments 7831R module with LabVIEW programming illustration

With the planned installation of a large number of additional control coils and the versatility of the existing digital processing system, the capabilities and limits of mode control on external (and perhaps internal) MHD instabilities can be fully explored and hopefully contribute to the understanding and design of such systems on large reactor scale tokamaks such as the soon to be constructed ITER project.

11.2 Conclusion

Feedback on external kink modes is a promising route to high _ advanced tokamak operation. The mode control feedback system on HBT-EP utilizes small modular coils which project radial flux onto the outboard plasma surface, driven by high speed digital processors in response to poloidal perturbations as detected by a distributed network of flux loops. This system is able to suppress kink modes with very rapid growth rates, near the ideal wall limit.

The phase shifts in the transfer function of the system are crucial parameters that must be tailored to provide negative feedback for a range of frequencies, else the system will inadvertently drive instability at frequencies above or below the natural mode rotation rate. Relatively simple phase lag/phase lead compensation in the digital domain was used to accomplish the required phase transfer function. It is likely that a better design for control coils and analog filtering circuitry could result in feedback systems with extremely flat phase transfer functions over a broad range of frequencies.

There are unresolved issues dealing with the rigidity of external modes when these are strongly unstable. Large coverage gaps in the control coil arrangement result in local MHD activity which is unaffected by the feedback system. This may be due to multi-mode coupling and should be investigated in greater detail. How effective multiple, small coils can control long wavelength instabilities in tokamaks poses an important set of questions, as it may lead to simpler and less expensive control systems when compared to extensive and large coil systems which take up much more space and power on large reactor scale devices.

BIBLIOGRAPHY

---

[1] R.L. Hirsch, U.S. SAIC report (2005)

[2] Clean Air Task Force "An Analysis of Diesel Air Pollution and Public Health in America", (2005)

[3] U.S. Department of Energy, Report #:DOE/EIA-0484(2005)

[4] G.H. Miley, Fusion Energy Conversion, American Nuclear Society (1976)

[5] Congressional Research Service Report #IB91039, Library of Congress (2001)

[6] J.L. Bromberg, Fusion: Science, Politics, and the Invention of a New Energy Source, MIT Press (1982)

[7] F. Troyon, R. Gruber, H. Saurenmann, S. Semenzato, S. Succi, Plasma Physics and Controlled nuclear Fusion, 26 pg. 209, 1984

[8] M. Kikuchi, Plasma Phys Control. Fusion 35, pg. B39 (1993)

[9] R. Goldston, et al., Plasma Phys. Control. Fusion 36, pg. B213 (1994)

[10] C. Kessel, J. Manickam, G. Rewoldt, and W. M. Tang, Phys. Rev. Letters 72, pg. 1212 (1994)

[11] H. Zohm, et al., Plasma Phys. Contr. Fusion 45, pg. A163 (2003)

[12] E.A. Lazarus, Phys. Rev. Lett. 77, pg. 2714

[13] A. Gibson, Phys. Technol. 9, pg. 162 (1978)

[14] M.K. Vijaya Sankar, et al., Journal of Fusion Energy 12, pg. 303 (1993)

[15] J. Freidberg, Ideal Magnetohydrodynamics, New York: Plenum Press (1987)

[16] N. Krall & A. Trivelpiece, Principles of Plasma Physics, San Francisco Press (1986)

[17] K. Miyamoto, Plasma Physics for Nuclear Fusion, MIT Press (1980)

[18] A. H. Boozer, Rev. Mod. Physics 76, pg. 1071 (2004)

[19] I.B. Bernstein, E.A. Frieman, M.D. Kruskal and R. M. Kulsrud Proc. Royal Soc. London, Series A 244, pg. 17 (1958)

[20] H.P. Furth, J. Killeen, M. N. Rosenbluth, and B. Coppi, Plasma Phys. Contr. Nucl. Fusion Vol1 pg. 103 (1965)

[21] J.M. Greene, and J.L. Johnson, Plasma Phys., 10, pg. 729 (1968)

[22] S.V. Mirnov and I.B. Semenov, Soviet Atomic Energy 30, pg. 22 (1971)

[23] J. P. Freidberg, F. A. Haas, Phys. Fluids 16, pg. 1909 (1973)

[24] J. Wesson, Tokamaks, 2nd Ed., Clarendon press, Oxford (1997)

[25] A. B. Mikhailovskii, Instabilities in a Confined Plasma, Institute of Physics Publishing, Bristol and Philadelphia (1998)

[26] V.D. Shafranov, Soviet Phys. – Tech. Phys. 15, pg. 175 (1970)

[27] A.M. Garofalo et al., Nuclear Fusion 38, pg. 1029 (1998)

[28] A. D. Turnbull, T. S. Taylor, M. S. Chu, R. L. Miller, Y. R. Lin-Liu, Nuclear Fusion 38, pg. 1467 (1998)

[29] R. Betti, J.P. Freidberg, Phys. Rev. Letters 74, pg. 2949 (1995)

[30] L. E. Zakharov and S. V. Putvinskii, Sov. J. of Plasma Phys. 13, pg. 68 (1986)

[31] S.J. Allfrey, et al., Proc. Of the EPS, Prague (1998)

[32] M. S. Chu, et al., Physics of Plasmas 2 pg. 2236 (1995)

---

[33] R. Fitzpatrick, A. Y. Aydemir, Nuclear Fusion 36, pg. 11 (1996)
[34] A. M. Garofalo, et al., Physics of Plasmas 6, pg. 1893 (1999)
[35] J. B. Lister, Proceed. Of ICALEPCS2003, Korea, pg. 37 (2003)
[36] C. M. Bishop, Plasma Physics and Controlled Nuclear Fusion 31, pg. 1179 (1989)
[37] R. Fitzpatrick, T. H. Jensen, Physics of Plasmas 3, pg. 2641 (1996)
[38] C.C. Gimblett, Plasma Phys. Contr. Fusion 31, pg. 2183 (1989)
[39] C.C. Hegna, Phys. Plasmas 11, pg. 4230 (2004)
[40] P.R. Brunsell et al., Phys. Rev. Letters 93, pg. 225001 (2004)
[41] D.H. Edgell et al., Fusion Eng. And Design, V71, pg. 53 (2004)
[42] L.I. Artemenkov, et. al, JETP Letters 27, pg. 108 (1978)
[43] L.I. Artemenkov, Soviet J. Plasma Physics 5, pg.235 (1979)
[44] V.V. Arsenin et al, Proc. of 7th Int. Conf. of Plasma Phys. Cont. Nucl. Fusion, Vol 1, pg.233 (1978)
[45] M. Okabayashi, N. Pomphrey, R.E. Hatcher, Nucl. Fusion 38 , pg. 1607 (1998)
[46] V.D. Pustovitov, Plasma Phys. Contr. Fusion 44, pg. 295 (2002)
[47] General Atomics Report #A24851 (2004)
[48] A. H. Boozer, Phys. Plasmas, 11, 110 (2004)
[49] Y. Liu and A. Bondeson, Plasma Phys. Contr. Fusion 44, pg. L21 (2002)
[50] C. Cates, Ph.D. dissertation, Columbia University (2004)
[51] M.S. Chu, M.S. Chance, A.H. Glasser, and M. Okabayashi, Nucl. Fusion 43, pg.441 (2003)
[52] R. Fitzpatrick, Phys. Plasmas 9, pg. 3459 (2002)
[53] Mauel, et. Al., Nuclear Fusion 45, pg. 285 (2005)
[54] R. Fitzpatrick and A. Y. Aydemir, Nuc. Fusion 16, pg. 11 (1996).
[55] A. Bondeson and M. Persson, Nuc. Fusion, 28, pg. 1887 (1988).
[56] J. Bialek, A. Boozer, M.E. Mauel and G. Navratil, Phys. Plasmas 8, pg. 2170 (2001)
[57] A.H. Glasser, LANL report LA-UR-95-528
[58] A. Bondeson, G. Vlad, and H. Lutjens, Phys. Fluids B 4, pg. 1889 (1992)
[59] M. Mauel, Internal Memorandom, 15 May 2004
[60] M. Shilov, et al., Phys. Plasmas, 11, pg. 2573 (2004).
[61] A. H. Boozer, Phys. Plasmas, 5, pg. 3350 (1998).
[62] A. H. Boozer, Phys. Plasmas, 6, 3180 (1999).
[63] S. Sabbagh, et al., Proceedings of the IAEA (2004).
[64] A. Bondeson and M. S. Chu, Phys. Plasmas 3, pg. 3013 (1996)
[65] NEED PASSIVE PAPERS GAROFALO HERE
[66] National Instruments: "7831-R" modules with Xilinx II processors
[67] D. Stranneby, Digital Signal Processing: DSP and Applications, Oxford, 2001
[68] L.B. Jackson, Digital Filters and Signal Processing, 2nd ed., Boston 1989
[69] Allen H. Boozer, Phys. Plasmas 5, pg. 3350 (1998)
[70] G. Fussman, B.J. Green, H. P. Zehrfeld, Plasma Physics and Contr. Fusion Research (Proc. Int. Conf. Brussels, 1980)
[71] O. Chubar, P. Elleaume, J. Chavanne, J. Synchrotron Rad. 5, pg.481 (1998)
[72] M. K. Vijaya Sankar et al., Journal of Fusion Energy 12 pg. 303 (1993)

---

[73] C. Cates, et. al., Phys. Plasmas 7, pg. 3133 (2000)

[74] M. Mauel, L. Bai, Proc. 12th Int. Conf. Plasma Phys. Contr. Nucl. Fusion, 1, pg. 415 (1988)

[75] D.A. Maslovsky, A. H. Boozer, Physics of Plasmas 12, n4, pg. 42108-1 (2005)

[76] M. Shilov, Ph.D. Dissertation, Columbia University (2005)

[77] A.H. Boozer, Phys. Rev. Letters 86, pg. 5059 (2001)

[78] G.A. Navratil, C. Cates, M.E. Mauel, D. Nadle, E. Taylor, and Q. Xiao, Phys. Plasmas 5, pg.1855 (1998)

[79] T.D. de Wit, et. al., Phys. Plasmas 1, pg. 3288 (1991)

[80] P.R. Brunsell et. al, Physics Review Let. 93, pg. 225001 (2004)

[81] R. Fitzpatrick, Phys. Plasmas 4, pg. 4043 (1997)

[82] R. Fitzpatrick, Phys. Plasma 1, pg. 2931 (1994)

[83] G.A. Navratil, J. Bialek, A. Boozer, D. Maslovsky, presentation at US/JP Workshop of MHD Stab. Control of Tor. Plasmas, JAERI-Naka, Japan (2004)

[84] A. Bondeson, Y.Q. Liu, D. Gregoratto, C.M. Fransson and Y. Gribov, Plasma Phys. Control. Fusion 45, pg. A253 (2003)

[85] H. Zohm, Nuclear Fusion 35, pg. 543 (1995)